H3K36 METHYLATION REGULATES CELL PLASTICITY AND REGENERATION IN THE INTESTINAL EPITHELIUM

by

ALISON RAE SWEARINGEN PASHOS

B.A., Washington University in St. Louis, 2018

A thesis submitted to the
Faculty of the Graduate School of the
University of Colorado in partial fulfillment
of the requirement for the degree of
Doctor of Philosophy

Department of Molecular, Cellular, and Developmental Biology
2024

Committee Members:
Justin Brumbaugh, Ph.D - PI
Ed Chuong, Ph.D
Tin Tin Su, Ph.D
Lee Niswander, Ph.D
Peter Dempsey, Ph.D

Pashos, Alison Rae Swearingen (Ph.D., Molecular Cellular and Developmental Biology)
H3K36 Methylation Regulates Cell Plasticity and Regeneration in the Intestinal Epithelium
Thesis directed by Assistant Professor Justin Brumbaugh, Ph.D.

ABSTRACT

Cell plasticity is needed during development and homeostasis to generate diverse cell types from stem and progenitor cells. Following differentiation, plasticity must be restricted in specialized cells to maintain tissue integrity and function. For this reason, specialized cell identity is highly stable under homeostatic conditions; however, cells in some tissues regain plasticity during injury-induced regeneration. While precise gene expression is needed to control these processes, the regulatory mechanisms that restrict or promote cell plasticity are poorly understood. Here, I use the mouse small intestine as a model system to study cell plasticity. I find that H3K36 methylation reinforces expression of cell type-associated genes to maintain specialized cell identity in intestinal epithelial cells. Depleting H3K36 methylation leads to defects in lineage commitment and activates a plastic, regenerative gene expression signature. Correspondingly, I observe rapid and reversible remodeling of H3K36 methylation following injury-induced regeneration. Together, these data suggest a fundamental role for H3K36 methylation in reinforcing specialized lineages and regulating cell plasticity and regeneration.

DEDICATION

This dissertation is dedicated to my amazing husband, Michael Pashos.

ACKNOWLEDGEMENTS

Thank you first and foremost to all the family and friends who have supported me throughout the years – emotionally, financially, and physically. I am endlessly grateful for every little way in which you make my life easier.

Thank you to Justin for his support, guidance, and encouragement. I am a better writer, presenter, and scientist because of his mentoring. Justin is endlessly motivated and always pushes for clean, impactful experiments that ask meaningful questions, which are skills I continue to reach towards as a scientist. I appreciate his willingness to put in just as much effort to my project as I did every day.

Thank you to my committee: Ed, Tin Tin, Lee, and Peter, for their expert advice at every step of my journey. I further thank Peter for making it easy to collaborate between campuses, and making sure we stayed cheerful even when experiments failed.

Thank you to all my lab mates over the years, especially Mariel, for showing me that CUT&Tag was possible, and Mika and Erin, for fun scientific and non-scientific conversations at lunch every day. All their experimental input and commiseration has been critical for my success as a scientist.

Thank you to the NIH T32 Signaling and Cellular Regulation Training Grant for my funding for several years. This training grant helped me connect with fellow MCDB and Biochemistry graduate students, which led to many valuable interactions. Finally, thank you to MCDB's 50th anniversary class – without all of you this would have been a much lonelier path.

TABLE OF CONTENTS

Chapter

FIGURES

CHAPTER 1

1 INTRODUCTION

1.1 Chromatin organizes the genome

If you were to unspool the DNA in a single cell and lay it end to end it would extend for 2 meters, yet most cells are only a few micrometers in diameter. To accommodate this amount of DNA, eukaryotes have evolved mechanisms to package and condense DNA. The fundamental packaging mechanism for DNA is a nucleosome, which is composed of four canonical histones (H2A, H2B, H3, and H4) wrapped with ~147 bp of DNA[1]. Nucleosomes are octamers of histone proteins, comprised of two copies each of H2A, H2B, H3, and H4, and are considered the base unit of chromatin[1]. Nucleosomes wrapped in DNA are then further compacted by folding into more complex structures, called chromatin fibers, that make up the chromosomes of a cell[2]. Heterochromatin, the tightly wrapped chromatin fiber structure, makes DNA difficult to access and transcribe into RNA[3]. By contrast, some DNA is wrapped loosely with fewer nucleosomes for easier access and active transcription, and this is known as euchromatin[3]. Heterochromatin and euchromatin organize the genome in cells, both in location and transcription, and this organization directly affects cellular function and specialization[4].

1.1.1 Histone variants

The histones that comprise the nucleosome have multiple variants that can also affect transcription and cellular function[5]. Histone variants are encoded by different genes and have distinct protein sequences and chaperone systems that regulate their incorporation into the genome[5]. Most histones are canonical replicative variants, meaning they are inserted into chromatin to fill in voids created after the chromosome is duplicated during cell division[5]. For example, the histone chaperone CAF-1 is known to interact with the DNA replisome to deposit canonical H3-H4 dimers onto newly synthesized DNA[6]. These canonical histones are encoded by multiple genes that exist as intronless copies clustered together in the genome[5]. However, non-canonical histone variants also exist outside of these

canonical histone clusters in other places throughout the genome, often as multiple genes with introns, similar to a typical gene structure[5]. These non-canonical variants are expressed independently of replication and are dynamically incorporated to influence chromatin structure[5].

This thesis focuses on the core histone H3, which in mammals has three variants, H3.1 and H3.2 which are replication-dependent, and H3.3 which is replication-independent[7]. The non-canonical histone H3.3 is encoded by two genes in mammals, H3F3A and H3F3B, which translate into identical protein products that differ from H3.1 and H3.2 by only a few amino acids. These few amino acids allow for recognition of histone H3 variants by different chaperones, i.e. CAF-1 for H3.1/H3.2 versus the histone regulator A (HIRA) complex for H3.3[6,8–10]. As mentioned above, CAF-1 interacts with the processivity factor for DNA polymerases during DNA replication, and thereby adds H3.1/H3.2 in a replication-dependent manner[6]. By contrast, the HIRA complex associates with RNA polymerase II and regions of nucleosome-free DNA during active transcription to add H3.3 in a replication-independent manner[11]. H3.3 incorporation is therefore often associated with regions of euchromatin and active regulatory elements, and is the variant most often mutated in cancers[5,7]. Interestingly, H3.3 can also be deposited at regions of repetitive heterochromatin, such as telomeres, by a complex of ATRX and DAXX chaperones[5], suggesting varied roles for these histone variants. Chaperone-regulated incorporation of histone variants indicates how specific regions of chromatin are given unique properties that affect transcription and cell function.

1.1.2 Histone modifications

While chromatin can be regulated by dynamic incorporation of histone proteins, another important facet of chromatin regulation is post-translational modifications that decorate the unstructured N-terminal histone tail[12]. The tail of histone H3 is highly modified at distinct amino acids by addition or removal of chemical groups such as methylation, acetylation, and phosphorylation, that provide a versatile platform to display regulatory signals (Figure 1.1a)[12]. These histone modifications have been suggested to act as an “epigenetic code”, where both individual and combinations of marks convey distinct messages in the cell[13]. The epigenetic code of histone modifications is maintained by various

writers, readers, and erasers of these chemical groups (see Section 1.2 for more detail), and the balance of these enzymes is crucial for regulating the output of a given post-translational modification (Figure 1.1b)[14]. Many of these histone modifications have been linked to transcriptional activation or repression[15], which provides a mechanism by which histones can influence complex cell fate decisions[16]. In addition, histone modifications can be added or removed quickly, offering a dynamic system to fine-tune gene expression on a timescale that is compatible with rapid developmental changes[17–19].

Figure 1.1

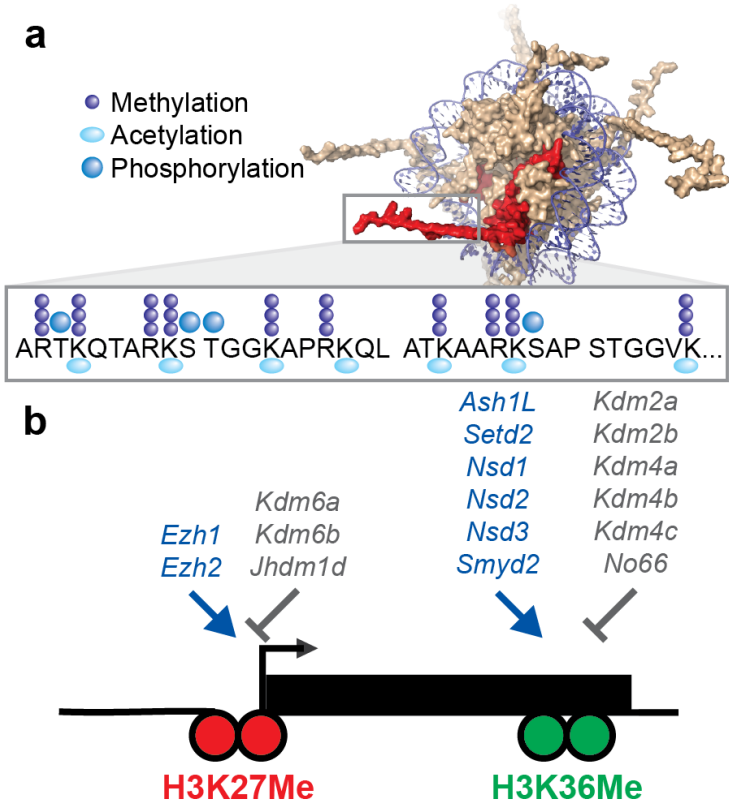

Figure 1.1 Histone modifications on the N-terminal tail of histone H3

(a) A simplified schematic of histone H3 showing a subset of possible modifications on the N-terminal tail.

(b) Specific sites on histone H3 are written and erased by multiple enzymes and are associated with different transcriptional states.

1.1.2.1 Histone acetylation

Histone acetylation, generally occurring at lysines, was one of the first noted histone modifications, and has been extensively characterized[14]. Histone acetylation is generally correlated with transcriptional activity and is often found in regions of euchromatin marking enhancers and promoters of actively transcribed genes[14]. There are several ways in which histone acetylation promotes transcription. First, acetylation neutralizes the positive charge of lysine, thereby disrupting internucleosome interactions and altering chromatin structure to be less compact and therefore more available for transcription factor binding[20]. Further, specific lysine acetylation sites (e.g., H3K27) are associated with active enhancers and have been suggested to increase enhancer-promoter interactions to support transcription[20]. Interestingly, removal of histone acetylation at a single site often has a limited effect on transcription, so histone acetylations are thought to act in a redundant and cumulative manner[21]. Finally, readers of histone acetylation such as BRD4 and transcription initiation factor TFIID subunit TAF1 are recruited by this mark to promote transcription[22]. Altogether, there are distinct roles for histone acetylation in regulating transcription and thus cell state.

1.1.2.2 Histone phosphorylation

Histone phosphorylation can occur on serine, threonine, and tyrosine residues, and like acetylation, is thought to enhance transcription[14]. For example, phosphorylation of H3.3S31, which is unique to the histone H3.3 variant, increases transcriptional output through interaction with histone acetyltransferase p300 and histone methyltransferase SETD2[14]. Recruitment of these enzymes thus increases the activating marks of histone acetylation and methylation[14]. Similarly, phosphorylation of H3S10 or H3S28 antagonizes repressive chromatin readers and writers such as HP1 and PRC2 to prevent gene repression[23]. These findings suggest extensive crosstalk exists between histone phosphorylation and other histone modifications, in support of the complex epigenetic code that contributes to gene regulation.

1.1.2.3 Histone methylation

Histone methylation can occur on any basic residue, namely arginines, histidines, and lysines[15]. These residues can be modified with one to three methyl groups, and the level of methylation as well as the site of methylation causes differential transcriptional regulation[15]. For example, trimethylation of H3K4 or H3K36 is generally coupled with active transcription, while H3K27 trimethylation is associated with repressed chromatin, and H3K4 monomethylation is linked to enhancer function[15]. Interestingly, in some contexts these marks have a different combined function when appearing in the same location. In embryonic stem cells, when H3K4 trimethylation and H3K27 trimethylation occur at the same locus, they poise genes for transcription, unlike their individual functions[24]. Each of these distinct methylation sites and levels must recruit different readers and cofactors to affect different transcriptional outcomes. For example, H3K4 trimethylation is associated with recruitment of transcription initiation factor subunit TAF3 and several lysine acetyltransferases that all suggest enhancement of transcription[25]. By contrast, TRIM24 is a chromatin regulator that contains multiple domains that recognize both unmethylated H3K4 and acetylated H3K23, suggesting that some readers incorporate information from multiple histone modifications at once[15]. Further, PHF8, a demethylase for H3K9, and KDM7A, a demethylase for H3K27, both recognize and bind to H3K4 di- and trimethylation[15]. This suggests that histone methylation must not be considered in isolation, but that extensive crosstalk with other modifications via recruitment of other histone readers, writers, and erasers is essential for understanding the functional output of these marks.

1.2 Histone 3 lysine 36 (H3K36) methylation

This thesis focuses on two modifications of lysine 36 on the tail of histone H3, H3K36 di- and trimethylation (H3K36me2 and H3K36me3). H3K36me2 and H3K36me3 can be added and removed quickly by several methyltransferases and demethylases respectively, supporting the possibility that they are involved in dynamic regulation of transcription (Figure 1.1b)[26]. In mammals, NSD1/2/3 and SETD2 are considered the primary H3K36 methyltransferases. SETD2 is the only enzyme that deposits

H3K36me1/2/3; the other methyltransferases catalyze H3K36me1/2[27]. These methyltransferases all contain a functional SET domain that transfers a methyl group from S-adenosylmethionine to the amino group of lysine 36 on histone H3[28]. To remove methylation of lysine 36, there are two families of demethylases, KDM2A/B and KDM4A-D. KDM2A/B remove H3K36me1/2, while KDM4A-D remove H3K36me2/3 and are also demethylases for H3K9 methylation[29–31].

H3K36me2 and H3K36me3 are generally associated with active transcription and have been implicated in regulation of transcriptional elongation. In yeast, Set2 is the homolog of SETD2 and is responsible for all methylation on H3K36, and deletion of Set2 causes defects in transcriptional elongation. Further, Set2 and SETD2 are known to associate with RNA Polymerase II in yeast and humans, respectively, and deposit methylation during the elongation process[26,32].

Another well-known function of H3K36 methylation is prevention of cryptic transcription, i.e., transcription originating from inside a gene instead of at the promoter region, which has been described in both yeast and mammalian cells[33]. In normal conditions, H3K36me2/3 are recognized by Rpd3S, a histone deacetylase complex that maintains low acetylation levels on histone tails[33]. In the absence of this histone deacetylase complex, H4 acetylation increases at the end of gene bodies, and cryptic transcription increases[33]. Further, deletion of Set2 in yeast leads to an increase in cryptic transcription[34], altogether suggesting a role for H3K36 methylation in preventing phenomena that lead to cryptic transcription.

A third described function of H3K36 methylation is regulation of alternative splicing. With depletion of SETD2 in human cells, widespread RNA splicing defects are observed[33]. Further, ZMYND11, a factor that binds H3K36me3 to regulate transcriptional elongation, also binds to RNA splicing factors, and knockdown of ZMYND11 leads to increased intron retention[32].

H3K36 methylation is also thought to play a functional role in DNA replication and repair. In yeast, H3K36 methylation has been implicated in replication origin firing as well as DNA replication checkpoint control, though the exact mechanisms of these functions are unclear[26]. Set2 limits creation of single-stranded DNA at sites of DNA damage, which promotes non-homologous end joining, and deletion of this protein causes defects in DNA damage response pathways in yeast[26,33]. In humans, deletion of SETD2 leads to defects in

homologous recombination, likely due to a failure to recruit essential DNA damage response factors[33,35].

The most relevant relationship for this thesis is that between H3K36 methylation, H3K27 methylation, and transcription. H3K36me2 is often found in intergenic regions, while H3K36me3 usually decorates gene bodies, but both modifications contribute to transcriptional regulation, at least in part, by antagonizing the repressive H3K27 trimethylation (H3K27me3) mark[36–41]. On a molecular level, unmodified H3K36 activates the H3K27 methyltransferase, EZH2, by fitting in a sensing pocket of this enzyme and triggering structural changes that enable H3K27 placement in the active site[42,43]. This results in addition of H3K27me3, and corresponding gene repression[42,43]. Both H3K36me2 and H3K36me3 disrupt this interaction in cis[42–47], likely because the addition of methylation at this site prevents proper positioning of the histone tail in the active site[42,43]. This therefore impedes the spread of H3K27me3 and, correspondingly, prevents repression of nearby genes[36,37,40,41]. In this way, H3K36 methylation may both prevent transcriptional repression and reinforce transcriptional elongation. Together, there is extensive evidence that H3K36 methylation mediates essential functions in the cell.

1.3 H3K36M mutant as a tool to study H3K36 methylation

Directly perturbing a given histone modification to study its function in mammalian backgrounds is challenging, in part because histones are encoded many times in the genome, as discussed above[48]. As a result, the functional significance of histone marks has largely been inferred from gain- and loss-of-function studies for histone-modifying enzymes, such as NSD1/2/3 or SETD2 for H3K36 methylation. A limitation of these studies is that histone modifications are typically regulated by multiple enzymes, which are difficult to perturb simultaneously, and may compensate for one another when one enzyme is disrupted (Figure 1.1b)[49]. Moreover, these proteins often have non-histone substrates or act to recruit additional regulatory factors, raising the possibility that phenotypes observed in these studies are unrelated to histone marks[50–52]. Together, these challenges illustrate the great need for tractable tools to directly manipulate specific histone modifications.

Recently, a heterozygous gain of function lysine-to-methionine (K-to-M) substitution on residue 36 of H3.3 (H3K36M) was identified in chondroblastoma, soft tissue sarcoma,

and head and neck squamous cell carcinoma[41,53,54]. Further research demonstrated that expression of H3K36M led to potent, global suppression of H3K36 methylation on the remaining endogenous copies of H3[55]. Interestingly, while H3.3 is the variant of histone H3 that is mutated in most cancers, expression of H3.1K36M recapitulates the same phenotypes as H3.3K36M[41]. While the role of K-to-M mutants has been extensively studied in the context of cancer, these K-to-M mutants also offer excellent tools to functionally connect specific histone modifications to diverse biological processes.

In this thesis, I use mice generated in our lab that express either WT H3.3 or H3.3K36M (Hereafter referred to as WT H3 or H3K36M). To create these mice, DNA encoding doxycycline-inducible versions of either WT H3 or H3K36M was inserted into mouse embryonic stem cells using a site-specific, single-copy integration system[56]. These modified embryonic stem cells were used to generate transgenic mice that express either WT H3 or H3K36M in all cells of the body following addition of doxycycline to drinking water[56]. This system offers us a tool to examine the effects of depletion of H3K36 methylation in vivo and functionally connect this histone modification to cell fate.

1.4 H3K36M mutant mechanism

H3K36M is thought to inhibit methylation through sequestration of cognate methyltransferases. Crystal structures of H3K36M bound to SETD2, the methyltransferase responsible for H3K36me3, show that insertion of the H3K36M side chain into the active site of SETD2 forms several preferential contacts that stabilize the interaction[57,58]. Interestingly, although the H3K36 methyltransferases NSD1, NSD2, and SETD2 showed increased affinity for H3K36M compared to wild type H3 under some conditions[41], NSD1 is not inhibited by the mutant histone in vitro[57,58]. H3K36M suppresses both H3K36me2 and H3K36me3[41,56,59], though the effect appears to be context-dependent as some studies report predominant loss of H3K36me2[60–62]. Genes downregulated following H3K36M induction lose H3K36 methylation, suggesting a direct connection between the mark and gene expression[56]. Overall, H3K36M offers a unique and convenient tool to specifically disrupt H3K36 methylation and study its functional role in a biological context.

1.5 Histone modifications as regulators of cell fate

Differentiation generates astonishingly diverse cell types, largely without altering the DNA sequence between cells. This concept suggests that precise regulation exists to interpret the genome in different ways. Various types of genome regulation can be seen at the signaling, post-transcriptional, translational, or epigenetic levels. Here, I will focus on epigenetic regulation, defined as a mechanism that influences cell phenotype without altering DNA sequence. Epigenetic regulation is thought to play a crucial role in guiding and ultimately reinforcing cell fate change[15], but our understanding of the factors involved remains incomplete. Histone modifications are prime candidates to mediate this epigenetic role for several reasons, namely the ability to rapidly add and remove these modifications which are linked to transcriptional activation or repression.

1.6 The small intestine as a model of differentiation

The small intestine acts as a crucial point of interaction between many organisms and the outside world[63]. In mammals, it has primary roles in nutrient absorption, barrier function, immune homeostasis, and defense against pathogens[64–66]. To perform these diverse duties, the intestine contains specialized cell types, which are organized into characteristic crypt-villus units (Fig. 2.1a). Intestinal stem cells (ISCs) reside in the crypt base and continuously replenish specialized cells by differentiating in a stepwise manner along distinct paths (Fig. 2.1b). Resident cells are subject to frequent challenge from food, pathogens, and digestive molecules that the intestine secretes to break down food. As a result, the intestinal epithelium is one of the most regenerative tissues in the human body and must turn over every 4-7 days, underscoring the importance of a robust stem cell compartment in maintaining intestinal tissue homeostasis.

The earliest cell fate decision in the intestinal epithelium divides cells between the secretory and enterocyte lineages (Fig. 2.1b)[64]. Mature enterocytes are important for absorbing food and maintaining an epithelial barrier, while secretory cells such as goblet and Paneth cells secrete mucus and antimicrobial enzymes to protect the surrounding tissue. Cell fate specification in the intestine is initiated by key signaling networks, including the Wnt, Notch, and BMP pathways. In particular, Notch signaling has a well

characterized role in the decision between the secretory and enterocyte lineages, while an increasing BMP gradient is involved in functional maturation of post-mitotic cells[67–72]. The balance between cell types is carefully maintained by inductive signaling and gene regulation to ensure proper organ function, and thus, the intestine provides an opportunity to study how differentiation into specialized cell fates is regulated.

1.7 The small intestine as a model of plasticity

Most tissues, including the intestine, require a pool of stem cells to replenish mature cell types and avoid organ failure. However, in the intestine, certain injuries (e.g., chemotherapy) or infection can damage ISCs, which presents a challenge in the context of regeneration. To overcome this challenge, intestinal progenitors and some differentiated cell types dedifferentiate to a highly plastic, regenerative state, capable of repopulating ISCs and, ultimately, every cell type in the intestinal epithelium. For example, secretory progenitors[73,74], Paneth cells[75,76], Bmi1^{+} label retaining cells[77–79], mature enterocytes[80], and enteroendocrine cells[81] can dedifferentiate, and even ISCs assume regenerative features in response to certain conditions[82]. Notably, gene expression profiles induced during regeneration share considerable overlap with fetal gene expression signatures, suggesting that regenerative responses may resemble developmental programs[82]. Importantly, this process is only initiated in response to damage, ensuring tissue integrity. Mature intestinal cells must modulate their plasticity to maintain homeostasis yet also dedifferentiate after tissue injury, and therefore the intestine offers a good model to study how cell plasticity is regulated.

1.8 Organoids as a model of the small intestine

The mouse small intestine offers an excellent system for studying cell homeostasis and plasticity. One advantage of this tissue is that 3D epithelial structures, known as organoids, can be generated from mouse and human intestines and cultured in vitro for experimental ease. In fact, single ISCs from mouse intestinal crypts can be isolated, grown in a 3D matrix with defined growth supplements, and expanded indefinitely to generate organoids containing all mature intestinal cell types[83]. In vivo, the intestinal epithelium is

supported by mesenchymal, blood, immune, and other cell types. In vitro, the epithelium is isolated yet still recapitulates the crypt-villus structure seen in vivo[83,84]. This benefits studies of intestinal epithelial cells by removing any confounding cell types while maintaining structural complexity. Importantly, intestinal organoids can also be manipulated in ways that are more difficult in vivo, such as gene knockdown, irradiation, drug treatment, or enrichment for specific cell types.

1.9 Histone modifications in the small intestine

To date, relatively few histone modifications have been studied in the context of intestinal epithelial cell differentiation. However, some epigenetic features, such as open chromatin, repressive histone modifications (e.g. H3K27me3), marks of active enhancers (e.g. H3K4 methylation and H3K27 acetylation), and DNA methylation are surprisingly similar between enterocyte progenitors, secretory progenitors, and ISCs [67,85–91]. For example, distributions of H3K27me3 across the genome were shown to be similar between ISCs and mature villus cells, with a poor association between loss of repressive H3K27me3 and gene activation[92]. Indeed, loss of PRC2, the methyltransferase for H3K27me3, in the intestine did not lead to a re-activation of repressed ISC-related genes in mature villus cells, suggesting involvement of other safeguards against dedifferentiation[92]. Similarly, loss of KDM6A/B (demethylases for H3K27me3) did not influence intestinal cell proliferation or differentiation, indicating that this modification is not an essential barrier between intestinal cell types[93]. Others have characterized enhancer marks in sorted enterocyte progenitors and secretory progenitors, revealing similar levels and distributions of these marks in each cell type, despite differential gene expression between the two cell types[67]. Interestingly, these enhancers were already marked with H3K4me2 and H3K27ac in undifferentiated ISCs and were further characterized by regions of open chromatin that were then maintained during differentiation into enterocyte and secretory progenitors[67]. This suggests a priming of enhancers in ISCs that is maintained during the first intestinal differentiation steps. DNA methylation, often a suppressive mechanism, was further shown to be similar at enhancers and promoters between ISCs and enterocytes[85]. Presumably, maintaining similar chromatin profiles on enhancers and promoters lowers the barrier to dedifferentiation and explains how intestinal epithelial cells retain plasticity to

interconvert between cell types[67]. However, this leads to the unresolved question of how intestinal epithelial cells reinforce lineage identity and function while retaining the capacity to dedifferentiate.

1.10 H3K36 methylation as a regulator of differentiation and plasticity in the intestine

Our lab previously showed that methylation of histone H3K36 plays a fundamental role in regulating lineage-specific genes in pluripotent and hematopoietic stem cells[56], but little is known about H3K36 methylation in intestinal differentiation. This regulatory input is downstream of transcriptional activation or repression, providing a mechanistically distinct way for intestinal epithelial cells to control transcriptional output, compared to previously studied histone modifications in the intestine. I therefore hypothesized that H3K36 methylation reinforces cell type-specific gene expression to maintain cell identity and prevent reversion to a plastic, regenerative state. Using chromatin profiling tools, I have shown that H3K36 methylation is distinct between mature intestinal epithelial cell types and reinforces highly transcribed genes. I have used the histone mutant H3K36M to disrupt H3K36 methylation in intestinal organoids and mice, confirming a functional role for this mark in intestinal epithelial cell differentiation and regeneration. Overall, this work is the first to identify a crucial epigenetic regulatory switch that mediates the balance between specialized cell identity and regeneration in the intestine.

CHAPTER 2

2 H3K36 METHYLATION REGULATES CELL PLASTICITY AND REGENERATION IN THE INTESTINAL EPITHELIUM

2.1 Introduction

Complex tissues contain diverse cell types with distinct functions. This diversity is achieved during development through the differentiation of stem and progenitor cells into specialized cell types. During differentiation, cell plasticity (i.e., the ability of a cell to change phenotypic features or function) is progressively restricted to reinforce the identity of specialized cell types and safeguard tissue integrity. Maintaining the balance of specialized cells is therefore crucial for tissue function, and failure to properly restrict cell plasticity is a hallmark of cancer. Yet, some degree of plasticity is needed over the lifetime of an adult organism. Dying and displaced cells within many tissues must be replaced by stem or progenitor cells to maintain homeostasis and, in some tissues, cells regain plasticity as part of a regenerative response to injury. These points underscore the importance of understanding the mechanistic basis for cell plasticity, but little is known about the regulation that governs it.

The small intestine is a tractable model system to study cell plasticity, both under conditions of homeostasis and regeneration. In mammals, the intestinal epithelium contains specialized cell types, which are organized into characteristic crypt-villus units (Fig. 2.1a). *Lgr5*$^{+}$ intestinal stem cells (ISCs) reside in the crypt base and continuously replenish specialized cells by differentiating in a progressive manner along different specification paths (Fig. 2.1b). The earliest cell fate decision in the intestinal epithelium divides cells between the secretory and enterocyte lineages[94]. Mature enterocytes are important for absorbing food and maintaining an epithelial barrier, while secretory cells such as goblet and Paneth cells secrete mucus and antimicrobial proteins or peptides to protect the surrounding tissue. Hormone-secreting enteroendocrine cells and chemosensory Tuft cells also belong to the secretory lineage and are less abundant compared to other cells in the epithelium. The balance between intestinal epithelial cell types must be carefully

maintained to ensure proper organ function, and thus, the intestine provides an opportunity to study how plasticity is regulated to achieve the proper balance of specialized cell fates.

Certain injuries or infection can damage ISCs, which presents a challenge in the context of regeneration. Without a stem cell pool, the intestinal epithelium cannot replenish, which ultimately leads to organ failure. To overcome this challenge, intestinal progenitors and many specialized cell types dedifferentiate upon injury into a highly plastic, regenerative state, capable of repopulating ISCs and, ultimately, every cell type in the intestinal epithelium[94]. For example, secretory progenitors[73,74], Paneth cells[75,76], Bmi1^{+} label retaining cells[77–79], mature enterocytes[80], and enteroendocrine cells[81] can dedifferentiate. Notably, even ISCs downregulate gene expression associated with stem cell function and assume regenerative features in response to damage[82]. Thus, the intestine also provides an opportunity to study the acquisition of plasticity during regeneration. Importantly, this process is only initiated in response to damage, ensuring tissue integrity. This leads to a major, unresolved question in the field: how do intestinal epithelial cells reinforce lineage identity and function, while retaining the capacity to dedifferentiate into a highly plastic state when needed?

Epigenetic regulation (i.e., a mechanism that influences the biology of the cell without altering its DNA sequence) is thought to play a crucial role in guiding and ultimately reinforcing cell fate change, but our understanding of the factors involved in regulating plasticity remains incomplete[15]. Several histone post-translational modifications have been studied in the context of the intestinal epithelium; however, most epigenetic features, such as chromatin accessibility, repressive histone modifications, DNA methylation, and marks of active enhancers (e.g., H3K4 methylation and H3K27 acetylation) are surprisingly similar between intestinal epithelial cells[67,85–91]. Presumably, maintaining similar chromatin profiles on enhancers and promoters lowers the barrier to dedifferentiation and explains how intestinal epithelial cells regain plasticity following injury[67]. Yet, mature intestinal epithelial cells are functionally and transcriptionally distinct from one another and from ISCs, which begs the question of how these cells maintain their identity.

We previously reported that methylation of H3K36 plays a fundamental role in regulating lineage-specific genes in pluripotent and hematopoietic stem cells[56]; however, little is known about H3K36 methylation in intestinal differentiation. H3K36 di- and tri-

methylation (H3K36me2 and H3K36me3) are generally associated with active transcription[26]. While a direct, mechanistic link between H3K36 methylation and gene expression remains elusive in mammals, mounting evidence suggests that H3K36me2 and H3K36me3 contribute to transcriptional regulation, at least in part, by antagonizing Polycomb activity and the repressive H3K27me3 mark[36–41]. On a molecular level, unmodified H3K36 activates the H3K27 methyltransferase, EZH2, by engaging a distinct "sensing" pocket on the protein[42,43]. Both H3K36me2 and H3K36me3 disrupt this interaction in *cis*[42–47], impeding the spread of H3K27me3 and, correspondingly, preventing repression of nearby genes[36,37,40,41]. In this way, H3K36 methylation acts as an important barrier to repressive chromatin modifications.

Here, I report that different intestinal epithelial cell types have distinct H3K36 methylation profiles, which are pronounced in secretory cell types. Disrupting H3K36me2 and H3K36me3 leads to the spread of repressive H3K27me3 in the regions flanking cell type-associated genes, resulting in their downregulation and a corresponding defect in secretory cell differentiation during adult intestinal homeostasis. These data suggest that H3K36 methylation reinforces gene expression needed to maintain specialized intestinal epithelial cell identity. Supporting these findings, suppressing H3K36 methylation in the intestinal epithelium induced a plastic state, characterized by a regenerative gene expression signature. Further, when I irradiated mice or intestinal organoids to induce injury and regeneration, I observed a widespread, transient reduction in H3K36 methylation, particularly at cell type-associated genes, that resolved as regeneration completed and normal homeostatic growth resumed. Overall, I identify H3K36 methylation as a crucial regulatory switch that mediates the balance between specialized cell identity and regeneration in the intestine.

2.2 Results

2.2.1 H3K36me3 is distinct at cell type-associated genes in intestinal epithelial cells

ISCs, progenitor cells, and mature epithelial cells display remarkably similar chromatin profiles based on the promoter and enhancer marks tested to date[67,85–91]. This

finding is surprising given the vastly different functional roles and gene expression profiles associated with each cell type; however, our understanding of the epigenetic landscape in the intestine remains incomplete. In particular, H3K36 methylation remains largely unexplored in the small intestine. To address this gap in knowledge, I leveraged established reporter mouse lines to sort ISCs, enterocytes, tuft cells, enteroendocrine cells, goblet cells, and Paneth cells, which cover primary cell types in the intestinal epithelium (Fig. 2.1a,b and Fig. S1a,b). An important advantage of this approach is that each cell type is isolated without disrupting homeostasis in the intestine through chemical or genetic enrichment for certain lineages (Fig. S1b). RNA-seq analysis confirmed distinct transcriptional profiles and expression of known markers for each sorted cell type (Fig. S1c,d). I next used Cleavage Under Targets and Tagmentation (CUT&Tag), a technique that maps the genome-wide occupancy of proteins or protein modifications, analogous to ChIP-seq[95]. Specifically, I profiled H3K36me3 and H3K27me3, two antagonistic histone modifications that are generally associated with active and repressive chromatin, respectively. I observed strong enrichment of H3K36me3 over previously published sets of cell type-associated genes in each respective cell type[96], which was particularly pronounced in Paneth cells (Fig. 2.1c and Fig. S1e). To visualize locus-specific differences between cell types, I plotted the fold-change of H3K36me3 peaks between each cell type and marked differentially expressed genes corresponding to each peak ($\log_2FC > 1$, $p < 0.05$, colored data points; Fig. 2.1d and Fig. S2a). Importantly, many genes with the largest differences in H3K36me3 enrichment were established markers of intestinal epithelial cell identity (e.g., *Lgr5* and *Olfm4* in ISCs, *Lyz1* and *Mmp7* in Paneth cells; Fig. 2.1d, labeled data points). By contrast, pairwise comparison of H3K27me3 patterns did not partition cell type-associated genes (Fig. 2.1e and Fig. S2b); however, H3K27me3 anticorrelated with H3K36me3, consistent with the mutually antagonistic nature of the marks (Fig. S1f). Collectively, these data reveal that H3K36me3, unlike other histone modifications previously studied, is preferentially enriched at cell type-associated genes in the intestine.

H3K36 methylation is generally associated with active transcription[26]. I therefore asked whether H3K36me3 levels differed between cell type-associated genes and other genes that are expressed in intestinal epithelial cells but are not necessarily associated with cell identity. Notably, cell type-associated genes in each differentiated cell type had higher levels of H3K36me3 compared to other expressed genes (Fig. 2.1f-k and Fig. S1g-l).

As expected, cell-type associated genes with high levels of H3K36me3 had correspondingly higher levels of expression (Fig. 2.1g,i,k and Fig. S1h,j,l). These observations raise the possibility that increased H3K36 methylation reinforces high levels of expression for cell type-associated genes to safeguard their specialized cell fate. In support of this notion, *Gfi1*, a well-established marker of goblet and Paneth cells, had both significantly increased gene expression and significantly increased H3K36me3 in goblet and Paneth cells (Fig. S1m). Conversely, I identified non-cell type-associated genes (e.g., *Mettl1* and *Commd4*) that had strong gene expression in goblet and Paneth cells but had no consistent difference in H3K36me3 compared to other cell types (Fig. S1n). These data suggest that H3K36me3 levels are highest on cell type-associated genes and may therefore function as primary regulators of their expression, but are not necessarily a primary regulator of non-cell type-associated genes, like *Mettl1* or *Commd4*.

Figure 2.1

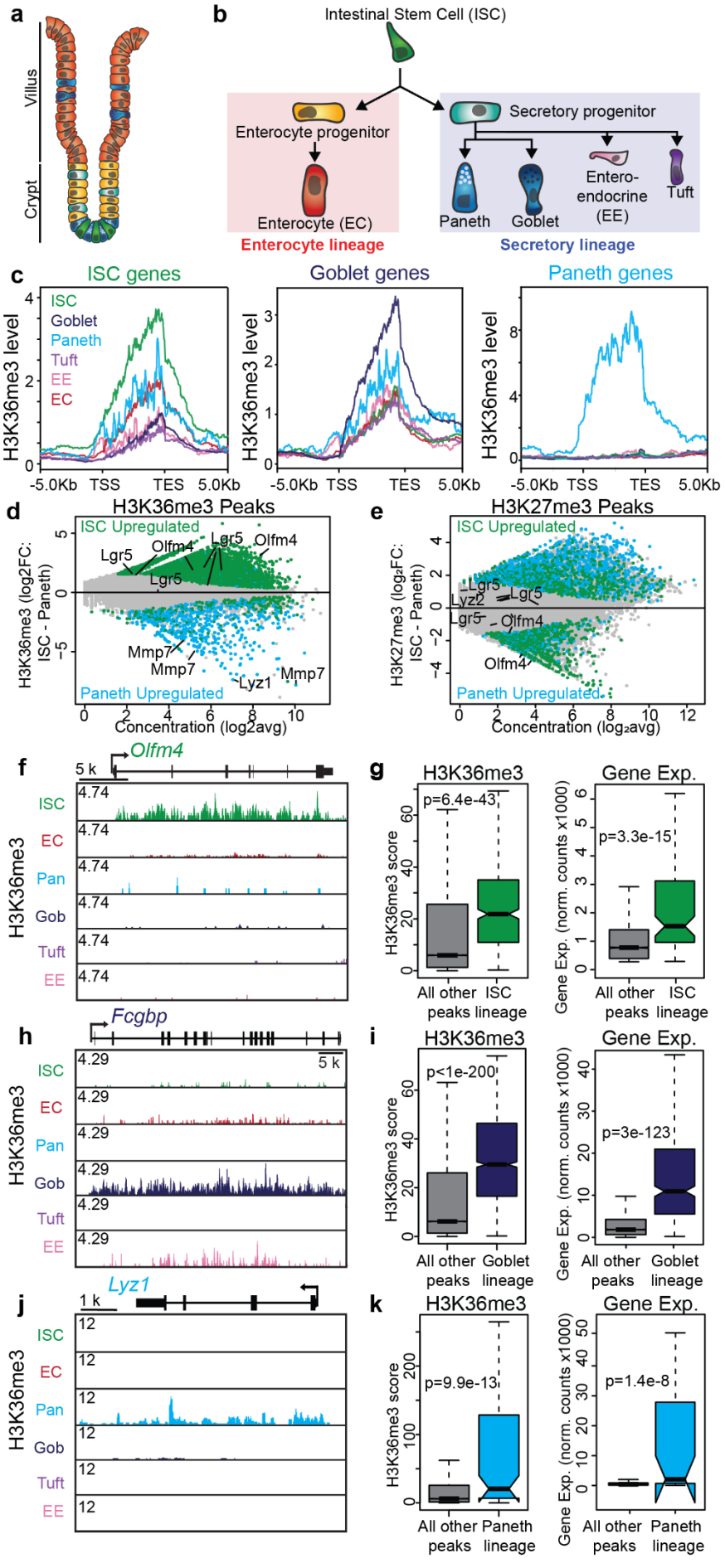
a
Villus
Crypt
b
Intestinal Stem Cell (ISC)
Enterocyte progenitor
Enterocyte (EC)
Enterocyte lineage
Secretory progenitor
Paneth
Goblet
Entero-endocrine (EE)
Tuft
Secretory lineage
c
ISC genes
Goblet genes
Paneth genes
H3K36me3 level
ISC
Goblet
Paneth
Tuft
EE
EC
-5.0Kb TSS TES 5.0Kb
d
H3K36me3 Peaks
ISC Upregulated
Paneth Upregulated
H3K36me3 (log2FC: ISC - Paneth)
Concentration (log2avg)
Lgr5
Olfm4
Mmp7
Lyz1
e
H3K27me3 Peaks
H3K27me3 (log2FC: ISC - Paneth)
Concentration (log2avg)
Lyz2
f
Olfm4
5 k
H3K36me3
ISC
EC
Pan
Gob
Tuft
EE
4.74
g
H3K36me3
Gene Exp.
p=6.4e-43
p=3.3e-15
H3K36me3 score
Gene Exp. (norm. counts x1000)
All other peaks
ISC lineage
h
Fcgbp
4.29
i
p<1e-200
p=3e-123
Goblet lineage
j
Lyz1
1 k
12
k
p=9.9e-13
p=1.4e-8
Paneth lineage

Figure 2.1 Intestinal epithelial cells have distinct H3K36 methylation profiles at cell type-associated genes.

(a) A schematic of a typical crypt-villus intestinal unit.

(b) A simplified schematic of differentiation in the intestinal epithelium.

(c) Meta-analysis of H3K36me3 over published[96] cell-type specific genes in each sorted cell type (representative trace for 2 biological replicates). The goblet cell and Paneth cell gene sets are modified from Haber et al.[96] (see methods for details).

(d) Differential H3K36me3 peaks between ISCs and Paneth cells. Colored dots indicate peaks over differentially expressed genes (blue = upregulated genes in Paneth cells, green = upregulated genes in ISCs). Labeled dots are established markers of each cell type.

(e) Differential H3K27me3 peaks between ISCs and Paneth cells. Colored dots indicate peaks over differentially expressed genes (blue = upregulated genes in Paneth cells, green = upregulated genes in ISCs). Labeled dots are established markers of each cell type.

(f) Gene tracks for H3K36me3 at *Olfm4*, an ISC-associated gene (representative track for 2 biological replicates).

(g) Left, boxplots for H3K36me3 levels for a published[96] ISC-associated gene set and all other genes; right, boxplots for gene expression for a published[96] ISC-associated gene set and all other genes (n = 2 biological replicates; Wilcoxon test; box plot center lines represent the median, box edges represent the first and third quartiles, and whiskers indicate minimum and maximum values).

(h) Gene tracks for H3K36me3 at *Fcgbp*, a goblet cell-associated gene (representative track for 2 biological replicates).

(i) Left, boxplots for H3K36me3 levels for a published[96] goblet cell-associated gene set and all other genes; right, boxplots for gene expression for a published[96] goblet cell-associated gene set and all other genes (n = 2 biological replicates; Wilcoxon test; box plot center lines represent the median, box edges represent the first and third quartiles, and whiskers indicate minimum and maximum values).

(j) Gene tracks for H3K36me3 at *Lyz1*, a Paneth cell-associated gene (representative track for 2 biological replicates).

(k) Left, boxplots for H3K36me3 levels for a published[96] Paneth cell-associated gene set and all other genes; right, boxplots for gene expression for a published[96] Paneth cell-associated gene set and all other genes (n = 2 biological replicates; Wilcoxon test; box plot center lines

represent the median, box edges represent the first and third quartiles, and whiskers indicate minimum and maximum values).

2.2.2 Suppression of H3K36 methylation disrupts adult intestinal homeostasis

Chromatin profiling suggested a strong link between H3K36 methylation and cell type-associated gene expression in the intestinal epithelium; however, this approach cannot distinguish whether a particular histone modification regulates or simply correlates with gene expression. To directly test the function of H3K36 methylation in intestinal cell fate, I used mice that harbor a stably integrated, doxycycline-inducible copy of either wild-type H3.3 or H3.3 with a lysine-to-methionine mutation at amino acid 36 (*Col1a1-tetO-H3; Rosa26-M2rtTA* and *Col1a1-tetO-H3K36M; Rosa26-M2rtTA*; hereafter referred to as WT H3 or H3K36M) (Fig. 2.2a)[56]. These constructs are expressed at a low level and, while the WT H3 control has no appreciable effect on histone modifications, H3K36M acts in a dominant-negative manner to suppress methylation specifically at H3K36 [36,41,55,56,59]. Moreover, H3K36M is only detectable in the nucleus, properly incorporates into chromatin, and does not directly alter methylation of other H3 residues[55,56,59]. I used doxycycline to induce expression of WT H3 and H3K36M in adult mice (i.e., 8-16 weeks of age) for four weeks (Fig. 2.2a) and observed strong expression of the H3K36M mutant and concomitant loss of H3K36 di- and trimethylation (H3K36me2/3) in the bulk intestinal epithelium (Fig. 2.2b). Importantly, immunofluorescence on duodenal sections from H3K36M mice showed significant loss of H3K36me2/3 in all cells of the intestinal epithelium, confirming full penetrance for our transgene (Fig. 2.2c). By contrast, stromal cells did not strongly express H3K36M and retain H3K36 methylation (Fig. 2.2c), as the transgene is silenced in mesenchymal cells[97]. Thus, our system effectively depletes H3K36 methylation in the intestinal epithelium.

I next asked whether the balance of cells in the intestinal epithelium was disrupted following suppression of H3K36 methylation. Histological analysis revealed dramatically fewer goblet cells, identified by periodic acid-Schiff (PAS) staining, in the villus of H3K36M mice (Fig. S3a). This finding was supported by immunofluorescence for MUC2, a marker of goblet cells, which confirmed the significant loss of these cells in H3K36M-expressing mice

(Fig. 2.2d). Additionally, immunofluorescence for LYZ1, a marker of Paneth cells, revealed improperly localized LYZ1-positive cells in the villi of intestines from H3K36M-expressing mice, suggesting a defect in secretory lineage differentiation and the accumulation of an aberrant secretory cell (Fig. 2.2e, white arrows). Based on these striking phenotypes, I decided to focus my analyses primarily on goblet and Paneth cells; however, I also noted a trend toward increased CHGA+ enteroendocrine cells and decreased DCLK1+ tuft cells in H3K36M villi (Fig. S3b,c). These data are consistent with other studies that reported a modest expansion of enteroendocrine cells and depletion of tuft cells upon goblet/Paneth cell loss[98]. Despite these defects, overall crypt-villus structure was maintained, suggesting a specific defect in cell fate specification and homeostasis in the intestinal epithelium (Fig. 2.2c and Fig. S3a). Collectively, these observations suggest that H3K36 methylation reinforces intestinal cell type-specific gene expression and plays a fundamental role in the regulation of secretory cell types in the intestinal epithelium.

2.2.3 H3K36M changes chromatin and gene expression at cell type-associated genes

To understand the mechanistic basis for my observations, I profiled gene expression and histone modifications in the bulk intestinal epithelium of adult WT H3 and H3K36M mice. To control for the widespread loss of H3K36 methylation in H3K36M samples, I used a spike-in histone panel control for normalization in all CUT&Tag samples[99]. Consistent with western blot analysis (Fig. 2.2b), H3K36M expression globally suppressed H3K36 methylation after 4 weeks of doxycycline treatment (Fig. 2.3a and Fig. S3d,e). Despite the general association between H3K36 methylation and transcriptional activity, I did not observe an indiscriminate decrease in gene expression for H3K36M samples. In fact, only a subset of genes (1044 transcripts) were significantly downregulated in bulk H3K36M intestinal epithelial cells compared to WT H3 control (Fig. 2.3a, yellow dots), which is consistent with previous studies in the mouse hematopoietic system[56], mouse chondrocytes[59], and *Drosophila* eye imaginal discs[36]. Notably, downregulated genes in H3K36M samples had lower levels of H3K36me3 compared to all other genes (Fig. 2.3b). These data suggest that the regulatory effects of H3K36 methylation are nuanced and cell type- or gene-specific. Supporting this notion, gene set enrichment analysis revealed that

expression signatures characteristic of specialized cells, including goblet cells and intestinal stem cells, were diminished in H3K36M intestinal epithelium (Fig. 2.3c). Accordingly, established markers of each cell type (*Muc2* for goblet cells, *Olfm4* for ISCs) were decreased in H3K36M samples compared to WT H3 controls (Fig. S3f), corresponding to the defect in homeostasis observed by immunofluorescence (Fig. 2.2d). Gene expression signatures associated with Paneth cells were modestly increased in H3K36M samples, perhaps reflecting the mislocalized and increased number of $LYZ1^+$ secretory cells in the villi of the H3K36M intestine (Fig. 2.2e and Fig. 2.3c; see also below). Finally, expression of *Mettl1* and *Commd4*, discussed above as non-lineage associated genes, did not change in H3K36M samples compared to control, despite a dramatic reduction in H3K36me3 over their gene bodies (Fig. S3g). By contrast, H3K36me3 decreased over *Gfi1*, a goblet/Paneth cell marker, with a corresponding loss of gene expression (Fig. S3g). Together, these observations suggest that H3K36 methylation is important for reinforcing the expression of cell type-associated genes, and disrupting this regulatory system prevents the acquisition or maintenance of mature, specialized cell types in the intestinal epithelium.

Figure 2.2

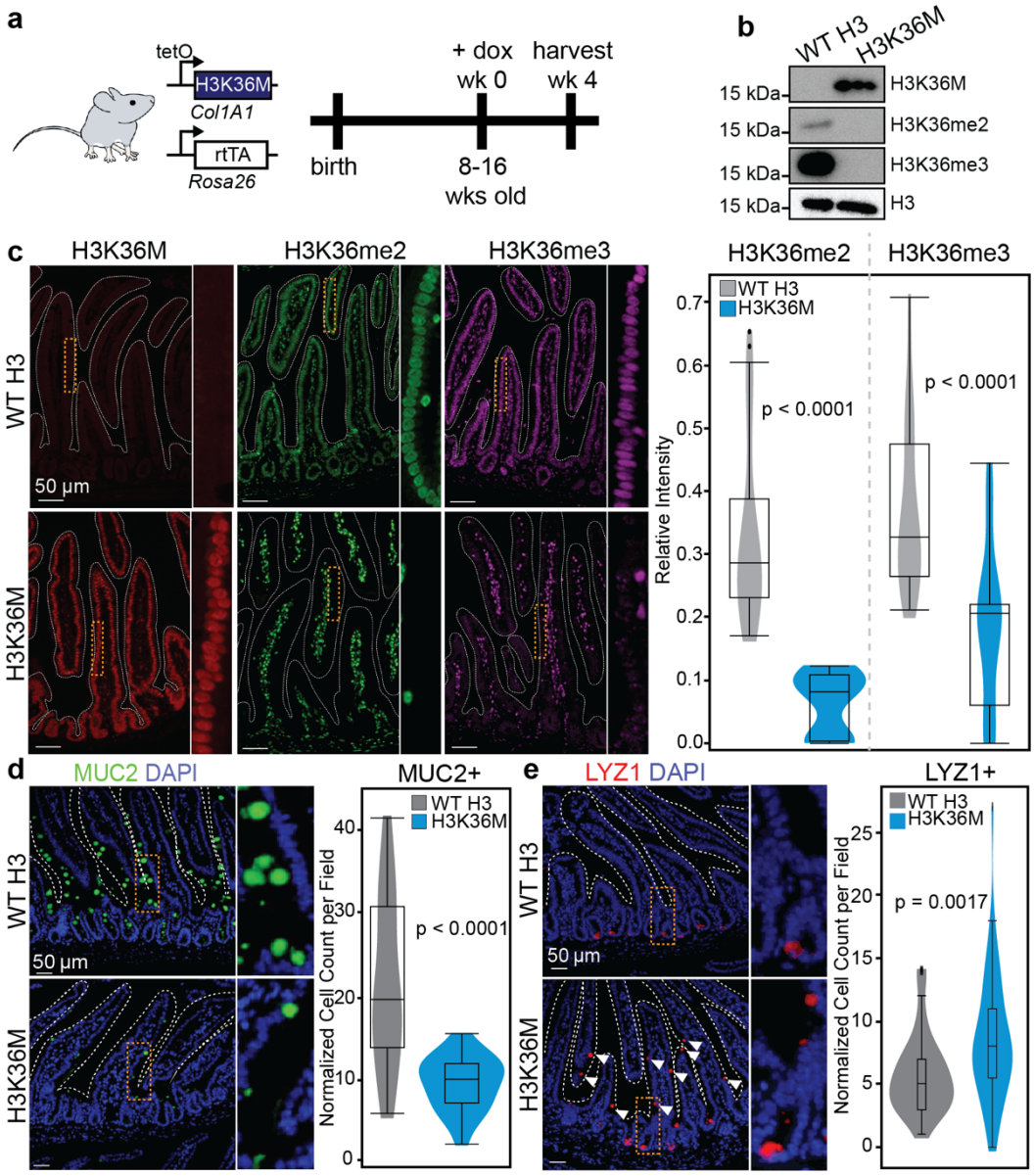

Figure 2.2 Suppressing H3K36 methylation disrupts adult intestinal homeostasis.

(a) A schematic of the experimental design for induction and harvest of WT H3 and H3K36M intestinal epithelium.

(b) Western blot analysis of bulk intestinal epithelium.

(c) Left, representative images of immunofluorescence in WT H3 and H3K36M intestines (n = 3 WT H3 mice, 2 H3K36M mice). The inset is a magnified image of the epithelium. Right, quantification of immunofluorescence (n = 10 images per mouse; unpaired two-tailed

student's t-test; box plot center lines represent the median, box edges represent the first and third quartiles, and whiskers indicate minimum and maximum values).
(d) Representative images of immunofluorescence for MUC2 on WT H3 and H3K36M intestinal sections (left; n = 2 mice each) and quantification (right; n = 10 images per mouse; unpaired two-tailed student's t-test; box plot center lines represent the median, box edges represent the first and third quartiles, and whiskers indicate minimum and maximum values).
(e) Representative images of immunofluorescence for LYZ1 on WT H3 and H3K36M intestine sections after four weeks dox induction (left; n = 2 mice each) and quantification (right; n = 10 images per mouse; unpaired two-tailed student's t-test; box plot center lines represent the median, box edges represent the first and third quartiles, and whiskers indicate minimum and maximum values).

I next asked whether the loss of H3K36me3 led to the spread of H3K27me3 over gene bodies in the intestinal epithelium, as reported for other systems[36,41,56,100]. Indeed, I observed a marked increase in H3K27me3 that correlated with the loss of H3K36me3 over downregulated genes in H3K36M samples relative to WT H3 control (Fig. 2.3d,e). Quantification of histone methylation levels over gene bodies revealed a distinct loss of H3K36me3 and corresponding gain of H3K27me3 over all downregulated genes and this trend was consistent for ISC and goblet cell related genes (Fig. 2.3f,g). These data provide additional support that loss of H3K36me3 over gene bodies of cell type-associated genes leads to an increase in repressive H3K27me3 and silencing of specialized genes.

Based on western blot analysis, H3K36M expression suppresses both H3K36me3 and H3K36me2 in the intestinal epithelium (Fig. 2.2b). Like H3K36me3, I confirmed genome-wide loss of H3K36me2 in H3K36M samples by CUT&Tag analysis (Fig. S3e). Unlike H3K36me3, which localizes primarily to gene bodies, H3K36me2 exists in broad domains across both genic and intergenic regions. This distribution makes it difficult to infer relationships between H3K36me2 and gene expression; however, given its antagonistic relationship with Polycomb Repressive Complex 2 (PRC2)[36–41], previous work suggested that H3K36me2 acts as a boundary to prevent the spread of the repressive H3K27me3 mark into intergenic regions[36,40,56,101]. These regions may be important for the expression of nearby genes, as they harbor cis regulatory elements (i.e., enhancers and

promoters). To explore this relationship in intestinal epithelial cells, I plotted H3K27me3 signal in a 25 kb window surrounding genes downregulated in H3K36M compared to WT H3 samples (Fig. 2.3h). Consistent with previous observations[41], I noted broad spreading of H3K27me3 following expression of H3K36M, particularly into intergenic regions that lost H3K36me2 (Fig. 2.3h and Fig. S3h-j). This effect was consistent for genes associated with ISCs and goblet cells (Fig. 2.3i-k). Together, these data suggest that H3K36me2 and H3K36me3 prevent inappropriate spreading of H3K27me3 and silencing of cell type-associated genes.

Figure 2.3

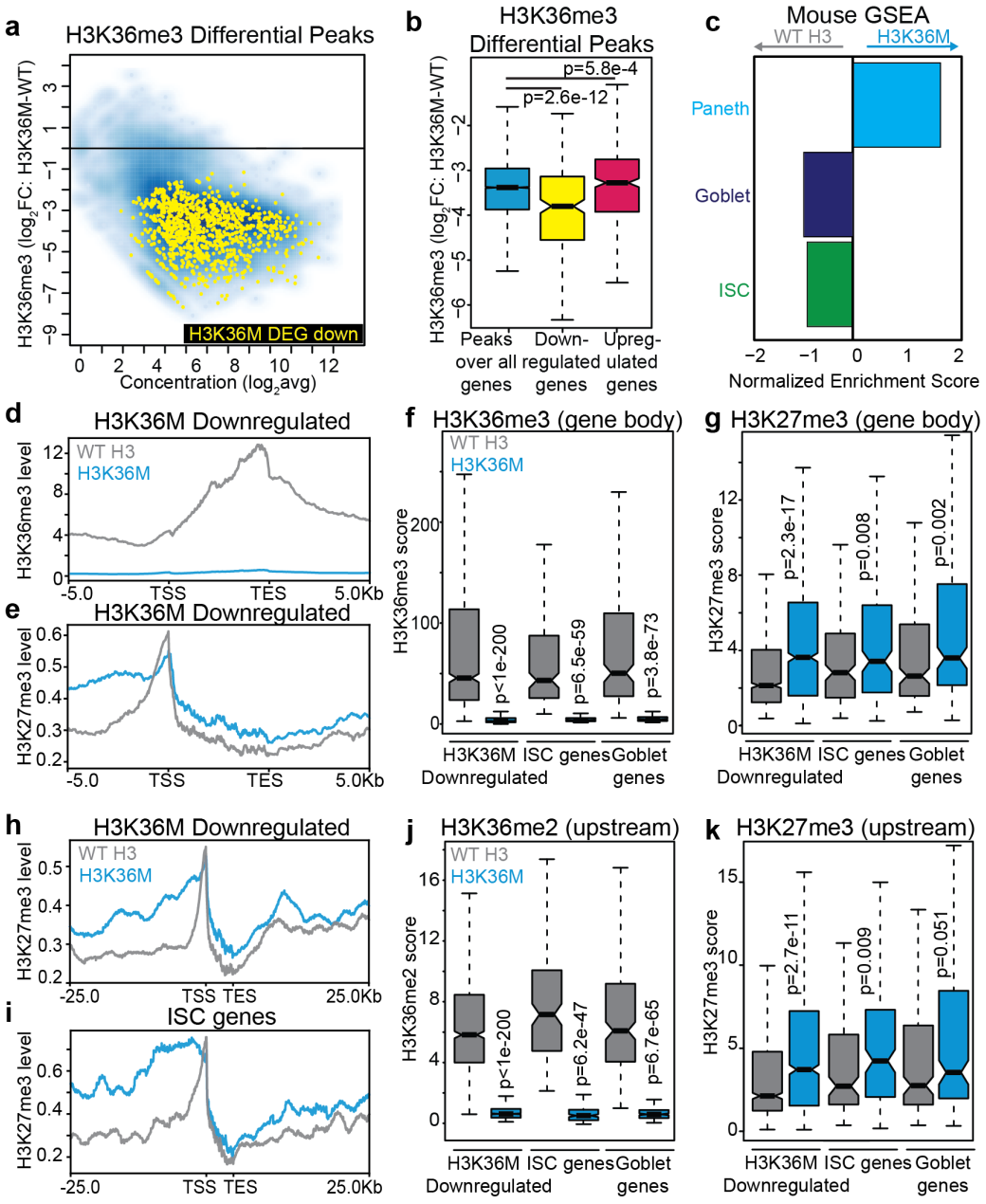

Figure 2.3. Expressing H3K36M disrupts chromatin and gene expression at cell type-associated genes.

(a) Differential peaks for H3K36me3 between WT H3 and H3K36M mice induced for four weeks. Yellow dots indicate peaks occurring over significantly downregulated genes in H3K36M from RNA-seq (n = 2 mice each; downregulated genes defined as p-value < 0.05 and $\log_2$FC > 1).

(b) Quantification of H3K36me3 for all peaks over genes, H3K36M downregulated genes, or H3K36M upregulated genes (Wilcoxon test; box plot center lines represent the median, box edges represent the first and third quartiles, and whiskers indicate minimum and maximum values).
(c) Gene set enrichment analysis based on RNA-seq from WT H3 and H3K36M intestines after four weeks dox induction using published cell type-associated gene sets[96].
(d) Meta-analysis of H3K36me3 over genes downregulated H3K36M samples (5kb window around the TSS and TES).
(e) Meta-analysis of H3K27me3 over genes downregulated H3K36M samples (5kb window around the TSS and TES).
(f) Quantification of H3K36me3, binned into 10 kb regions over the gene body of genes downregulated in H3K36M samples, ISC-associated genes, and goblet cell-associated genes (Wilcoxon test; box plot center lines represent the median, box edges represent the first and third quartiles, and whiskers indicate minimum and maximum values).
(g) Quantification of H3K27me3, binned into 10 kb regions over the gene body of genes downregulated in H3K36M samples, ISC-associated genes, and goblet cell-associated genes (Wilcoxon test; box plot center lines represent the median, box edges represent the first and third quartiles, and whiskers indicate minimum and maximum values).
(h) Meta-analysis of H3K27me3 over genes downregulated H3K36M samples (25kb window around the TSS and TES).
(i) Meta-analysis of H3K27me3 over ISC-associated genes (25kb window around the TSS and TES).
(j) Quantification of H3K36me2, binned into 1 kb regions upstream of the gene body of genes downregulated in H3K36M samples, ISC-associated genes, and goblet cell-associated genes (Wilcoxon test; box plot center lines represent the median, box edges represent the first and third quartiles, and whiskers indicate minimum and maximum values).
(k) Quantification of H3K27me3, binned into 1 kb regions upstream of the gene body of genes downregulated in H3K36M samples, ISC-associated genes, and goblet cell-associated genes (Wilcoxon test; box plot center lines represent the median, box edges represent the first and third quartiles, and whiskers indicate minimum and maximum values).

2.2.4 Suppression of H3K36 methylation induces accumulation of abnormal secretory cells

Previous work in the hematopoietic system demonstrated that suppressing H3K36 methylation led to distinct defects in differentiation, characterized by the accumulation of stem and progenitor cells[56]. Given that Paneth and goblet cells share a common precursor, I next asked whether abnormal LYZ1-expressing cells in the villi of H3K36M mice might also express genes characteristic of goblets cells. Co-immunofluorescence for TFF3, a marker of goblet cells and LYZ1, a Paneth-cell marker, demonstrated the presence of TFF3/LYZ1 double-positive cells in H3K36M villi, which were not detectable in the villi of H3 control intestines (Fig. 2.4a). Of note, intermediate cells expressing genes associated with both goblet and Paneth cells have been identified in wildtype mice[102,103]. These cells are thought to represent a fleeting goblet/Paneth cell precursor, are rare, and reside only in intestinal crypts[102,103]. However, in H3K36M intestines, these double-positive cells were readily detectable and occurred predominantly in the villus (Fig. 2.4a). To examine these cells further, I performed transmission electron microscopy on sections of WT and H3K36M intestines. In WT intestine sections, I identified goblet cells with characteristic light granules in the villus, and Paneth cells with dense granules in the crypt (Fig. 2.4b, left and middle panels). By contrast, I noted villus cells in the H3K36M intestine that contained mixed granule types and had a morphology reminiscent of intermediate goblet/Paneth precursor cells, in line with immunofluorescence data (Fig. 2.4a,b, right panel). Together, these data suggest that suppressing H3K36 methylation prevents proper maturation of a goblet/Paneth secretory progenitor, leading to its abnormal accumulation in the villi of intestines from H3K36M mice.

Bulk RNA-seq analysis suggested that a gene expression signature characteristic of Paneth cells was modestly enriched in the intestine of H3K36M-expressing mice (Fig. 2.3c). This finding was surprising, given that H3K36 methylation is enriched at genes associated with specialized cells and appears to reinforce their expression; however, I reasoned that perhaps the accumulation of an immature secretory cell precursor in H3K36M mice could account for this observation. To test this possibility, I sought to define gene expression signatures characteristic of immature and mature Paneth cells under homeostatic conditions. We therefore isolated phenotypic Paneth cells from a Defa4Cre/+; Rosa26-LSL-

tdTomato reporter mouse and performed single cell RNA sequencing. My analysis partitioned the cells into three clusters (Fig. 2.4c). I identified one cluster as immature, based on the expression of immature secretory genes *Spink4*[104] and *Mmp7*[104], as well as the co-expression of goblet cell genes, including *Muc2* (Fig. 2.4c-e). Conversely, I identified two other clusters that expressed higher levels of mature Paneth cells markers, including multiple α-Defensins and *Lyz1* (Fig. 2.4c-e). From these data, I constructed gene sets characteristic of each cluster and performed gene set enrichment analysis on H3K36M and WT H3 samples. I observed a striking increase in the immature Paneth cell signature in H3K36M-expressing intestinal epithelial cells and a corresponding decrease in the mature Paneth cell signatures (Fig. 2.4f). These data support my findings that loss of H3K36 methylation disrupts the expression of genes related to specialized cell function and suggest the accumulation of abnormally localized, intermediate secretory progenitors in H3K36M mice.

Figure 2.4

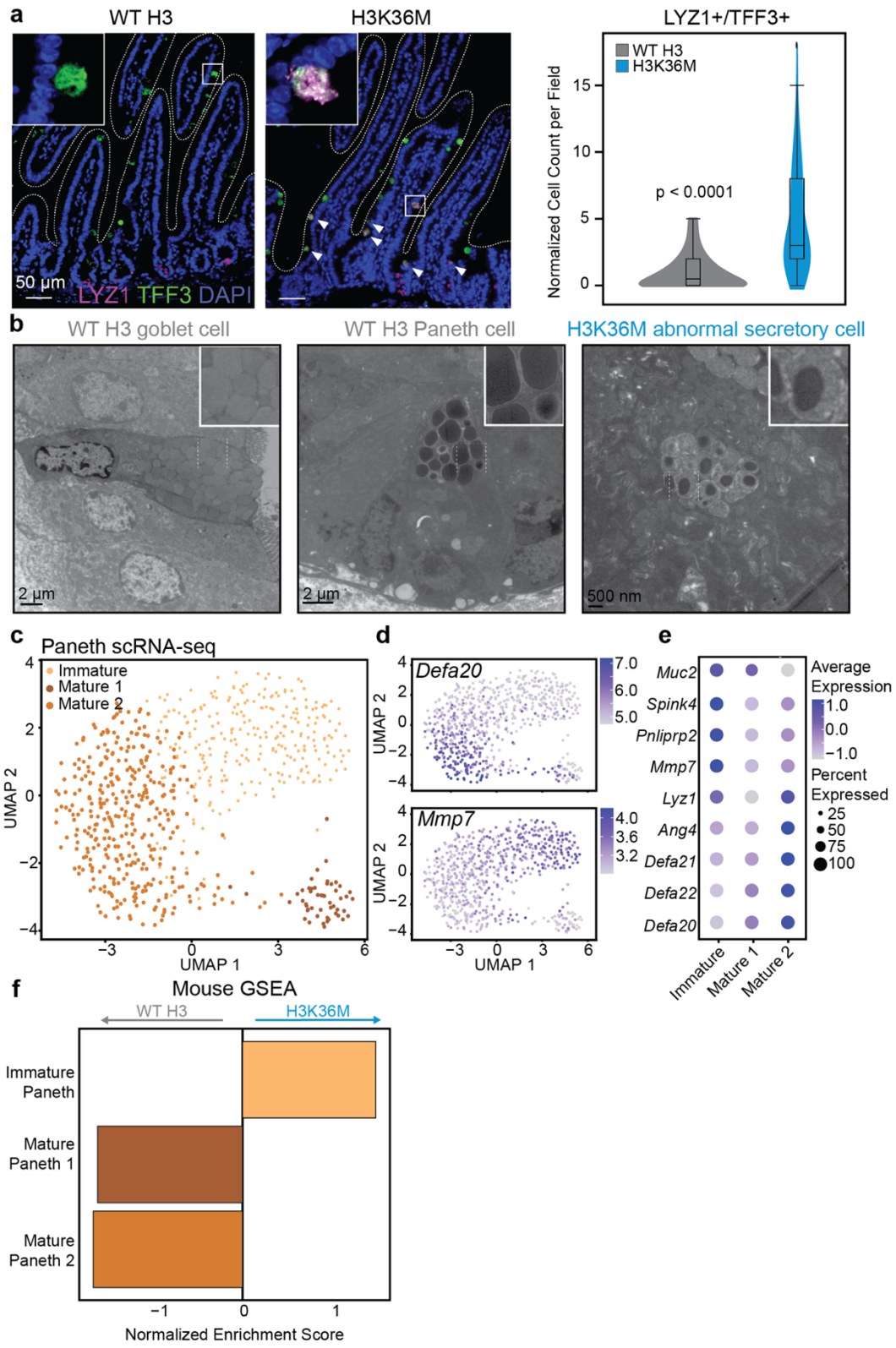
a
WT H3
H3K36M
LYZ1+/TFF3+
WT H3
H3K36M
Normalized Cell Count per Field
p < 0.0001
50 μm
LYZ1 TFF3 DAPI
b
WT H3 goblet cell
WT H3 Paneth cell
H3K36M abnormal secretory cell
2 μm
2 μm
500 nm
c
Paneth scRNA-seq
Immature
Mature 1
Mature 2
UMAP 1
UMAP 2
d
Defa20
Mmp7
UMAP 1
UMAP 2
e
Muc2
Spink4
Pnliprp2
Mmp7
Lyz1
Ang4
Defa21
Defa22
Defa20
Immature
Mature 1
Mature 2
Average Expression
Percent Expressed
f
Mouse GSEA
WT H3
H3K36M
Immature Paneth
Mature Paneth 1
Mature Paneth 2
Normalized Enrichment Score

Figure 2.4. Suppressing H3K36 methylation induces the accumulation of abnormal secretory cells.

(a) Left, representative immunofluorescence images for LYZ1 and TFF3 on WT H3 and H3K36M intestine sections after four weeks dox induction (n = 5 mice each). Right, quantification of $LYZ1^{+}/TFF3^{+}$ cells (n = 10 images per mouse; unpaired two-tailed student's t-test; box plot center lines represent the median, box edges represent the first and third quartiles, and whiskers indicate minimum and maximum values).

(b) Representative transmission electron microscopy images of a WT H3 goblet cell (left, scale bar 2 μm), WT H3 Paneth cell (middle, scale bar 2 μm) and H3K36M intermediate cell found in the villus (right, scale bar 500 nm). The inset shows granules in each respective cell type (n = 3 mice each).

(c) UMAP representation for unsupervised clustering of 3 distinct Paneth cell clusters sorted from WT mice.

(d) UMAP representation from panel c overlaid with expression values for the mature Paneth cell gene *Defa20* and immature Paneth cell gene *Mmp7*. Dark purple indicates maximum gene expression, while light purple indicated low or no expression in log-normalized unique molecular identifier counts.

(e) Expression level and percent of cells in each cluster expressing the indicated genes.

(f) Gene set enrichment analysis based on RNA-seq from WT H3 and H3K36M intestines after four weeks dox induction using gene sets established from Paneth cell scRNA-seq clusters.

2.2.5 Organoid systems support a role for H3K36 methylation in intestinal homeostasis

To confirm that the intestinal cell fate phenotypes that I observed in mice are not a secondary effect, arising from H3K36M-driven defects in other tissues, I derived intestinal organoids, consisting of only intestinal epithelial cells, from uninduced WT H3 or H3K36M mice. I treated the organoids with doxycycline for up to eight weeks, and performed bulk RNA-sequencing, CUT&Tag, and immunofluorescence (Fig. S4a). Organoids from H3K36M mice expressed H3K36M in every cell upon doxycycline induction and showed loss of H3K36 methylation as expected (Fig. S4b,c). Gene set enrichment analysis revealed the loss

of gene expression signatures characteristic of ISCs, goblet cells, and mature Paneth cell population 1 in H3K36M organoids, and an increased signature characteristic of immature Paneth cells (Fig. S4d). In line with these results, immunofluorescence on H3K36M organoids for MMP7, a marker of Paneth cells, and MUC2, a marker of goblet cells, confirmed the accumulation of cells that were double-positive for Paneth and goblet cell-associated proteins, similar to the H3K36M mice (Fig. S4e). Likewise, CUT&Tag analysis demonstrated global loss of both H3K36me2 and H3K36me3, with a corresponding increase in H3K27me3 at genes downregulated in H3K36M organoids compared to WT H3 control (Fig. S4f-k). Together, this work recapitulates my observations in mice using an orthogonal, organoid-based system.

2.2.6 Suppressing H3K36 methylation activates a regenerative gene expression signature

While H3K36 methylation is generally associated with active chromatin, I observed increased expression of a subset of genes (351 transcripts) upon its suppression, which is in line with previous studies[36,56,100,105]. Correlating with their expression, upregulated genes retained a higher level of H3K36me3 in the H3K36M context (Fig. 2.3b). Given that H3K36M intestinal epithelial cells lose expression of functional, cell fate-associated genes, I hypothesized that upregulated genes may reflect a more plastic cell fate. To test this possibility, I performed gene set enrichment analysis using a panel of transcriptional signatures that represent a regenerative state induced by injury or infection[106–108]. I also included a fetal gene expression signature as many of the genes upregulated following injury are highly expressed during development[82]. Supporting my hypothesis, gene expression signatures characteristic of these highly plastic states were significantly enriched in H3K36M-expressing intestinal epithelial cells. (Fig. 2.5a). Established markers of regeneration, such as *Clu, Tubb6, Areg,* and *Cldn4*, were correspondingly upregulated (Fig. 2.5b). To understand the dynamics of gene expression changes that take place following H3K36M induction, I analyzed an RNA-seq time course in H3K36M and WT H3 organoids (Fig. S4a). Principal component analysis (PCA) revealed a distinct trajectory for gene expression in H3K36M organoids that departed from WT H3 organoids (Fig. 2.5c). Further analysis revealed that regenerative genes were rapidly and progressively

upregulated following induction (Fig. 2.5d), confirming and extending my observations in vivo. Specifically, regenerative and fetal gene expression signatures were enriched in H3K36M samples compared to WT H3 control organoids (Fig. S5a), with increased expression of *Clu* and other established markers of regeneration (Fig. 2.5d, labeled rows). During culture of H3K36M organoids, I also observed a distinct morphological change, characterized by the appearance of large, cystic organoids with fewer buds compared to WT control (Fig. 2.5e). This morphology is reminiscent of fetal intestinal organoids, which are likewise cystic[109,110]. Together, these data suggest that suppressing H3K36 methylation initiates gene expression and morphological features associated with highly plastic cell states.

Figure 2.5

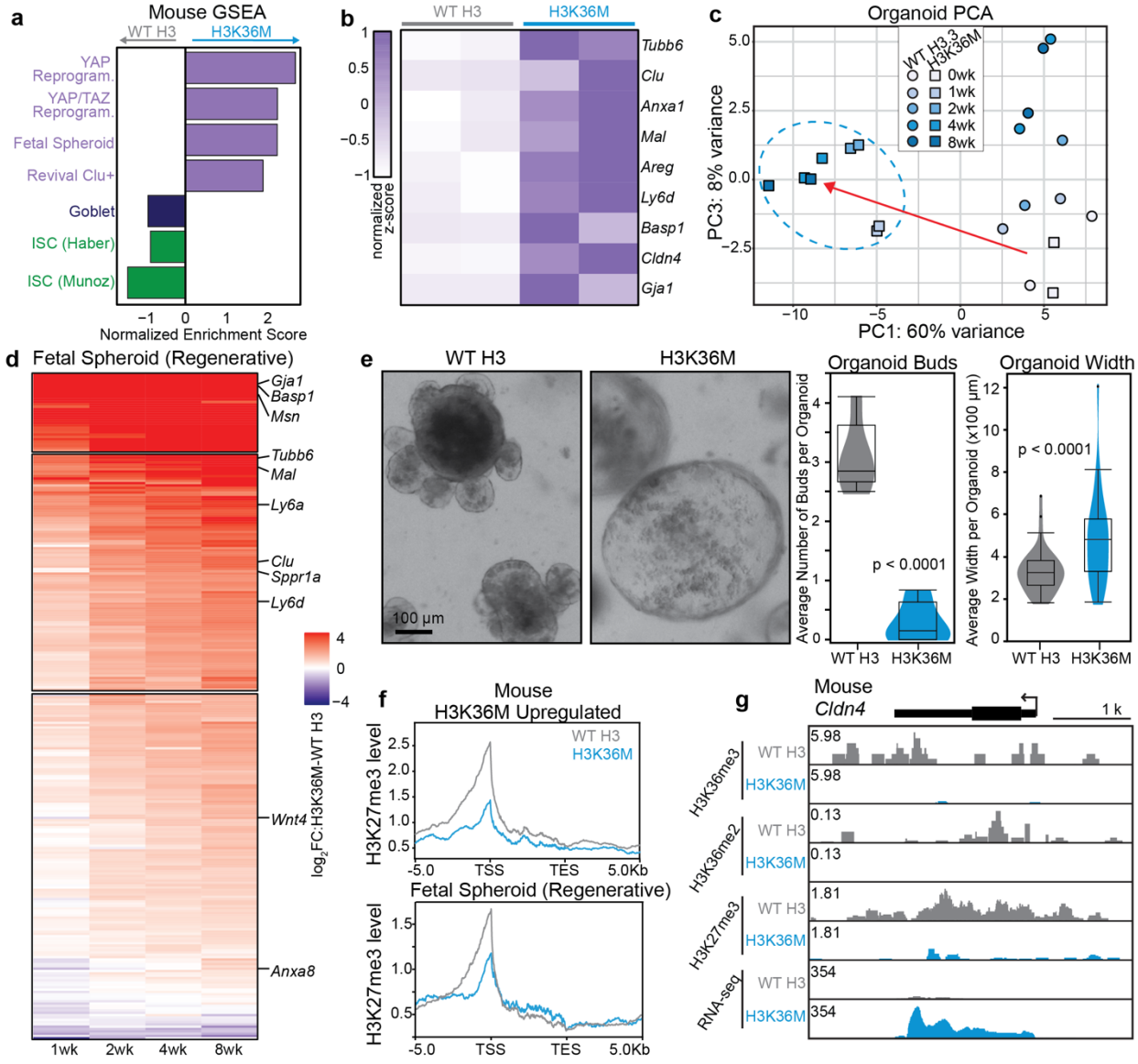

Figure 2.5. Suppressing H3K36 methylation activates a regenerative gene expression signature.

(a) Gene set enrichment analysis based on RNA-seq from WT H3 and H3K36M intestines after four weeks dox induction, using published regenerative (purple) and mature cell type gene sets[96,106–109,111].

(b) Gene expression normalized z-score from WT H3 or H3K36M mice for the indicated regenerative genes.

(c) Multidimensional scaling analysis from RNA-seq for WT H3 and H3K36M organoids over an 8-week time course (n = 2 biological replicates per condition). The blue dashed line indicates H3K36M-induced samples.
(d) Gene expression for WT H3 and H3K36M organoids over an 8-week time course for a published regenerative gene set[109]. Notable regenerative markers are labeled.
(e) Left, representative brightfield images of WT H3 and H3K36M intestinal organoids after 8 weeks of doxycycline induction (n = 2 biological replicates each; scale bar 100 μm). Right, quantification of organoid budding and width in WT H3 and H3K36M organoids (n=10 images each; unpaired two-tailed student's t-test).
(f) Meta-analysis of H3K27me3 at genes upregulated in H3K36M samples (top) and at a published set of regenerative genes[109] (bottom) (5kb window around the TSS and TES).
(g) Representative gene tracks for H3K36me3, H3K36me2, H3K27me3, and gene expression for *Cldn4*, a regenerative marker, in WT H3 and H3K36M mice.

Loss of H3K36 methylation near cell type-associated genes leads to inappropriate spreading of H3K27me3 and transcriptional repression at that genomic locus (Fig. 2.3); however, I and others have observed a corresponding decrease of H3K27me3 over Polycomb targets, presumably due to titration of PRC2 away from these sites and into regions that lose antagonistic H3K36 methylation marks[36,41,56,100,105]. Indeed, I observed inappropriate spreading of H3K27me3 into intergenic regions following H3K36M expression (Fig. 2.3d-k and Fig. S3h-j). To explore whether this mechanism could explain the upregulation of regenerative genes in H3K36M-expressing intestinal epithelial cells, I analyzed CUT&Tag data from mouse intestinal epithelial cells. Meta-analysis of H3K27me3 revealed that genes upregulated in H3K36M samples, and specifically, regenerative genes, had a sharp H3K27me3 peak at their promoters in WT H3 mice, suggesting that they are repressed, at least in part, by Polycomb activity under normal growth conditions (Fig. 2.5f,g and Fig. S5b). Accordingly, H3K27me3 decreased substantially at promoters of these genes in H3K36M-expressing cells (Fig. 2.5f,g and Fig. S5b). I confirmed these trends using WT and H3K36M organoids as well (Fig. S5c). Together, these data suggest a mechanism whereby the loss of H3K36 methylation relieves a barrier for the spreading of H3K27me3, which in turn dilutes PRC2 from regenerative genes and activates their expression.

2.2.7 Suppressing H3K36 methyltransferases partially phenocopies H3K36M

As an orthogonal approach to suppress H3K36 methylation, I transduced intestinal organoids with short hairpin RNAs (shRNAs) targeting either *Nsd2*, which deposits H3K36me1/2, or *Setd2*, which deposits H3K36me1/2/3. Western blot analysis confirmed that *Nsd2* and *Setd2* knockdown reduced H3K36me2 and H3K36me3, respectively (Fig. S6a,b), though not to the same extent as H3K36M expression. Suppression of either methyltransferase moderately but significantly reduced the expression of secretory markers, such as *Muc2* and *Lyz1*, and the stem cell marker *Lgr5* (Fig. S6c,d). Although fewer in number compared to H3K36M samples, I identified abnormal secretory cells marked by both Paneth and goblet cell markers in *Nsd2* and *Setd2* knockdown organoids (Fig. S6e). I also observed increased expression of the regenerative-associated gene, *Clu* (Fig. S6c,d). *Nsd2* and *Setd2* knockdown organoids appeared cystic, with increased size and fewer buds compared to shLuc control organoids (Fig. S6f,g), consistent with a regenerative state. These findings suggest that both H3K36me2 and H3K36me3 are important for reinforcing expression of cell type-associated genes and their suppression partially phenocopies expression of H3K36M.

2.2.8 Injury-induced regeneration leads to a redistribution of H3K36 methylation

I next sought to determine whether H3K36 methylation is associated with a physiological model of regeneration. To this end, I irradiated wildtype intestinal organoids and harvested samples at 24, 48, and 96 hours for both RNA-seq and CUT&Tag (Fig. 2.6a). At 24 and 48 hours, regeneration is underway; however, by 96 hours, intestinal organoids have recovered from injury and are re-entering a homeostatic state[112]. This trajectory was reflected by PCA of RNA-seq data, which revealed that non-irradiated organoids clustered with the 96-hour organoids, while 24- and 48-hour post-irradiation organoids clustered separately (Fig. 2.6b). Interestingly, PCA also revealed that 24- and 48-hour post-irradiation organoids were similar to H3K36M organoids by principal component 2, suggesting similarity in gene expression between the two treatments (Fig. 2.6b). The trajectory of regenerating cells was further confirmed by gene expression analysis for key

markers, as *Clu* levels increased at 24 and 48 hours post-irradiation but returned to near homeostatic levels by 96 hours (Fig. 2.6c). Conversely, *Lgr5* decreased dramatically at 24 and 48 hours after injury but returned to homeostatic levels at 96 hours (Fig. 2.6c). Gene set enrichment analysis further demonstrated the enrichment of regenerative gene expression signatures after 24 and 48 hours of irradiation with a corresponding depletion of ISC gene sets (Fig. 2.6d). These data suggest that suppressing H3K36 methylation induces gene expression changes similar to irradiation-induced regeneration.

Figure 2.6

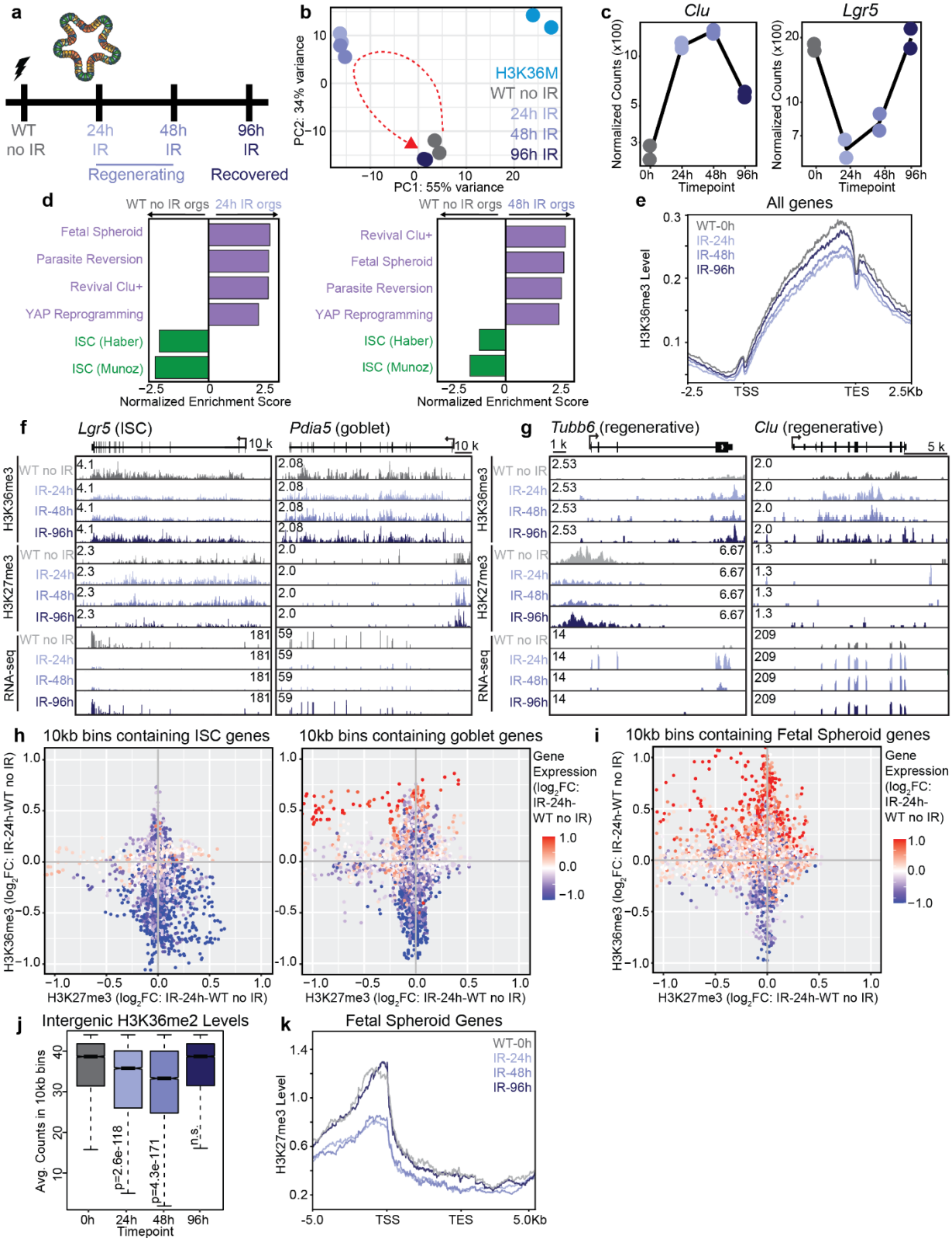

Figure 2.6. Injury-induced regeneration induces widespread remodeling of H3K36 methylation.

(a) A schematic of the experimental design for irradiation and harvest of WT organoids.
(b) Multidimensional scaling analysis based on RNA-seq from WT H3, H3K36M, and irradiated organoids. Each circle represents a biological or independent replicate.
(c) Time course analysis following organoid irradiation for Clu, a marker of regeneration, and Lgr5, a marker of ISCs. Each circle represents an independent replicate.
(d) Gene set enrichment analysis based on RNA-seq analysis comparing non-irradiated and irradiated organoids at 24-hours post-irradiation (left) and 48-hours post-irradiation (right), using published regenerative gene sets, or published mature cell type gene sets[82,96,107–109,111].
(e) Meta-analysis of H3K36me3 over all genes in untreated and irradiated WT organoids (representative trace for 2 independent replicates).
(f) Representative gene tracks for Lgr5, a marker of ISCs, and Pdia5, a marker of goblet cells, in untreated and irradiated WT organoids (representative track for 2 independent replicates).
(g) Representative gene tracks for Tubb6 and Clu, markers of intestinal regeneration, in untreated and irradiated WT organoids (representative track for 2 independent replicates).
(h) Differential methylation analysis between WT non-irradiated organoids and 24 hour post-irradiation organoids in 10kb bins for published ISC- and goblet cell-associated genes [96]. The color of each dot represents $\log_2$FC gene expression in that bin.
(i) Differential methylation analysis between WT non-irradiated organoids and 24 hour post-irradiation organoids in 10kb bins for published regenerative genes [109]. The color of each dot represents $\log_2$FC gene expression in that bin.
(j) Quantification of H3K36me2 binned into 10,000 randomly selected 10 kb intergenic regions in WT or 24-, 48-, and 96-hour post-irradiation organoids (Wilcoxon test; box plot center lines represent the median, box edges represent the first and third quartiles, and whiskers indicate minimum and maximum values).
(k) Meta-analysis of H3K27me3 in WT or 24-, 48-, and 96-hour post-irradiation organoids over a published regenerative gene set[109] (representative trace for 2 independent replicates).

Given the similarities in gene expression between H3K36M and irradiated organoids, I examined CUT&Tag data to determine whether H3K36 methylation likewise changed during injury-induced regeneration. Meta-analysis revealed a global decrease in H3K36me3 over gene bodies upon irradiation, which recovered by 96 hours (Fig. 2.6e). To understand the mechanistic basis for this finding, I plotted the expression of H3K36

methyltransferases, *Setd2* and *Nsd2*, over the regeneration time course. Consistent with H3K36 methylation dynamics, both genes were downregulated at 24 and 48 hours post-irradiation but returned to normal levels at 96 hours (Fig. S7a). Notably, genes related to specialized cell function, including *Lgr5* (ISC) and *Pdia5* (goblet cell), reflected this trend, with a marked decrease of H3K36me3 over the gene body during regeneration that returned to normal at 96 hours post-irradiation (Fig. 2.6f). In line with our observations in H3K36M cells, H3K27me3 was correspondingly increased over *Lgr5* and *Pdia5*, which returned to baseline levels after 96 hours (Fig. 2.6f). By contrast, H3K36me3 was retained or increased at 24 and 48 hours post-irradiation over regeneration-associated genes, like *Tubb6* and *Clu* (Fig. 2.6g), consistent with results in H3K36M samples (Fig. 2.3b). Correspondingly, H3K27me3 decreased appreciably over *Tubb6* (Fig. 2.6g), suggesting that, as in H3K36M samples, titration of PRC2 away from regenerative genes occurs upon reduction of antagonistic H3K36 methylation across the genome. In turn, these chromatin profiles corresponded to changes in gene expression (i.e., upregulation of *Tubb6* and *Clu,* downregulation of *Lgr5* and *Pdia5* at 24- and 48-hour timepoints) (Fig. 2.6f,g). To expand these findings to a larger set of genes and study chromatin dynamics, I plotted the fold-change of H3K36me3 at 24 hours post-irradiation against the fold-change of H3K27me3 in 10kb bins containing regenerative-, ISC-, or goblet-related genes (Fig. S7b). For regenerative genes, I observed a distinct increase in the percentage of bins that gained H3K36me3 and lost H3K27me3 at 24 and 48 hours (Fig. S7b; upper left quadrant of graphs in top row). Notably, this association is lost at 96 hours after irradiation, suggesting that changes in these histone modifications direct regeneration (Fig. S7b). I noted the opposite trend for ISC- or goblet-associated genes, where most bins showed a loss of H3K36me3 and gain of H3K27me3 (Fig. S7b; lower right quadrant of graphs in middle and bottom rows). By overlaying RNA-seq data on these plots, I observed a strong correlation between H3K36me3 levels and gene expression (Fig. 2.6h,i and Fig. S7c). Together these data suggest that H3K36 methylation is suppressed during irradiation-induced injury and these changes correlate with gene expression related to the regenerative response.

To determine whether similar chromatin and gene expression changes take place during regeneration in vivo, I irradiated mice and harvested intestines for RNA-seq and CUT&Tag at 2 and 3 days post-irradiation (Fig. S8a). I note that re-entry into a homeostatic state takes place at a later time point in vivo and is therefore not captured by

this time course. In line with organoid experiments, expression of *Clu* increased upon irradiation, while *Lgr5* decreased (Fig. S8b). Likewise, gene set enrichment analysis revealed enrichment of regenerative gene sets at 2 and 3 days post-irradiation, and depletion of ISC gene sets, confirming injury-induced regeneration (Fig. S8c). Following irradiation, H3K36me3 and H3K36me2 were reduced, particularly at genes associated with specialized function (i.e., ISC- and goblet-related genes) and I observed increased H3K27me3 at these loci, while the opposite trend occurred at regenerative genes (Fig. S8d-g). Consistent with organoid experiments, both *Setd2* and *Nsd2* were downregulated following irradiation, suggesting that transcriptional regulation of H3K36 methyltransferases contribute to decreased H3K36 methylation following injury (Fig. S8h).

My analyses in H3K36M mice and organoids revealed substantial loss of H3K36me2 and corresponding redistribution of H3K27me3. I therefore asked whether similar chromatin changes occur in physiological regeneration. Indeed, I found that H3K36me2 levels decreased over intergenic regions, as in H3K36M (Fig. 2.6j and Fig. S8i). Correspondingly, H3K27me3 was depleted at the transcription start sites of regenerative genes following irradiation, correlating with gene expression in both mice and organoids (Fig. 2.6k and Fig. S8j). Notably, H3K27me3 levels recover in organoids 96 hours after irradiation, as homeostasis is restored (Fig. 2.6k). Together with functional analyses in H3K36M-expressing intestinal epithelial cells, my findings support a model whereby depletion of H3K36 methylation and subsequent redistribution of H3K27me3 silences mature cell type-associated genes. At the same time, apparent titration of PRC2 into intergenic regions relieves repression of regenerative genes, facilitating a transition to a more plastic state.

2.3 Discussion

In mammals, the intestinal epithelium has primary roles in nutrient absorption, barrier function, immune homeostasis, and defense against pathogens[94,113]. To perform these diverse duties, the intestine contains highly specialized cell types with distinct functional and transcriptional profiles. Maintaining the proper balance of these specialized cells is crucial to the organ's function and requires precisely regulated differentiation from

plastic stem and progenitor cells. Cell fate specification in the intestine is initiated by key signaling networks, including the Wnt, Notch, and BMP pathways[68–72,114]; yet, while many signals that induce intestinal cell fate are known, the regulatory mechanisms that control their activity and subsequently maintain cell type-specific expression patterns remain elusive. Previous work demonstrated that epigenetic elements that typically distinguish lineages in other tissues, such as regions of open chromatin, repressive histone modifications, DNA methylation, and marks of active enhancers (e.g. H3K4 methylation and H3K27 acetylation) are surprisingly similar between enterocyte progenitors, secretory progenitors, and ISCs [67,85–91]. Mature intestinal epithelial cells, particularly secretory cells, exhibit modest but detectable differences in chromatin accessibility at a subset of putative enhancers[85,87]. However, many of these regions lack marks of active enhancers and chromatin accessibility differences are resolved rapidly after dedifferentiation is induced[85]. These observations suggest that the chromatin barrier to cell fate change is low in the intestinal epithelium, which begs the question of how these cells maintain their identity. Here, I report that unlike other chromatin modifications, H3K36me3 profiles are distinct between intestinal epithelial cell types. Pronounced differences in H3K36me3 occurred at genes related to specialized cell fate and correlated with gene expression, suggesting a role for H3K36me3 in reinforcing cell fate. At a functional level, disrupting H3K36 methylation led to aberrant spreading of H3K27me3, diminished expression of cell type-associated genes, and a striking defect in intestinal homeostasis, characterized by a loss of mature goblet and Paneth cells (Fig. S9a,b). Notably, only a subset of genes was downregulated following suppression of H3K36 methylation, and this subset was enriched for gene signatures related to specialized cell function. These data suggest that H3K36 methylation is a primary regulator in intestinal epithelial cells that reinforces gene expression to maintain specialized cell identity. Consistent with this notion, loss of H3K36 methylation led to the accumulation of abnormal secretory progenitor cells in the intestinal villus, that resembled an intermediate goblet/Paneth cell precursor. Together, these data suggest that H3K36 methylation is necessary for maintaining cell fate, and its disruption leads to a more plastic state.

Regenerative tissues are particularly vulnerable to damage that compromises the stem cell compartment. Without highly plastic cells to replenish mature cell types, homeostasis cannot be maintained, which ultimately leads to tissue failure. Different

tissues employ different mechanisms to overcome this challenge. For example, damage in the hematopoietic system induces stem cell proliferation to repopulate the stem cell pool. This strategy maintains the separation between the stem cell compartment and specialized cells. Consequently, molecular features that reinforce cell identity (e.g., chromatin modifications) are vastly different between hematopoietic stem cells and their progeny[115–118]. By contrast, the intestinal epithelium relies upon dedifferentiation of specialized cells, including most cell types in the secretory lineage, to replace damaged tissue. Dedifferentiation is thought to be key for the regenerative process and over time, these regenerative cells transition back into multipotent ISCs and restore intestinal homeostasis. In this way, intestinal epithelial cells are highly plastic and capable of rapidly changing cell identity. A major outstanding question in the field is how intestinal epithelial cells maintain the delicate balance between specialized function and plasticity. Given that loss of H3K36 methylation extinguished specialized gene expression programs, I hypothesized that it might also lead to a more plastic cell state. Consistent with this hypothesis, my analyses confirmed that suppressing H3K36 methylation rapidly induced a regenerative gene expression profile. Moreover, H3K36M-expressing organoids adopted a rounded, cystic appearance, characteristic of highly plastic fetal organoids. In further support of this notion, H3K36 methylation decreased dramatically following injury-induced regeneration, concomitant with the loss of gene expression patterns characteristic of specialized cells. H3K27me3 was correspondingly redistributed following injury-induced irradiation, paralleling my observations in H3K36M-expressing cells (Fig. S9b). Importantly, these chromatin changes returned to normal homeostatic levels as regeneration concluded, presumably directing expression of cell type-associated genes while restricting the expression of plastic, regenerative genes. To my knowledge, this is the first example of a histone modification associated with regeneration in the intestine.

Mechanistically, H3K36 methylation controls cell fate and plasticity in the intestinal epithelium through two distinct regulatory modes, both involving H3K27me3 (Fig. S9a,b). Under homeostatic conditions, H3K36me3 acts as an antagonistic boundary for PRC2, restricting the inappropriate spread of H3K27me3 into the gene bodies of cell type-associated genes and preventing their silencing. H3K36me2 likewise acts a barrier to the spreading of H3K27me3, which maintains PRC2 at Polycomb targets, including regenerative genes. Upon induction of regeneration, H3K36me3 is globally reduced,

permitting silencing of cell type-associated genes through Polycomb activity. At the same time, loss of H3K36me2 genome wide, but particularly in intergenic regions, drives the redistribution of PRC2 away from its targets in specialized cells. These targets include regenerative genes, like *Clu*, *Cldn4,* and *Tubb6,* which are correspondingly upregulated. In this way, the genome acts as a buffering mechanism during regeneration to titrate PRC2 away from genes needed to restore plasticity, which relies on H3K36 methylation.

Although H3K27me3 profiles are remarkably similar between intestinal crypt and villus cells[92], direct perturbation of enzymes that add or remove H3K27 methylation has variable effects on intestinal epithelial cell fate. For example, deletion of H3K27 demethylases, *Kdm6a* and *Kdm6b*, induced modest gene expression changes in intestinal epithelial cells but had no functional effect on homeostasis or regeneration[93]. Likewise, knockout of *Ezh2*, the primary H3K27 methyltransferase, had no apparent effect on intestinal epithelial cell fate[119]. By contrast, disrupting PRC2 through EED knockout led to reduced intestinal stem cells[119,120] and an accumulation of abnormal secretory cells[119], supporting a role for H3K27me3 in maintaining specialized cell function. EED knockout also led to defects in injury-induced regeneration[120], suggesting that complete elimination of H3K27me3 prevents reacquisition of plasticity. There is a growing appreciation that many chromatin modifiers have roles outside of their function in regulating histone modifications and disruption of one histone methyltransferase may be partially or fully compensated by other enzymes, which may explain these discordant findings[50,51]. However, a more nuanced mechanism may also resolve these findings. Regeneration requires not only the activation of regenerative genes, but the silencing of lineage-associated genes (i.e., a concept known as paligenosis[121]), which is likely compromised by complete loss of H3K27me3. I propose that regeneration requires the concerted gain of H3K27me3 at cell type-associated genes with loss of H3K27me3 at regenerative genes and these dynamics are regulated by H3K36 methylation. Whether this dual mechanism is likewise involved in other cell responses, particularly those involving cell fate transitions and plasticity, is unknown but represents an exciting avenue for future research.

An additional unresolved question is how specificity of H3K36 methylation is achieved in different cell states (i.e., how is H3K36me3 directed to cell type-associated genes in specialized cells and regenerative genes during regeneration). I note that SETD2,

the methyltransferase responsible for H3K36me3, associates with transcriptional machinery, which is thought to direct its activity to the gene bodies of actively expressed genes. I postulate that signaling pathways, induced either during differentiation or during regeneration, activate transcription of specific genes, which directs deposition of H3K36me3 in the gene bodies. Once established, H3K36me3 acts as a crucial mechanism to prevent silencing by Polycomb and reinforce transcription of cell fate-instructive genes. This effectively acts as a feedforward mechanism to stabilize gene expression.

Histone modifications provide regulatory diversity that is crucial during differentiation and homeostasis. Based on my data, I propose a paradigm for regulating cell plasticity that relies upon H3K36 methylation. My model provides a mechanism for specifying mature cell types, but also accounts for the ability of intestinal stem cells to rapidly dedifferentiate. This model is further supported by a recent report that suppressing H3K36 methylation in mouse embryonic fibroblasts greatly increases the efficiency of reprogramming to pluripotency[105]. Similar to my observations in the intestinal epithelium, loss of H3K36 methylation facilitates the silencing of genes related to fibroblast cell fate and the upregulation of genes related to the highly plastic, pluripotent state[105]. Conversely, suppressing H3K36 methylation prevented the acquisition of specialized cell fates in gastruloids[105], embryoid body assays[56], and the directed differentiation of chondrocytes, adipocytes, and osteocytes[41]. I therefore propose that H3K36 methylation is a general mechanism for restricting plasticity during development and homeostasis. Finally, I note that increased plasticity and failure to differentiate are hallmarks of cancer, and H3K36M expression is associated with chondroblastoma, giant cell bone tumors, soft-tissue sarcoma, and head and neck squamous cell carcinoma[41,53,54,59]. My efforts to understand how H3K36 methylation controls plasticity may clarify its role in tumorigenesis and lay the foundation for future work in this area.

2.4 Methods

2.4.1 Mice

Col1a1-tetO-H3.3:R26-M2rtTA (B6;129-*Gt(ROSA)26Sor*$^{tm1(rtTA*M2)Jae}$ *Col1a1*$^{tm3(tetO-H3f3a)Hoch}$/J, JAX stock no. 034364)[56]; Col1a1-tetO-H3.3K36M:R26-M2rtTA (B6;129-*Gt(ROSA)26Sor*$^{tm1(rtTA*M2)Jae}$ *Col1a1*$^{tm4(tetO-H3f3a*K36M)Hoch}$/J; JAX stock no. 034365)[56]; Defensin-alpha 4-Cre knockin (Defa4^{Cre})[122,123], Lgr5$^{EGFP\text{-}ires\text{-}CreERT2}$ (B6.129P2-*Lgr5*$^{tm1(cre/ERT2)Cle}$/J, JAX stock no. 008875)[124], Rosa26^{tdTomato} (B6.Cg-*Gt(ROSA)26Sor*$^{tm9(CAG\text{-}tdTomato)Hze}$/J, JAX stock no. 007909)[125], NeuroD1^{Cre} (Tg(Neurod1-cre)1Able/J, JAX stock no. 028364)[126], MUC2-mCherry (transgene RedMUC2^{98trTg})[127], transgene TRPM5-GFP[128] and C57BL/6J (JAX stock no. 000664) were used in this study. All alleles were confirmed by PCR genotyping. Mice were housed in ventilated and automated watering cages with a 12-hour light cycle under specific, pathogen-free conditions. Protocols for mouse usage were approved by the University of Colorado IACUC protocols (no. 2688, Boulder campus; no. 00084, Anschutz campus). Adult mice of both sexes were used for analyses. NeuroD1-Cre mice were a gift from Dr. Stephen Liberles, Dept of Cell Biology, Harvard Medical School. TRPM5-GFP reporter mice were a gift from Drs. Eric Larson and Sue Kinnamon, Dept. of Otolaryngology, Rocky Mountain Taste and Smell Center, University of Colorado Anschutz Medical Campus.

2.4.2 Animal Treatment Protocols and Tissue Collection

For transgene induction, adult (7-16 week old) homozygous Col1a1-tetO-H3.3K36M:R26-M2rtTA (termed H3K36M) and control Col1a1-tetO-H3.3:R26-M2rtTA (termed WT H3) mice were treated with 2 mg/ml doxycycline (Sigma D9891) and 5% sucrose in drinking water for 4 weeks. For irradiation treatment, adult (8-12 week-old) C57BL/6J mice were exposed to 12 Gy whole-body irradiation using a MultiRAD350 from Precision X-Ray Irradiation to induce epithelial injury in vivo.

For histologic analysis, intestinal tissue was removed rapidly, flushed with ice-cold phosphate-buffered saline (PBS), opened longitudinally, Swiss-rolled, and then fixed in cold

4% Paraformaldehyde (PFA) in PBS overnight at 4°C. Intestinal tissue was then processed and paraffin embedded. For epithelial cell elution, intestinal tissue was removed rapidly, flushed with ice-cold PBS, opened longitudinally, and then region-specific segments (duodenum, jejunum, and ileum) were cut into 0.5 cm segments, placed in chelation buffer (PBS containing 20 mM EDTA [Fisher Scientific S311] and 1 mM DTT [Fisher Scientific BP172-5]), and rocked for 30 minutes at 4˚C. Epithelial cells were isolated by vigorous shaking in ice-cold PBS, sequentially filtered through 100 and 40 μm cell strainers, and then centrifuged at 600g for 5 min at 4°C. Cell pellets were resuspended in 2 ml ice-cold PBS, aliquoted, centrifuged at 600 x g at 4°C, and flash-frozen in liquid nitrogen.

2.4.3 Intestinal Organoids and Treatments

Intestinal crypts were isolated from the duodenum of WT H3 or H3K36M mice and organoids were generated as described previously[83,84]. Briefly, crypts were plated in ice-cold Reduced Growth Factor Basement Membrane Extract (BME) (Cultrex, R&D Systems, Minneapolis, MN) (15 ul) into wells of 48-well plates and grown in 300 ul basal ENR media. The basal ENR culture medium (Advanced Dulbecco's modified Eagle medium/F12 [ThermoFisher 12634020] with 1X penicillin/streptomycin [ThermoFisher 15070063], 10 mM HEPES [ThermoFisher 15630080], 1X Glutamax [ThermoFisher 35050061], 1X B27 [ThermoFisher 17504044], and 1 mM N-acetylcysteine [Sigma-Aldrich A9165]) was supplemented with 50 ng/ml murine recombinant epidermal growth factor (PeproTech 315-09), 100 ng/ml murine recombinant Noggin (PeproTech 250-38), and R-spondin2 (conditioned medium, 5% final volume). R-spondin2-conditioned media was produced using HEK293T cells stably transfected with mouse R-spondin2[129] and provided by Organoid and Tissue Modelling Shared Resource, University of Colorado Anschutz Medical Campus. Media was replaced every 2–3 days. To induce WT H3 or H3K36M gene expression, doxycycline (Sigma D9891, 2ug/ml) was added to the culture medium for at least one week before harvest for analysis. For time course analysis, two biological replicates were analyzed at each timepoint.

For irradiation treatment, WT H3 organoids grown in BME were exposed to 6 Gy irradiation using a Cabinet X-Ray System (Faxitron X-Ray Corporation) at a dose rate of

5.33 rad/minute. Organoids were harvested 24, 48, and 96 hours post-irradiation. Non-irradiated organoids were harvested at timepoint 0 as a control. Two independent replicates were used for each timepoint.

Lentiviral transduction of WT C57BL/6J duodenal organoids was performed as described previously[130–132] with minimal modifications. shRNA lentivirus (pLKO.1-puro) constructs for mouse *Nsd2* and *Setd2* were obtained from the University of Colorado Anschutz Functional Genomics Shared Resource.

2.4.4 Immunohistochemical and Immunofluorescence Staining

Paraffin tissue sections (5 µm) were used for histologic analysis and immunohistochemistry, as previously described[72,123]. Paraffin-embedded organoid sections (5 µm) were prepared from organoids fixed in 4% PFA in PBS overnight at 4°C, placed in Histogel, processed, and then paraffin embedded. Hematoxylin and eosin (H&E) and Periodic acid-Schiff (PAS) staining were performed according to the manufacturer's instructions by the Research Histology core, Pathology Shared Resource. For immunofluorescence staining, sections were deparaffinized in Histo-Clear (National Diagnostics HS200) and rehydrated. Agilent Dako Target Retrieval Solution (Agilent S236984-2) was used for antigen retrieval in a pressure cooker. Slides were blocked using Agilent Dako Protein Block, Serum Free (Agilent X090930-2) for one hour at room temperature. Sections were then stained with MUC2 (SantaCruz sc-15334, 1:200), Lysozyme (Dako A0099, 1:1000), Chromogranin A (Abcam Ab15160-1, 1:500), DCKL1 (Abcam ab109029, 1:2000), TFF3 (Thermo Fisher 14-4758-82, 1:1000), MMP7 (Vanderbilt Antibody and Protein Resource, 1:200). After washing, sections were incubated with Alexa Fluor 568, 647, or 488-conjugated anti-rabbit, rat or mouse IgG (Invitrogen A32723, A32731, A-11011, A-11004, A-21247) and DAPI (VWR 95059). Microscopy and imaging was performed using a Leica DMIL LED inverted fluorescence microscope or an Olympus IX71 inverted fluorescent microscope equipped with a DP74 digital camera and cellSens software. Staining was quantified using CellProfiler 2, with 10 random images quantified per antibody per mouse. Whole mount immunofluorescence staining of intestinal organoids

was performed as described previously[133] and imaged using a Nikon A1 laser scanning confocal microscope.

2.4.5 Electron Microscopy

Freshly isolated duodenal tissue from WT H3 and H3K36M mice was fixed in 4% PFA (Fisher Scientific AC416785000)/2.5% glutaraldehyde (Electron Microscopy Sciences 16316) overnight at 4˚C, post fixed for 1 hour in 1% OsO_4 (Sigma-Aldrich 419494), dehydrated, and Epon embedded. Ultra-thin sections were stained with uranyl acetate and lead citrate and then examined and imaged using a FEI Tecnai T12 Transmission Electron Microscope in the University of Colorado Boulder Electron Microscopy Facility.

2.4.6 Western Blotting

Eluted epithelial cells were prepared for western blotting by nuclear isolation. First, 400 µl of cold nuclear isolation buffer (50 mM Tris-HCl pH 8 [Fisher Scientific AAJ22676A1], 15 mM NaCl [Sigma-Aldrich S5886], 60 mM KCl [Alfa Aesar 11595], 5 mM $MgCl_2$ [Fisher Scientific M33], 1 mM $CaCl_2$ [Acros Organics 423525000], 250 mM sucrose [Thermo Fisher A15583.0E], 1 mM dithiothreitol [Fisher Scientific BP172-5], 0.6% IGEPAL [Sigma-Aldrich I8896]) supplemented with complete protease inhibitors (Roche 04693159001) was gently added to 1 X 10^7cells. The suspension was incubated for 5 minutes on ice. Nuclei were then centrifuged at 960 x g for 5 min. The resulting pellet was gently washed twice in nuclear isolation buffer and lysed in RIPA buffer (50 mM Tris-HCL pH 8 [Fisher Scientific AAJ22676A1], 150 mM NaCl [Sigma-Aldrich S5886], 0.1% SDS [Fisher Scientific BP166], 0.5% sodium deoxycholate [Sigma-Aldrich D6750], 1% Triton X-100 [Aigma-Aldrich T8787], and 1 mM EDTA [Fisher Scientific S311]) supplemented with complete protease inhibitors (Roche 04693159001) and 0.01 U μl^{-1} benzonase (Fisher Scientific 70-746-4). The lysates were then sonicated for 10 cycles (30 seconds pulses with 30 seconds between pulses) using a Bioruptor Pico sonicator (Diagenode). The resulting lysate was cleared by centrifugation for 2 miuntes at 21,000 x g. The supernatant was boiled together with Laemmli sample buffer (100 mg/ml SDS [Fisher Scientific BP166], 250 mM Tris HCl pH 6.8 [Fisher Scientific AAJ22676A1], 1 mg/ml bromophenol blue [Fisher Scientific AAA1846909], and 50% glycerol

[VWR MK509202]) and loaded into 4–20% mini-Protean TGX precast protein gels (Bio-Rad 4561096). Protein was transferred to nitrocellulose membranes (Bio-Rad 1620112) and blocked for 1 hour in 5% milk in Tris-buffered saline and 0.1% Tween-20 (Fisher Scientific BP337-500). The following primary antibodies were used: H3 (Abcam, 1791; 1:10,000 dilution); H3K36me3 (Abcam, 9050; 1:1,000); H3K36me2 (Cell Signaling, 2901S, 1:1,000). Goat anti-rabbit-HRP-conjugated (Invitrogen, PI31460; 1:2,000 dilution) was used as the secondary antibody. Proteins were detected using Immobilon western chemiluminescent HRP substrate (Fisher Scientific WBKLS0100).

2.4.7 Fluorescence Activated Cell Sorting

The strategy for isolating and sorting of specific intestinal epithelial cell type populations is outlined in Fig. S1b. Briefly, fluorescent reporter lines were used to sort Lgr5^{+} ISCs (Lgr5-$^{CreER\text{-}ires\text{-}EGFP}$), Paneth cells (Defa4^{Cre}:Rosa26^{tdTomato}), goblet cells (MUC2-mCherry), enteroendocrine cells (NeuroD1-Cre:Rosa26^{tdTomato}) and tuft cells (TRPM5-GFP). An enriched enterocyte cell population was sorted based on EpCAM+, CD44-, CD24- gating. The whole epithelial cell elution was used for all sorting experiments except for Lgr5+ ISC and Paneth cells, which involved gently scrapping the mucosal surface with a glass slide to remove villi prior to crypt elution. To generate a single-cell suspension, an eluted epithelial cell pellet was resuspended in digestion buffer (TrypLE [Fisher Scientific 12-605-010] containing 0.1mg/ml DNaseI [Sigma-Aldrich D4263]) for 5min, washed and then passed through 16G and 20G syringes, then 100 μm, 70 μm, and 40 μm filters. Cells were stained with 1.25 μL α-EpCAM-FITC (eBioscience 11-5791-82) per 1 million cells for 30 minutes on ice. 10 minutes before sorting, DAPI (VWR 950591; 1 μg/ml final) was added. Cells were sorted at the University of Colorado Cancer Center Flow Cytometry Shared Resource on a Sony MA900 with a 100 μm sorting chip or Beckman Coulter MoFlo XDP100 with a 100 μm nozzle tip.

2.4.8 Paneth Cell scRNA-seq Preparation and Analysis

The proximal small intestine (10 cm segment within a 2-12 cm region from the gastroduodenal junction) from an adult (female 20-week-old) Defa4^{Cre}:Rosa26$^{tdTomato/tdTomato}$

mouse was removed, rinsed with ice cold PBS, opened longitudinally, and then scraped with a glass slide to remove villi prior to crypt elution using chelation buffer (PBS containing 2 mM EDTA [Fisher Scientific S311] and 1 mM DTT [Fisher Scientific BP172-5]). To generate a single-cell suspension for flow cytometric analysis and sorting, isolated crypts were incubated with dispase (LifeTech 17105041; 0.3 U/ml), and DNaseI (LifeTech 17105041; 0.1 mg/ml,), cell suspensions were filtered through a 40-µm cell strainer and then stained with rat anti-EpCAM–fluorescein isothiocyanate IgG2a antibody (epithelial cell marker, 11-5791-82; eBioscience, San Diego, CA) and DAPI (VWR 95059; 1 µg/m, live/dead cell marker). Rat IgG2a–fluorescein isothiocyanate (eBioscience 11-4321-82) was used as a control. The Beckman Coulter MoFlo XDP100 cytometer (Beckman Coulter, Indianapolis, IN) with a 100-µm nozzle tip was used for single-cell sorting of EpCAM+ tdTomato^{-} and EpCAM+ tdTomato^{+} cell populations[123]. Sorted tdTomato+ Defa4^{Cre}-expressing Paneth cells were loaded onto Chromium Next GEM Single Cell 3' Library and Gel Bead Kit V2 (PN-120237, 10X Genomics) for complementary DNA library preparation. Sequencing was performed on an Illumina Novaseq6000 (Illumina).

2.4.9 Quantitative RT–PCR

For quantitative RT-PCR (qRT-PCR), cells from epithelial elutions of intestinal tissues or organoids were used. RNA was purified using a miRNeasy Micro kit (Qiagen 217084) according to the manufacturer's recommendation. cDNA was generated using a High-Capacity RNA-to-cDNA kit according to the manufacturer's recommendation (Applied Biosystems 4387406). Quantitative PCR was performed on a 7500 Fast Real-Time PCR System (Applied Biosystems) using Luna Universal qPCR Master Mix (New England Biolabs M3003), and cDNA from each sample in triplicate. The efficiencies of each primer set used was found to be >90%, and fold-change was calculated using the ΔΔCt method. The following primers were used:

Neurog3-F	ACCCTATCCACTGCTGCTTGTC
Neurog3-R	CGGGAAAAGGTTGTTGTGTCTCTG

GapDH-F	TATTATGGGGGTCTGGGATGG
GapDH-R	TCAAGAAGGTGGTGAAGCAGG
Lgr5-F	AGGCTGCCAAAAACTTCAGA
Lgr5-R	AGGGAAGGACGACAGGAGAT
Lyz1-F	GTGCCTGTCCTGATCTTTCT
Lyz1-R	GATTTGCTCCTGTGGTTATTGG
Muc2-F	AGAACGATGCCTACACCAAG
Muc2-R	CATTGAAGTCCCCGCAGAG
Sox9-F	CCTGGACTGTATGTGGATGTG
Sox9-R	TAAGGTCTGTCCGATGTCTCT
Atoh1-F	GGTCTGTGGTGATCGTTGTTA
Atoh1-R	TACAGAGGAAGGAGAAGGTAGG
Gfi1-F	GAGGAGGTGAAGCTGTGGAG
Gfi1-R	CTCCCTTGGAAGCACAGAAC
Hes5-F	ATGCTCAGTCCCAAGGAGAA
Hes5-R	GGCTTTGCTGTGTTTCAGGT
Hes1-F	AAGTCCCTAGCCCACCTCTC
Hes1-R	AGGCGCAATCCAATATGAAC
Ascl2-F	ATCTTCCATCTTCCGGACCT
Ascl2-R	TCTAGACAGTGGGGGTGAGG
Olfm4-F	ATGTGAGGCCTCCAAAAGTG
Olfm4-R	ACAGAAGGAGCGCTGATGTT
DCLK1-F	TCCACCGGAATTGAACTCGG
DCLK1-R	GGGAGCGAACAGTATCAGA
Alpi-F	CCAACTCTTTTGTGCCAGAGA
Alpi-R	GGCTACATTGGTGTTGAGCTTTT
Lact-F	CAGCGATGCCCACAGGAAAG
Lact-R	ACGGAGCCCTTGACGAGAG
Tff3-F	TTGCTGGGTCCTCTGGGATA
Tff3-R	GCCGGCACCATACATTGG
c-Myc-F	ACACGGAGGAAAACGACAAG

c-Myc-R	AGAGGTGAGCTTGTGCTCGT
Clu1-F	GATGATCCACCAGGCTCAACAG
Clu1-R	ACACAGTGCGGTCATCTTCACC

2.4.10 CUT&Tag

CUT&Tag was performed directly from cells isolated via epithelial elution, or organoids from culture. Nuclei were isolated and CUT&Tag was done following the protocol for "Benchtop CUT&Tag" or "CUT&Tag-direct" with slight modifications[95]. 50,000 nuclei per sample were used in all experiments. Antibodies used were H3K36me3 (Abcam AB9050), H3K36me2 (Active Motif 39255), and H3K27me3 (Cell Signaling C36B11). TapeStation analysis using High Sensitivity D1000 ScreenTape (Agilent 5067-5584) was used to confirm successful library preparation. Libraries were quantified using NEBNext Library Quant Kit for Illumina (NEB E7630) and pooled according to the concentration of each library. Libraries were then sent to Novogene for sequencing, or sequenced in house on a MiSeq, resulting in approximately 5 million reads per samples on average.

2.4.11 RNA-sequencing

For RNA-sequencing, cells from epithelial elutions of mouse intestine or organoids were used. RNA was purified from epithelial elutions using a miRNeasy Micro kit (Qiagen 217084) according to the manufacturer's recommendation. RNA was purified from organoids using Direct-zol RNA MiniPrep kit (Zymo R2050). Libraries were prepped using NEBNext Ultra II Directional RNA Library Prep Kit for Illumina (NEB E7490 and NEB E7760). Libraries were quantified using NEBNext Library Quant Kit for Illumina (NEB E7630) and pooled according to concentration of each library. Libraries were sent to Novogene for sequencing, resulting in approximately 20 million reads per sample on average.

2.4.12 Data Analysis

CUT&Tag sequencing reads were mapped to the mm10 reference genome, except for alignment of *Muc2* in Fig. S3f, which used mm39 for annotation purposes. Alignment was performed using in-house scripts based on deepTools, and the bamTools and bedTools suite. Heatmaps and metaplots were generated using deepTools. MACS2 was used with -q 0.05, --nolambda, and --broad to call peaks in each sample. For plots referencing bins, the genome was binned into 10,000 bp windows and the bedTools suite was used to calculate read density in these windows. Intergenic bins were defined as bins not containing annotated genes from the mm10 reference genome. DiffBind (v3.6.5) was used to call differential peaks between samples in R, and plots were generated using the 'ggplot2' package.

Analysis of RNA-sequencing was performed using nf-core/rnaseq pipeline (v3.8.1) with alignment to the mm10 genome, except for allignment of *Muc2* in Fig. S3f, which used mm39 for annotation purposes. DEseq2 (v1.26.0) was used to call differentially expressed genes, based on the criteria of >twofold change in expression value and FDR<0.05. Quantile normalization was used for WT H3 and H3K36M mouse samples to correct for abnormal count distribution and calculate size factors used for normalization in DEseq2. Enrichment of gene sets from previously published studies[96] was analyzed using fgsea with default parameters. Given the remarkable transcriptional similarity between Paneth and goblet cells, many genes classified to the goblet cell gene set[96] were expressed at high levels in Paneth cells and vice versa. To avoid confounding data, we therefore filtered out genes from the goblet cell gene set that had >500 counts (approx. top 90% of expressed genes) in Paneth cells and vice versa to make the gene sets more specific. For plots referencing bins, the genome was binned into 10,000 bp windows and the bedTools suite was used to map signal in these windows. Plots were generated in R using the 'ggplot2' package.

Analysis of raw scRNA-sequencing data was performed using CellRanger (v3.0.1) to align, filter, and count reads per cell. Seurat (v4.3.0) was used for downstream analysis. To remove low-quality cells and potential doublets, we filtered out cells with more than 5% reads mapping to mitochondrial genes and cells expressing less than 200 genes or more than 4000 genes. We used 50 Canonical Correlation Analysis (CCA) dimensions throughout the integration, 100 neighbors, 0.75 minimum distance, and a resolution of 0.3 for

unsupervised clustering. Representative genes for each cluster of cells were identified using FindConservedMarkers() function. To define mature and immature Paneth cell clusters, we used gene signatures defined previously[96]. Plots were generated in R using the 'ggplot2' package.

2.4.13 Statistics and Reproducibility

Statistical tests are described in the corresponding figure legends. Statistical analyses were carried out using R or JMP. Data distribution was presumed to be normal, though this was not formally tested. Sample size was not statistically pre-determined, and no data were excluded from analyses in this paper. The investigators were not blinded to experimental samples during outcome assessment unless otherwise indicated.

2.4.14 Data Availability

RNA-seq, CUT&Tag, and scRNA-seq data have been deposited in the Gene Expression Omnibus under accession code GSE247253. Any other data supporting the findings of this study are available from the corresponding authors upon request. Code for analyses of the data in this paper is available upon request.

CHAPTER 3

3 CONCLUSIONS AND FUTURE DIRECTIONS

3.1 Insights into regulation of cell homeostasis by H3K36 and H3K27 methylation

3.1.1 Conclusions

There are hundreds of different types of cells in the human body, yet they all contain the same DNA sequence. This suggests that further regulation exists to give each cell type unique ways to interpret the genome. Epigenetic regulation, and specifically histone modifications, are often considered important guides of cell fate change. However, how histone modifications functionally regulate cell fate to maintain homeostasis is incompletely understood. The small intestine is an excellent model to examine cell and tissue homeostasis, because it contains many different cell types with distinct transcriptional profiles. These specialized cells must be maintained in a certain balance to mediate organ function throughout an organism's life. Here, I show that H3K36 methylation is distinct between intestinal epithelial cell types. Differences in H3K36 methylation occur at genes related to specialized cell fate and correlate with gene expression. Further, disruption of H3K36 methylation leads to aberrant spreading of H3K27me3 over cell type-associated genes, that are correspondingly downregulated. Functionally, this leads to a defect in intestinal homeostasis characterized by a loss of mature Paneth and goblet cells, and an accumulation of an intermediate Paneth/goblet cell precursor. Together, these data suggest that H3K36 methylation plays a functional role in reinforcement of cell fate and tissue homeostasis.

3.1.2 Future Directions

In adult mice, intestinal epithelial cells turn over rapidly to maintain tissue function as cells die in the harsh environment. I noted severe defects in intestinal homeostasis following loss of H3K36 methylation in mature adult mice, suggesting that H3K36 methylation reinforces cell fate and is necessary to maintain homeostasis of the adult intestine. However, this raises the question of whether H3K36 methylation plays the same role during specification of the intestine during development, where mature cells and homeostasis have not yet been established. I noted that loss of H3K36 methylation leads to inappropriate spreading of H3K27 methylation over cell type-associated genes, mediating their silencing. At the same time, H3K27 methylation is titrated away from regenerative genes, leading to their activation. Together, these mechanisms increase plasticity and induce a fetal-like, regenerative state in the adult intestine. Therefore, it is tempting to speculate that H3K36 methylation would be necessary for intestinal epithelial cells to fully mature and tissue homeostasis to be established in the mouse intestine.

In this work, I used immunofluorescence and bulk gene expression to show that upon loss of H3K36 methylation in the adult intestine, mature cell types such as Paneth and goblet cells are lost, and immature goblet/Paneth intermediate cells accumulate. There are at least two possible explanations for these results. First, it could be that without H3K36 methylation, ISCs are unable to differentiate into mature goblet and Paneth cells, and instead remain as immature progenitors. Second, it is possible that titration of H3K27 methylation away from regenerative genes in H3K36M mice enables mature goblet and Paneth cells to dedifferentiate and accumulate as immature progenitors. One way to distinguish between these hypotheses would be single-cell RNA-sequencing (scRNA-seq) of the H3K36M intestine compared to WT H3. This experiment would clarify the transcriptional signature of the goblet/Paneth intermediate cells we noted and could potentially reveal any subtle shifts in these populations that bulk analysis overlooks. Further, pseudotime analysis of scRNA-seq data from different timepoints after H3K36M induction might clarify the dynamics of cell fate changes after loss of H3K36 methylation, namely whether goblet/Paneth intermediates preferentially dedifferentiate from one mature lineage or are a result of failed differentiation.

While this thesis mainly focuses on goblet and Paneth cells following loss of H3K36 methylation, I also noted subtle defects in enterocyte cells of H3K36M mice. Mature goblet

and Paneth cells secrete mucus and antimicrobial proteins or peptides to protect the surrounding tissue, while enterocytes are important for absorbing nutrients and maintaining an epithelial barrier. After H3K36M induction in mice and organoids, I noted a downregulation of enterocyte gene expression (Fig. 3.1a), as with mature goblet and Paneth cells, but immunofluorescence and histology did not reveal a gross phenotype of epithelial barrier dysfunction (Fig. 2.2c, Fig. S3a). To examine these results further, I performed transmission electron microscopy on sections of WT H3 or H3K36M intestines, but did not notice a gross defect in enterocyte cells or their brush border (Fig. 3.1b). I did note a ruffling of the nuclear membrane in H3K36M cells that suggests a potential function for H3K36 methylation in the nuclear lamina (Fig. 3.1b). There are known connections between chromatin and nuclear structure, so this may be a noteworthy future direction in the intestine as well as other tissues (see Appendix A). It is interesting that the decrease in mature enterocyte gene expression does not appear to disrupt the enterocyte barrier. Future experiments might examine this phenotype further, potentially by scRNA-seq as described above to determine whether sub-populations of immature enterocytes are affected upon loss of H3K36 methylation. The functional ability of these H3K36M enterocytes might also be tested by treating intestinal organoids or mice with bacteria or small molecules and assessing passage of these solutes across the epithelial barrier via different passage routes[134]. Experiments such as these might clarify whether the changes in gene expression that I observed are physiologically meaningful and reflect the importance of H3K36 methylation in mature enterocytes at homeostasis.

Figure 3.1

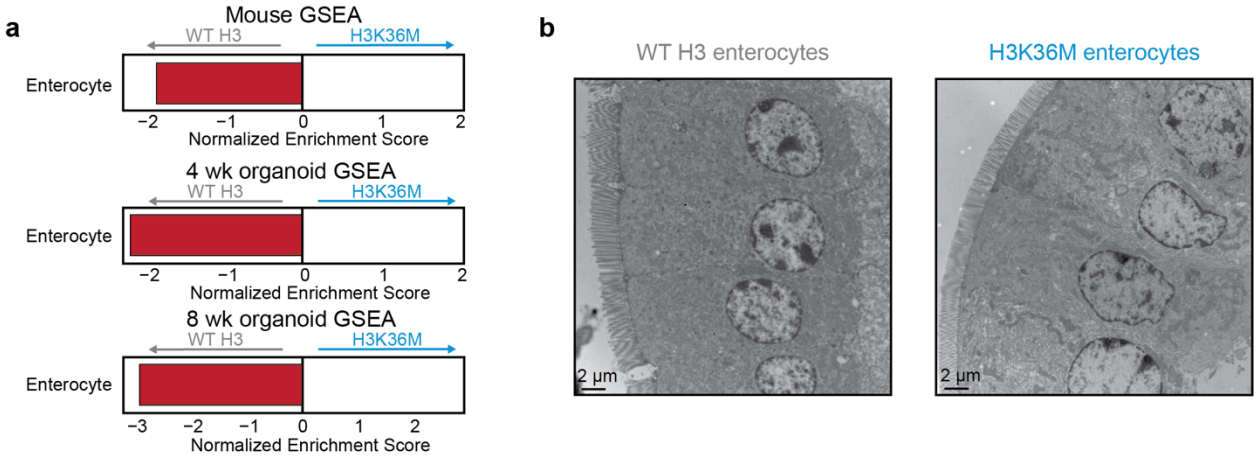

Figure 3.1 Suppressing H3K36 methylation disrupts enterocyte gene expression.

(a) Gene set enrichment analysis based on RNA-seq from WT H3 and H3K36M intestines after four weeks dox induction in mice (top), or four weeks dox induction in organoids (middle), or eight weeks dox induction in organoids (bottom) using an established enterocyte gene set.
(b) Representative transmission electron microscopy images of a WT H3 enterocyte (left, scale bar 2 μm), and H3K36M enterocyte found in the villus (right, scale bar 2 μm, n = 3 mice each).

Though here I establish the importance of H3K36 methylation in the intestine, and others have shown its relevance in stem cell models[105], chondrocytes[41], adipocytes[62], osteocytes[105], and blood[56], other epithelial tissues remain understudied. Preliminary work in our lab has revealed that disruption of H3K36 methylation in other gastrointestinal tissues such as the stomach or colon causes similar cell fate specification defects to the small intestine. It seems likely that H3K36 methylation might be involved in homeostasis of more diverse epithelial cell types as well, such as those in the respiratory tract or epidermis. Recently published work revealed that expression of H3K36M in self-renewing stratifying epithelia such as the skin, tongue, and esophagus during development led to defects in tissue function[135]. Namely, the reduction in H3K36 methylation led to aberrant gland formation due to loss of epithelial differentiation gene expression and gain of salivary gland gene expression, concomitant with changes in H3K27me3 distribution[135]. This supports the idea that H3K36 methylation has regulatory roles in many different tissues, and further work to characterize and perturb chromatin in these systems can illuminate how this histone modification directs cell fate.

Finally, though this thesis is focused on the interplay of H3K36 methylation and H3K27 methylation, there are other histone modifications that may also interact with these marks to regulate cell homeostasis. Recent work examined H3K27 acetylation (H3K27ac) upon H3K36M expression and found differential H3K27ac in regions losing H3K36me2, resulting in changes to enhancer activity[105]. Further, this work showed that DNA methylation at enhancers also changed upon H3K36M expression, specifically decreasing de novo methylation to activate genes[105]. As discussed above, previous work in the intestine established that these modifications do not differ significantly between intestinal cell types, namely enterocyte progenitors, secretory progenitors, and ISCs[67,85–91]. However, it is

possible that these modifications differ between fully mature intestinal cells or regulate cell fate during changes instead of cell fate at homeostasis. Future work might characterize these and other histone modifications in different contexts to provide a complete chromatin profile of the intestine.

3.2 Insights into regulation of plasticity by H3K36 and H3K27 methylation

3.2.1 Conclusions

Regeneration is an essential response to tissue damage as organisms age or are injured. In humans, tissues such as the skin, liver, bone marrow, and gastrointestinal tract can regenerate in response to damage. Regenerative tissues are particularly vulnerable to damage to the stem cell compartment, as without differentiation of these plastic cells, homeostasis cannot be maintained, and the tissue fails. To address this issue, the intestine has evolved to have specialized cells that are capable of dedifferentiation into plastic stem cells, followed by re-differentiation to replenish both the stem cell compartment and injured tissue. This begs the question of how specialized intestinal cells maintain the balance between specialized cell fate and plasticity. Given my findings that loss of H3K36 methylation disrupts specialized cell type-associated gene expression and tissue homeostasis, I hypothesized it might also lead to a more plastic state. Indeed, I found that suppressing H3K36 methylation leads to rapid induction of a fetal-like regenerative state in mice and intestinal organoids. Further, H3K36 methylation decreased globally following intestinal injury, concomitant with loss of specialized cell type gene expression, and H3K27me3 was correspondingly redistributed. Together, these data are the first to connect a histone modification to regeneration in the intestine.

3.2.2 Future Directions

Despite the work presented here, questions remain about the connection between histone modifications and tissue regeneration. Here I show that H3K36 and H3K27 methylation interact to regulate regeneration after intestinal injury, but is this connection also found in other epithelial tissues? Our preliminary examination of other

gastrointestinal tract tissues such as the colon and stomach would suggest that loss of H3K36 methylation does indeed impact tissue homeostasis, but further work is needed to examine how this connects to regeneration of these tissues. Additionally, tissues such as skin and liver may contain entirely different modes of regeneration, and the question remains whether H3K36 methylation may regulate those processes as well. Expression of H3K36M in combination with carcinogen treatment revealed that loss of H3K36 methylation leads to a less differentiated cell state that predisposes mice to squamous carcinogenesis[135]. This data suggests a similar link between H3K36 methylation and tissue plasticity in squamous epithelium as in the intestinal epithelium, and further work might strengthen this connection in other tissues.

My work shows that H3K36 methylation differentially marks genes in mature intestinal cell types, and that intestinal regeneration increases with loss of this histone modification. This raises the question of whether mature cells dedifferentiate after injury at different rates or with different efficiencies due to their differing levels of H3K36 methylation. One way to address this question is via lineage tracing studies. In a lineage tracing experiment, cells are marked at one timepoint, and the progeny of these marked cells are revealed at a later timepoint. For example, one might use Defa4-Cre; Rosa26-lsl-tdTomato mice, where Paneth cells turn on a red fluorescent reporter after a tamoxifen pulse. Following this pulse, all progeny of Paneth cells will also fluoresce red. Importantly, when intestinal cells dedifferentiate after injury, they can repopulate the entire crypt-villus structure. To take advantage of this, we could cross these Paneth cell Cre-linked reporter mice with H3K36M mice, injure the intestine via irradiation, and quantify the rate or extent of dedifferentiation of Paneth cells based on fluorescence. The same could be done with reporters for other mature cells of the intestine to determine which cell type, if any, makes up the bulk of dedifferentiation after injury. These experiments might also be successful in reporter organoids transfected with H3K36M for an approach that does not require mouse breeding.

Time course scRNA-seq experiments of H3K36M mice as described above may also elaborate on the nature of regeneration in this system – is regeneration induced in H3K36M mice due to mature cell loss, or due to dedifferentiation of mature cells? Examining gene expression changes over time at a single cell level could answer this question. Further, in the context of intestinal injury alone, I noted bulk loss of H3K36 methylation to support dedifferentiation. Single cell chromatin profiling experiments might

clarify whether specific cell types are responsible for this reduction, or whether all intestinal epithelial cells reduce methylation and dedifferentiate to replenish the intestinal epithelium.

There are strong connections between H3K36M expression and cancers such as chondroblastoma, giant cell bone tumors, soft-tissue sarcoma, and head and neck squamous cell carcinoma[41,53,54,59]. Indeed, plasticity and failure to differentiate are hallmarks of cancer. It is interesting to speculate whether long term, tissue specific expression of H3K36M in the intestine might lead to tumor formation and cancer, due to the excess plasticity noted in this thesis. Our preliminary data indicates that mice expressing H3K36M from an intestinal epithelial cell specific promoter showed intestinal defects but did not die or exhibit any gross health phenotypes after 8 weeks of induction. It would be interesting to examine any cancer-related phenotype changes that might appear at even further timepoints. It is also possible that another stimulus is needed in conjunction with H3K36M expression to induce tumor formation, as in the squamous epithelium[135]. To that end it is possible to cross H3K36M expressing mice with mice expressing a cancer driver in intestine or colon. I would predict a greater incidence of tumors or speed of cancer formation in these mice upon H3K36M induction due to the loss of mature cell types and increased regeneration. This would suggest a role for H3K36 methylation in preventing tumorigenesis at homeostasis. Finally, connecting these phenotypes to human diseases could pave the road for future treatments. For example, human tumor sequencing data could be examined for mutations in methyltransferases or demethylases of H3K36 and H3K27 that might lead to similar defects as those established here. Such future experiments would help cement the functional role of H3K36 methylation in reinforcing cell fate and regulating regeneration to prevent cancer upon injury.

4 BIBLIOGRAPHY

1. Luger, K., Mäder, A. W., Richmond, R. K., Sargent, D. F. & Richmond, T. J. Crystal structure of the nucleosome core particle at 2.8 A resolution. *Nature* **389**, 251–260 (1997).
2. Woodcock, C. L. & Dimitrov, S. Higher-order structure of chromatin and chromosomes. *Curr Opin Genet Dev* **11**, 130–135 (2001).
3. Klemm, S. L., Shipony, Z. & Greenleaf, W. J. Chromatin accessibility and the regulatory epigenome. *Nature Reviews Genetics 2018 20:4* **20**, 207–220 (2019).
4. Bonev, B. & Cavalli, G. Organization and function of the 3D genome. *Nature Reviews Genetics 2016 17:11* **17**, 661–678 (2016).
5. Martire, S. & Banaszynski, L. A. The roles of histone variants in fine-tuning chromatin organization and function. *Nature Reviews Molecular Cell Biology 2020 21:9* **21**, 522–541 (2020).
6. Panne, D. *et al.* Mechanistic insights into histone deposition and nucleosome assembly by the chromatin assembly factor-1. *Nucleic Acids Res* **46**, 9907–9917 (2018).
7. Ahmad, K. & Henikoff, S. Histone H3 variants specify modes of chromatin assembly. *Proc Natl Acad Sci U S A* **99**, 16477–16484 (2002).
8. Goldberg, A. D. *et al.* Distinct Factors Control Histone Variant H3.3 Localization at Specific Genomic Regions. *Cell* **140**, 678–691 (2010).
9. Tagami, H., Ray-Gallet, D., Almouzni, G. & Nakatani, Y. Histone H3.1 and H3.3 Complexes Mediate Nucleosome Assembly Pathways Dependent or Independent of DNA Synthesis. *Cell* **116**, 51–61 (2004).
10. Xiong, C. *et al.* UBN1/2 of HIRA complex is responsible for recognition and deposition of H3.3 at cis-regulatory elements of genes in mouse ES cells. *BMC Biol* **16**, 1–18 (2018).
11. Ray-Gallet, D. *et al.* Dynamics of Histone H3 Deposition In Vivo Reveal a Nucleosome Gap-Filling Mechanism for H3.3 to Maintain Chromatin Integrity. *Mol Cell* **44**, 928–941 (2011).
12. Phanstiel, D. *et al.* Mass spectrometry identifies and quantifies 74 unique histone H4 isoforms in differentiating human embryonic stem cells. *Proc Natl Acad Sci U S A* **105**, 4093–4098 (2008).

13. Turner, B. M. Decoding the nucleosome. *Cell* **75**, 5–8 (1993).
14. Millán-Zambrano, G., Burton, A., Bannister, A. J. & Schneider, R. Histone post-translational modifications — cause and consequence of genome function. *Nature Reviews Genetics 2022 23:9* **23**, 563–580 (2022).
15. Greer, E. L. & Shi, Y. Histone methylation: a dynamic mark in health, disease and inheritance. *Nature Reviews Genetics 2012 13:5* **13**, 343–357 (2012).
16. Zhou, V. W., Goren, A. & Bernstein, B. E. Charting histone modifications and the functional organization of mammalian genomes. *Nat Rev Genet* **12**, 7–18 (2011).
17. Brumbaugh, J., Rose, C. M., Phanstiel, D. H., Thomson, J. A. & Coon, J. J. Proteomics and pluripotency. *Crit Rev Biochem Mol Biol* **46**, 493–506 (2011).
18. Apostolou, E. & Hochedlinger, K. Chromatin dynamics during cellular reprogramming. *Nature* **502**, 462–471 (2013).
19. Perino, M. & Veenstra, G. J. C. Chromatin Control of Developmental Dynamics and Plasticity. *Dev Cell* **38**, 610–620 (2016).
20. Shvedunova, M. & Akhtar, A. Modulation of cellular processes by histone and non-histone protein acetylation. *Nature Reviews Molecular Cell Biology 2022 23:5* **23**, 329–349 (2022).
21. Zhang, W., Bone, J. R., Edmondson, D. G., Turner, B. M. & Roth, S. Y. Essential and redundant functions of histone acetylation revealed by mutation of target lysines and loss of the Gcn5p acetyltransferase. *EMBO J* **17**, 3155–3167 (1998).
22. Narita, T. *et al.* Enhancers are activated by p300/CBP activity-dependent PIC assembly, RNAPII recruitment, and pause release. *Mol Cell* **81**, 2166-2182.e6 (2021).
23. Gehani, S. S. *et al.* Polycomb Group Protein Displacement and Gene Activation through MSK-Dependent H3K27me3S28 Phosphorylation. *Mol Cell* **39**, 886–900 (2010).
24. Bernstein, B. E. *et al.* A Bivalent Chromatin Structure Marks Key Developmental Genes in Embryonic Stem Cells. *Cell* **125**, 315–326 (2006).
25. Beacon, T. H. *et al.* The dynamic broad epigenetic (H3K4me3, H3K27ac) domain as a mark of essential genes. *Clinical Epigenetics 2021 13:1* **13**, 1–17 (2021).
26. Wagner, E. J. & Carpenter, P. B. Understanding the language of Lys36 methylation at histone H3. *Nature Reviews Molecular Cell Biology 2012 13:2* **13**, 115–126 (2012).

27. Edmunds, J. W., Mahadevan, L. C. & Clayton, A. L. Dynamic histone H3 methylation during gene induction: HYPB/Setd2 mediates all H3K36 trimethylation. *EMBO J* **27**, 406–420 (2008).
28. Dillon, S. C., Zhang, X., Trievel, R. C. & Cheng, X. The SET-domain protein superfamily: protein lysine methyltransferases. *Genome Biol* **6**, 227 (2005).
29. Tsukada, Y. I. *et al.* Histone demethylation by a family of JmjC domain-containing proteins. *Nature* **439**, 811–816 (2006).
30. Klose, R. J. *et al.* The transcriptional repressor JHDM3A demethylates trimethyl histone H3 lysine 9 and lysine 36. *Nature* **442**, 312–316 (2006).
31. Cloos, P. A. C. *et al.* The putative oncogene GASC1 demethylates tri- and dimethylated lysine 9 on histone H3. *Nature* **442**, 307–311 (2006).
32. Wen, H. *et al.* ZMYND11 links histone H3.3K36me3 to transcription elongation and tumour suppression. *Nature* **508**, 263–268 (2014).
33. McDaniel, S. L. & Strahl, B. D. Shaping the cellular landscape with Set2/SETD2 methylation. *Cell Mol Life Sci* **74**, 3317–3334 (2017).
34. Cheung, V. *et al.* Chromatin- and Transcription-Related Factors Repress Transcription from within Coding Regions throughout the Saccharomyces cerevisiae Genome. *PLoS Biol* **6**, e277 (2008).
35. Hyun, K., Jeon, J., Park, K. & Kim, J. Writing, erasing and reading histone lysine methylations. *Exp Mol Med* **49**, (2017).
36. Chaouch, A. *et al.* Histone H3.3 K27M and K36M mutations de-repress transposable elements through perturbation of antagonistic chromatin marks. *Mol Cell* **81**, 4876-4890.e7 (2021).
37. Popovic, R. *et al.* Histone Methyltransferase MMSET/NSD2 Alters EZH2 Binding and Reprograms the Myeloma Epigenome through Global and Focal Changes in H3K36 and H3K27 Methylation. *PLoS Genet* **10**, e1004566 (2014).
38. Streubel, G. *et al.* The H3K36me2 Methyltransferase Nsd1 Demarcates PRC2-Mediated H3K27me2 and H3K27me3 Domains in Embryonic Stem Cells. *Mol Cell* **70**, 371-379.e5 (2018).
39. Alabert, C. *et al.* Domain Model Explains Propagation Dynamics and Stability of Histone H3K27 and H3K36 Methylation Landscapes. *Cell Rep* **30**, 1223-1234.e8 (2020).

40. Harutyunyan, A. S. *et al.* H3K27M in Gliomas Causes a One-Step Decrease in H3K27 Methylation and Reduced Spreading within the Constraints of H3K36 Methylation. *Cell Rep* **33**, 108390 (2020).
41. Lu, C. *et al.* Cancer: Histone H3K36 mutations promote sarcomagenesis through altered histone methylation landscape. *Science (1979)* **352**, 844–849 (2016).
42. Jani, K. S. *et al.* Histone H3 tail binds a unique sensing pocket in EZH2 to activate the PRC2 methyltransferase. *Proc Natl Acad Sci U S A* **116**, 8295–8300 (2019).
43. Finogenova, K. *et al.* Structural basis for prc2 decoding of active histone methylation marks h3k36me2/3. *Elife* **9**, 1–30 (2020).
44. Yuan, W. *et al.* H3K36 Methylation Antagonizes PRC2-mediated H3K27 Methylation. *Journal of Biological Chemistry* **286**, 7983–7989 (2011).
45. Schmitges, F. W. *et al.* Histone Methylation by PRC2 Is Inhibited by Active Chromatin Marks. *Mol Cell* **42**, 330–341 (2011).
46. Zheng, Y. *et al.* Total kinetic analysis reveals how combinatorial methylation patterns are established on lysines 27 and 36 of histone H3. *Proc Natl Acad Sci U S A* **109**, 13549–13554 (2012).
47. Voigt, P. *et al.* Asymmetrically Modified Nucleosomes. *Cell* **151**, 181–193 (2012).
48. Sankar, A. *et al.* Histone editing elucidates the functional roles of H3K27 methylation and acetylation in mammals. *Nat Genet* **54**, 754–760 (2022).
49. Inagawa, M. *et al.* Histone H3 lysine 9 methyltransferases, G9a and GLP are essential for cardiac morphogenesis. *Mech Dev* **130**, 519–531 (2013).
50. Miller, S. A., Mohn, S. E. & Weinmann, A. S. Jmjd3 and UTX play a demethylase-independent role in chromatin remodeling to regulate T-box family member-dependent gene expression. *Mol Cell* **40**, 594–605 (2010).
51. Xu, K. *et al.* EZH2 oncogenic activity in castration-resistant prostate cancer cells is Polycomb-independent. *Science* **338**, 1465–1469 (2012).
52. Warrier, T. *et al.* SETDB1 acts as a topological accessory to Cohesin via an H3K9me3-independent, genomic shunt for regulating cell fates. *Nucleic Acids Res* **50**, 7326–7349 (2022).
53. Behjati, S. *et al.* Distinct H3F3A and H3F3B driver variants define chondroblastoma and giant cell tumour of bone. *Nat Genet* **45**, 1479–1482 (2013).
54. Papillon-Cavanagh, S. *et al.* Impaired H3K36 methylation defines a subset of head and neck squamous cell carcinomas. *Nat Genet* **49**, 180–185 (2017).

55. Lewis, P. W. *et al.* Inhibition of PRC2 activity by a gain-of-function H3 mutation found in pediatric glioblastoma. *Science (1979)* **340**, 857–861 (2013).
56. Brumbaugh, J., Schwarz, B. A., Huebner, A. J. & Coffey, A. Inducible histone K-to-M mutations are dynamic tools to probe the physiological role of site- specific histone methylation in vitro and in vivo. *Nat Cell Biol* **21**, 1449–1461 (2019).
57. Zhang, Y. *et al.* Molecular basis for the role of oncogenic histone mutations in modulating H3K36 methylation. *Sci Rep* **7**, (2017).
58. Yang, S. *et al.* Molecular basis for oncohistone H3 recognition by SETD2 methyltransferase. *Genes Dev* **30**, 1611–1616 (2016).
59. Fang, D. *et al.* The histone H3.3K36M mutation reprograms the epigenome of chondroblastomas. *Science (1979)* **352**, 1344–1348 (2016).
60. Yuan, S. *et al.* Global regulation of the histone mark H3K36me2 underlies epithelial plasticity and metastatic progression. *Cancer Discov* **10**, 854–871 (2020).
61. Yano, S. *et al.* Histone H3K36me2 and H3K36me3 form a chromatin platform essential for DNMT3A-dependent DNA methylation in mouse oocytes. *Nat Commun* **13**, (2022).
62. Zhuang, L. *et al.* Depletion of Nsd2-mediated histone H3K36 methylation impairs adipose tissue development and function. *Nat Commun* **9**, (2018).
63. Snoeck, V., Goddeeris, B. & Cox, E. The role of enterocytes in the intestinal barrier function and antigen uptake. *Microbes and Infection* vol. 7 997–1004 Preprint at https://doi.org/10.1016/j.micinf.2005.04.003 (2005).
64. Saxena, M. & Shivdasani, R. A. Epigenetic Signatures and Plasticity of Intestinal and Other Stem Cells. *Annu. Rev. Physiol.* **83**, 405–427 (2021).
65. Flier, L. G. van der & Clevers, H. Stem Cells, Self-Renewal, and Differentiation in the Intestinal Epithelium. *Annu. Rev. Physiol.* **71**, 241–260 (2009).
66. Peterson, L. W. & Artis, D. Intestinal epithelial cells: regulators of barrier function and immune homeostasis. *Nature Reviews Immunology 2014 14:3* **14**, 141–153 (2014).
67. Kim, T.-H. *et al.* Broadly permissive intestinal chromatin underlies lateral inhibition and cell plasticity. *Nature* **506**, 511–515 (2014).
68. Stamataki, D. *et al.* Delta1 Expression, Cell Cycle Exit, and Commitment to a Specific Secretory Fate Coincide within a Few Hours in the Mouse Intestinal Stem Cell System. *PLoS One* **6**, e24484 (2011).

69. Kim, T.-H. & Shivdasani, R. A. Genetic evidence that intestinal Notch functions vary regionally and operate through a common mechanism of Math1 repression. *J Biol Chem* **286**, 11427–11433 (2011).
70. Pellegrinet, L. *et al.* Dll1- and Dll4-Mediated Notch Signaling Are Required for Homeostasis of Intestinal Stem Cells. *Gastroenterology* **140**, 1230-1240.e7 (2011).
71. VanDussen, K. L. & Samuelson, L. C. Mouse atonal homolog 1 directs intestinal progenitors to secretory cell rather than absorptive cell fate. *Dev Biol* **346**, 215–223 (2010).
72. Tsai, Y. H. *et al.* ADAM10 Regulates Notch Function in Intestinal Stem Cells of Mice. *Gastroenterology* **147**, 822-834.e13 (2014).
73. Jadhav, U. *et al.* Dynamic Reorganization of Chromatin Accessibility Signatures during Dedifferentiation of Secretory Precursors into Lgr5+ Intestinal Stem Cells. *Cell Stem Cell* **21**, 65-77.e5 (2017).
74. van Es, J. H. *et al.* Dll1+ secretory progenitor cells revert to stem cells upon crypt damage. *Nat Cell Biol* **14**, 1099–1104 (2012).
75. Jones, J. C. *et al.* Cellular Plasticity of Defa4Cre-Expressing Paneth Cells in Response to Notch Activation and Intestinal Injury. *Cell Mol Gastroenterol Hepatol* **7**, 533–554 (2019).
76. Yu, S. *et al.* Paneth Cell Multipotency Induced by Notch Activation following Injury. *Cell Stem Cell* **23**, 46-59.e5 (2018).
77. Buczacki, S. J. A. *et al.* Intestinal label-retaining cells are secretory precursors expressing Lgr5. *Nature* **495**, 65–9 (2013).
78. Sangiorgi, E. & Capecchi, M. R. Bmi1 is expressed in vivo in intestinal stem cells. *Nat Genet* **40**, 915–920 (2008).
79. Tian, H. *et al.* A reserve stem cell population in small intestine renders Lgr5-positive cells dispensable. *Nature* **478**, 255–259 (2011).
80. Tetteh, P. W. *et al.* Replacement of Lost Lgr5-Positive Stem Cells through Plasticity of Their Enterocyte-Lineage Daughters. *Cell Stem Cell* **18**, 203–13 (2016).
81. Yan, K. S. *et al.* Intestinal Enteroendocrine Lineage Cells Possess Homeostatic and Injury-Inducible Stem Cell Activity. *Cell Stem Cell* **21**, 78-90.e6 (2017).
82. Nusse, Y. M. *et al.* Parasitic helminths induce fetal-like reversion in the intestinal stem cell niche. *Nature* **559**, 109–113 (2018).

83. Sato, T. *et al.* Single Lgr5 stem cells build crypt-villus structures in vitro without a mesenchymal niche. *Nature 2009 459:7244* **459**, 262–265 (2009).
84. Mahe, M. M. *et al.* Establishment of Gastrointestinal Epithelial Organoids. *Curr Protoc Mouse Biol* **3**, 217–240 (2013).
85. Jadhav, U. *et al.* Dynamic Reorganization of Chromatin Accessibility Signatures during Dedifferentiation of Secretory Precursors into Lgr5+ Intestinal Stem Cells. *Cell Stem Cell* **21**, 65–77 (2017).
86. Jadhav, U. *et al.* Extensive Recovery of Embryonic Enhancer and Gene Memory Stored in Hypomethylated Enhancer DNA. *Mol Cell* **74**, 542-554.e5 (2019).
87. Raab, J. R. *et al.* Quantitative classification of chromatin dynamics reveals regulators of intestinal stem cell differentiation. *Development* **147**, (2020).
88. Kazakevych, J., Sayols, S., Messner, B., Krienke, C. & Soshnikova, N. Dynamic changes in chromatin states during specification and differentiation of adult intestinal stem cells. *Nucleic Acids Res* **45**, 5770–5784 (2017).
89. Sheaffer, K. L. *et al.* DNA methylation is required for the control of stem cell differentiation in the small intestine. *Genes Dev* **28**, 652–664 (2014).
90. Verzi, M. P. & Shivdasani, R. A. Epigenetic regulation of intestinal stem cell differentiation. *Am J Physiol Gastrointest Liver Physiol* **319**, G189–G196 (2020).
91. Kaaij, L. T. J. *et al.* DNA methylation dynamics during intestinal stem cell differentiation reveals enhancers driving gene expression in the villus. *Genome Biol* **14**, 1–15 (2013).
92. Jadhav, U. *et al.* Acquired Tissue-Specific Promoter Bivalency Is a Basis for PRC2 Necessity in Adult Cells. *Cell* **165**, 1389–1400 (2016).
93. Kolev, H. M. *et al.* H3K27me3 Demethylases Maintain the Transcriptional and Epigenomic Landscape of the Intestinal Epithelium. *Cell Mol Gastroenterol Hepatol* **15**, 821–839 (2023).
94. Saxena, M. & Shivdasani, R. A. Epigenetic Signatures and Plasticity of Intestinal and Other Stem Cells. *Annu Rev Physiol* **83**, 405–427 (2021).
95. Kaya-Okur, H. S. *et al.* CUT&Tag for efficient epigenomic profiling of small samples and single cells. *Nature Communications 2019 10:1* **10**, 1–10 (2019).
96. Haber, A. L. *et al.* A single-cell survey of the small intestinal epithelium. *Nature* **551**, 333–339 (2017).

97. Beard, C., Hochedlinger, K., Plath, K., Wutz, A. & Jaenisch, R. Efficient method to generate single-copy transgenic mice by site-specific integration in embryonic stem cells. *Genesis* **44**, 23–28 (2006).
98. Shroyer, N. F., Wallis, D., Venken, K. J. T., Bellen, H. J. & Zoghbi, H. Y. Gfi1 functions downstream of Math1 to control intestinal secretory cell subtype allocation and differentiation. *Genes Dev* **19**, 2412–2417 (2005).
99. Shah, R. N. *et al.* Examining the Roles of H3K4 Methylation States with Systematically Characterized Antibodies. *Mol Cell* **72**, 162-177.e7 (2018).
100. Abe, S., Nagatomo, H., Sasaki, H. & Ishiuchi, T. A histone H3.3K36M mutation in mice causes an imbalance of histone modifications and defects in chondrocyte differentiation. *Epigenetics* **16**, 1123–1134 (2021).
101. Sengupta, D. *et al.* NSD2 dimethylation at H3K36 promotes lung adenocarcinoma pathogenesis. *Mol Cell* **81**, 4481-4492.e9 (2021).
102. Garabedian, E. M., Roberts, L. J., McNevin, M. S. & Gordon, J. I. Examining the Role of Paneth Cells in the Small Intestine by Lineage Ablation in Transgenic Mice. *J Biol Chem* **272**, 23729–23740 (1997).
103. Grinat, J. *et al.* Epigenetic modifier balances Mapk and Wnt signalling in differentiation of goblet and Paneth cells. *Life Sci Alliance* **5**, (2022).
104. Ansari, I. *et al.* TET2 and TET3 loss disrupts small intestine differentiation and homeostasis. *Nature Communications 2023 14:1* **14**, 1–18 (2023).
105. Hoetker, M. S. *et al.* H3K36 methylation maintains cell identity by regulating opposing lineage programmes. *Nature Cell Biology 2023 25:8* **25**, 1121–1134 (2023).
106. Yui, S. *et al.* YAP/TAZ-Dependent Reprogramming of Colonic Epithelium Links ECM Remodeling to Tissue Regeneration. *Cell Stem Cell* **22**, 35–49.e7 (2018).
107. Gregorieff, A., Liu, Y., Inanlou, M. R., Khomchuk, Y. & Wrana, J. L. Yap-dependent reprogramming of Lgr5+ stem cells drives intestinal regeneration and cancer. *Nature* **526**, 715–718 (2015).
108. Ayyaz, A. *et al.* Single-cell transcriptomes of the regenerating intestine reveal a revival stem cell. *Nature* **569**, 121–125 (2019).
109. Mustata, R. C. *et al.* Identification of Lgr5-Independent Spheroid-Generating Progenitors of the Mouse Fetal Intestinal Epithelium. *Cell Rep* **5**, 421–432 (2013).
110. Fordham, R. P. *et al.* Transplantation of Expanded Fetal Intestinal Progenitors Contributes to Colon Regeneration after Injury. *Cell Stem Cell* **13**, 734 (2013).

111. Muñoz, J. *et al.* The Lgr5 intestinal stem cell signature: robust expression of proposed quiescent '+4' cell markers. *EMBO J* **31**, 3079–3091 (2012).
112. Montenegro-Miranda, P. S. *et al.* A Novel Organoid Model of Damage and Repair Identifies HNF4α as a Critical Regulator of Intestinal Epithelial Regeneration. *Cell Mol Gastroenterol Hepatol* **10**, 209–223 (2020).
113. van der Flier, L. G. & Clevers, H. Stem Cells, Self-Renewal, and Differentiation in the Intestinal Epithelium. *Annu Rev Physiol* **71**, 241–260 (2009).
114. Yang, Q., Bermingham, N. A., Finegold, M. J. & Zoghbi, H. Y. Requirement of Math1 for secretory cell lineage commitment in the mouse intestine. *Science* **294**, 2155–2158 (2001).
115. Rodrigues, C. P., Shvedunova, M. & Akhtar, A. Epigenetic Regulators as the Gatekeepers of Hematopoiesis. *Trends in Genetics* **37**, 125–142 (2021).
116. Yu, V. W. C. *et al.* Epigenetic Memory Underlies Cell-Autonomous Heterogeneous Behavior of Hematopoietic Stem Cells. *Cell* **168**, 944–945 (2017).
117. Cui, K. *et al.* Chromatin signatures in multipotent human hematopoietic stem cells indicate the fate of bivalent genes during differentiation. *Cell Stem Cell* **4**, 80 (2009).
118. Weishaupt, H., Sigvardsson, M. & Attema, J. L. Epigenetic chromatin states uniquely define the developmental plasticity of murine hematopoietic stem cells. *Blood* **115**, 247–256 (2010).
119. Koppens, M. A. J. *et al.* Deletion of Polycomb Repressive Complex 2 From Mouse Intestine Causes Loss of Stem Cells. *Gastroenterology* **151**, 684-697.e12 (2016).
120. Chiacchiera, F., Rossi, A., Jammula, S., Zanotti, M. & Pasini, D. PRC2 preserves intestinal progenitors and restricts secretory lineage commitment. *EMBO J* **35**, 2301–2314 (2016).
121. Willet, S. G. *et al.* Regenerative proliferation of differentiated cells by mTORC1-dependent paligenosis. *EMBO J* **37**, e98311 (2018).
122. Burger, E. *et al.* Loss of Paneth Cell Autophagy Causes Acute Susceptibility to Toxoplasma gondii-Mediated Inflammation. *Cell Host Microbe* **23**, 177-190.e4 (2018).
123. Jones, J. C. *et al.* Cellular Plasticity of Defa4 Cre-Expressing Paneth Cells in Response to Notch Activation and Intestinal Injury. *Cellular and Molecular Gastroenterology and Hepatology Cellular and Molecular Gastroenterology and Hepatology https://www.cmghjournal.org* **7**, 533–554 (2019).

124. Barker, N. *et al.* Identification of stem cells in small intestine and colon by marker gene Lgr5. *Nature 2007 449:7165* **449**, 1003–1007 (2007).
125. Madisen, L. *et al.* A robust and high-throughput Cre reporting and characterization system for the whole mouse brain. *Nature Neuroscience 2009 13:1* **13**, 133–140 (2009).
126. Li, H. J., Kapoor, A., Giel-Moloney, M., Rindi, G. & Leiter, A. B. Notch signaling differentially regulates the cell fate of early endocrine precursor cells and their maturing descendants in the mouse pancreas and intestine. *Dev Biol* **371**, 156–169 (2012).
127. Birchenough, G. M. H., Nystrom, E. E. L., Johansson, M. E. V. & Hansson, G. C. A sentinel goblet cell guards the colonic crypt by triggering Nlrp6-dependent Muc2 secretion. *Science* **352**, 1535–1542 (2016).
128. Clapp, T. R., Medler, K. F., Damak, S., Margolskee, R. F. & Kinnamon, S. C. Mouse taste cells with G protein-coupled taste receptors lack voltage-gated calcium channels and SNAP-25. *BMC Biol* **4**, (2006).
129. Bell, S. M. *et al.* R-spondin 2 is required for normal laryngeal-tracheal, lung and limb morphogenesis. *Development* **135**, 1049–1058 (2008).
130. De Van Lidth Jeude, J. F., Vermeulen, J. L. M., Montenegro-Miranda, P. S., Van Den Brink, G. R. & Heijmans, J. A Protocol for Lentiviral Transduction and Downstream Analysis of Intestinal Organoids. *J Vis Exp* **2015**, 52531 (2015).
131. Miyoshi, H. & Stappenbeck, T. S. In vitro expansion and genetic modification of gastrointestinal stem cells in spheroid culture. *Nat Protoc* **8**, 2471–2482 (2013).
132. Koo, B. K., Sasselli, V. & Clevers, H. Retroviral gene expression control in primary organoid cultures. *Curr Protoc Stem Cell Biol* **27**, (2013).
133. Dekkers, J. F. *et al.* High-resolution 3D imaging of fixed and cleared organoids. *Nat Protoc* **14**, 1756–1771 (2019).
134. Schoultz, I. & Keita, Å. V. The Intestinal Barrier and Current Techniques for the Assessment of Gut Permeability. *Cells* **9**, (2020).
135. Ko, E. K. *et al.* Disruption of H3K36 methylation provokes cellular plasticity to drive aberrant glandular formation and squamous carcinogenesis. *Dev Cell* **59**, 187-198.e7 (2024).
136. Nicetto, D. & Zaret, K. S. Role of H3K9me3 heterochromatin in cell identity establishment and maintenance. *Curr Opin Genet Dev* **55**, 1–10 (2019).

137. Schotta, G. *et al.* Central role of Drosophila SU(VAR)3-9 in histone H3-K9 methylation and heterochromatic gene silencing. *EMBO J* **21**, 1121–1131 (2002).
138. Gupta, J., Kumar, S., Li, J., Krishna Murthy Karuturi, R. & Tikoo, K. Histone H3 lysine 4 monomethylation (H3K4me1) and H3 lysine 9 monomethylation (H3K9me1): distribution and their association in regulating gene expression under hyperglycaemic/hyperinsulinemic conditions in 3T3 cells. *Biochimie* **94**, 2656–2664 (2012).
139. Barski, A. *et al.* High-resolution profiling of histone methylations in the human genome. *Cell* **129**, 823–837 (2007).
140. Poleshko, A. *et al.* H3K9me2 orchestrates inheritance of spatial positioning of peripheral heterochromatin through mitosis. *Elife* **8**, (2019).
141. Fukuda, K. *et al.* Regulation of mammalian 3D genome organization and histone H3K9 dimethylation by H3K9 methyltransferases. *Commun Biol* **4**, (2021).
142. Mikkelsen, T. S. *et al.* Genome-wide maps of chromatin state in pluripotent and lineage-committed cells. *Nature* **448**, 553–560 (2007).
143. Bulut-Karslioglu, A. *et al.* Suv39h-dependent H3K9me3 marks intact retrotransposons and silences LINE elements in mouse embryonic stem cells. *Mol Cell* **55**, 277–290 (2014).
144. Leung, D. C. & Lorincz, M. C. Silencing of endogenous retroviruses: when and why do histone marks predominate? *Trends Biochem Sci* **37**, 127–133 (2012).
145. Padeken, J., Methot, S. P. & Gasser, S. M. Establishment of H3K9-methylated heterochromatin and its functions in tissue differentiation and maintenance. *Nat Rev Mol Cell Biol* **23**, 623–640 (2022).
146. Ninova, M., Tóth, K. F. & Aravin, A. A. The control of gene expression and cell identity by H3K9 trimethylation. *Development* **146**, (2019).
147. Jayaram, H. *et al.* S-adenosyl methionine is necessary for inhibition of the methyltransferase G9a by the lysine 9 to methionine mutation on histone H3. *Proc Natl Acad Sci U S A* **113**, 6282–6287 (2016).
148. Shan, C. M. *et al.* A histone H3K9M mutation traps histone methyltransferase Clr4 to prevent heterochromatin spreading. *Elife* **5**, (2016).
149. Parada, L. A., McQueen, P. G. & Misteli, T. Tissue-specific spatial organization of genomes. *Genome Biol* **5**, (2004).

150. Joffe, B., Leonhardt, H. & Solovei, I. Differentiation and large scale spatial organization of the genome. *Curr Opin Genet Dev* **20**, 562–569 (2010).
151. de las Heras, J. I. *et al.* Tissue specificity in the nuclear envelope supports its functional complexity. *Nucleus* **4**, 460–477 (2013).
152. Solovei, I. *et al.* LBR and lamin A/C sequentially tether peripheral heterochromatin and inversely regulate differentiation. *Cell* **152**, 584–598 (2013).
153. Hug, C. B. & Vaquerizas, J. M. The Birth of the 3D Genome during Early Embryonic Development. *Trends Genet* **34**, 903–914 (2018).
154. Guilluy, C. *et al.* Isolated nuclei adapt to force and reveal a mechanotransduction pathway in the nucleus. *Nat Cell Biol* **16**, 376–381 (2014).
155. Zhang, Q. *et al.* Nesprin-2 is a multi-isomeric protein that binds lamin and emerin at the nuclear envelope and forms a subcellular network in skeletal muscle. *J Cell Sci* **118**, 673–687 (2005).
156. Zhang, Q., Ragnauth, C., Greener, M. J., Shanahan, C. M. & Roberts, R. G. The Nesprins Are Giant Actin-Binding Proteins, Orthologous to Drosophila melanogaster Muscle Protein MSP-300. *Genomics* **80**, 473–481 (2002).
157. Apel, E. D., Lewis, R. M., Grady, R. M. & Sanes, J. R. Syne-1, a dystrophin- and Klarsicht-related protein associated with synaptic nuclei at the neuromuscular junction. *J Biol Chem* **275**, 31986–31995 (2000).
158. Crisp, M. *et al.* Coupling of the nucleus and cytoplasm: role of the LINC complex. *J Cell Biol* **172**, 41–53 (2006).
159. Spagnol, S. T., Armiger, T. J. & Dahl, K. N. Mechanobiology of Chromatin and the Nuclear Interior. *Cell Mol Bioeng* **9**, 268–276 (2016).
160. Uzer, G. *et al.* Cell Mechanosensitivity to Extremely Low-Magnitude Signals Is Enabled by a LINCed Nucleus. *Stem Cells* **33**, 2063–2076 (2015).
161. Heo, S. J. *et al.* Differentiation alters stem cell nuclear architecture, mechanics, and mechano-sensitivity. *Elife* **5**, (2016).
162. Fedorchak, G. R., Kaminski, A. & Lammerding, J. Cellular mechanosensing: Getting to the nucleus of it all. *Prog Biophys Mol Biol* **115**, 76–92 (2014).
163. Swift, J. *et al.* Nuclear lamin-A scales with tissue stiffness and enhances matrix-directed differentiation. *Science* **341**, (2013).

164. Seelbinder, B. *et al.* Nuclear deformation guides chromatin reorganization in cardiac development and disease. *Nature Biomedical Engineering 2021 5:12* **5**, 1500–1516 (2021).
165. Ghosh, S. *et al.* Dedifferentiation alters chondrocyte nuclear mechanics during in vitro culture and expansion. *Biophys J* **121**, 131–141 (2022).
166. Barlič, A., Drobnič, M., Maličev, E. & Kregar-Velikonja, N. Quantitative analysis of gene expression in human articular chondrocytes assigned for autologous implantation. *J Orthop Res* **26**, 847–853 (2008).
167. Schnabel, M. *et al.* Dedifferentiation-associated changes in morphology and gene expression in primary human articular chondrocytes in cell culture. *Osteoarthritis Cartilage* **10**, 62–70 (2002).
168. Benya, P. D. & Shaffer, J. D. Dedifferentiated chondrocytes reexpress the differentiated collagen phenotype when cultured in agarose gels. *Cell* **30**, 215–224 (1982).
169. Ma, B. *et al.* Gene expression profiling of dedifferentiated human articular chondrocytes in monolayer culture. *Osteoarthritis Cartilage* **21**, 599–603 (2013).
170. Scott, A. K. *et al.* Mechanical memory stored through epigenetic remodeling reduces cell therapeutic potential. *Biophys J* **122**, 1428–1444 (2023).

APPENDIX A

Appendix A H3K9ME3 AS A REGULATOR OF NUCLEAR ARCHITECTURE IN CARDIOMYOCYTES AND CHONDROCYTES

A.1 Cardiomyocytes

A.1.1 Introduction

Most of my thesis work focused on the functional consequences of changes to H3K36 and H3K27 methylation, but there are other important histone modifications related to cell fate, such as H3K9me3. H3K9 methylation is generally associated with transcriptional silencing[136,137], though each methylation state has a nuanced role and distribution in the genome. H3K9me1 localizes to silenced genes in euchromatic regions, although it is also enriched at transcription start sites of actively transcribed genes in mammalian cells[138,139]. By contrast, H3K9me2 marks peripheral heterochromatin[140] and is enriched in lamina-associated domains[141], while H3K9me3 localizes to transposable elements across the genome[142–144] and silences lineage-inappropriate genes during differentiation[136]. Both H3K9me2 and H3K9me3 are enriched at centromeres and telomeric regions as well as in non-coding repetitive regions, thus defining constitutive heterochromatin[145,146]. Similar to other histone methylation sites, H3K9 methylation can also be disrupted using K-to-M mutants (H3K9M) that acts as an orthosteric inhibitor of the H3K9 methyltransferase, G9a[147,148].

As described in Chapter 1 and 2, chromatin modifications are linked to changes in cell fate via transcription. However, chromatin organization can also change during differentiation, and nuclear morphology can have direct implications for cellular functions[149–153]. Indeed, the nucleus is capable of sensing the mechanical environment through proteins that span the inner and outer nuclear membranes[154–163]. We hypothesized that mechanical strains may affect chromatin organization in the nucleus during cellular differentiation. To fill this gap in knowledge, we investigated the chromatin organization in

embryonic cardiomyocytes during development, as well as in adult mice and humans during pathology.

A.1.2 Results

The bulk of the results of these studies, carried out by the Neu lab, can be seen in Seelbinder et. al., 2021[164]. Briefly, we showed that cardiomyocytes maintain a cell type-specific nuclear architecture where chromatin is moved from the interior of the nucleus to the periphery during development. This is mediated by tensile strains transferred from myofibrils to the nucleus via LINC (linker of nucleo- and cytoskeleton) proteins. These tensile strains promote the rearrangement of epigenetically suppressed chromatin to the nuclear periphery. Disruption of LINC-complex, or stiff environments which cause nuclear deformation, abolished the embryonic reorganization of chromatin. Specifically, we examined H3K9me3 and H3K27me3, and observed opposing relocation trends for these chromatin marks. H3K9me3-modified chromatin became peripherally enriched before overall chromatin in embryonic cardiomyocytes, while peripheral enrichment of H3K27me3-modified chromatin indicated formation of a non-contractile cardiac fibroblast cell type.

Figure A.1

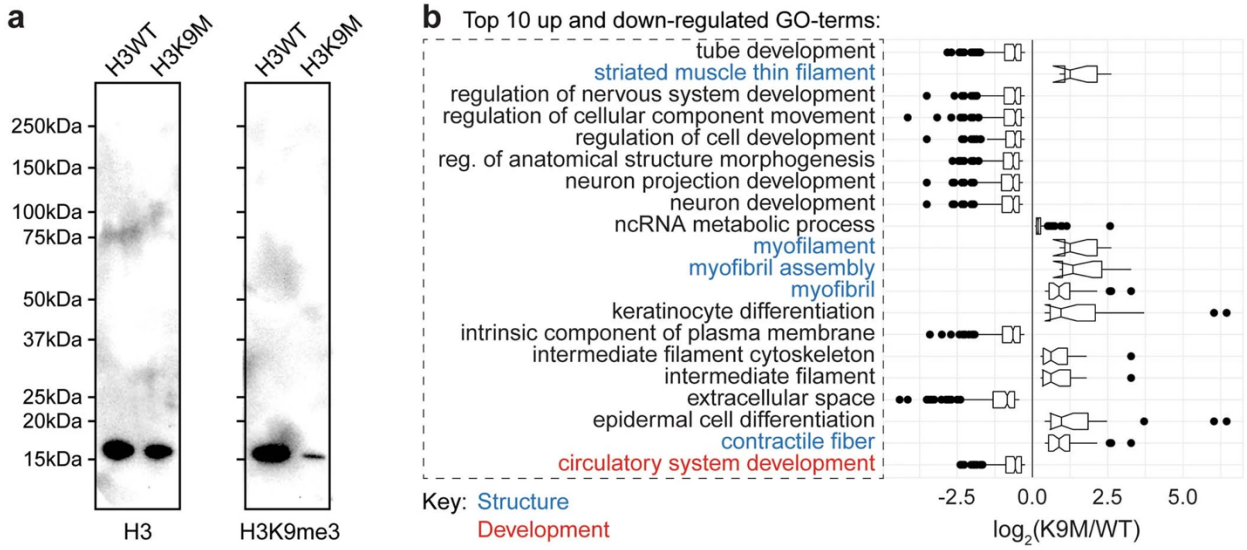

Appendix Figure 1. Inducible expression of H3.3 K-to-M mutant inhibits H3K9 trimethylation and changes cardiac gene expression

(a) Embryonic cardiac cells from H3K9M and H3WT mice were isolated and cultured on soft (13 kPa) PDMS. CMs were induced using 2 μg/ml doxycycline, harvested on day four, and subjected to Western blot analysis for H3K9me3 or H3 as a loading control.
(b) Functional annotation for top genes differentially regulated between H3K9M and H3WT cells, which show a phenotype consistent with CM development.

Given the correlation between H3K9me3 and cardiomyocyte development, I wanted to determine a functional connection between these two concepts. To investigate this question, I mated mice with doxycycline-inducible WT H3 or H3K9M with C57Bl/6 mice to obtain heterozygous pups. We harvested these pups at E18.5 and isolated cardiomyocytes from these embryonic mice. Following expansion in culture, we used doxycycline to induce the mutant or control, and then I confirmed loss of H3K9 methylation via Western blot (Fig. A1a). After 4 days of culture on soft polydimethylsiloxane (PDMS) substrate, peripheral enrichment of H3K9me3-marked chromatin, and indeed all chromatin, was depleted in H3K9M cardiomyocytes compared to control WT H3 or H2b-eGFP cardiomyocytes (Fig. A2a-c). In contrast to H2b-eGFP mice, both H3K9M and WT H3 cardiomyocytes showed no peripheral enrichment of H3K27me3 (Fig. A2a-c). To assess the transcriptional changes related to this phenotype, we performed RNA-seq on H3K9M and WT H3 cardiomyocytes at this timepoint. We found that gene ontology terms related to cardiac development and structure represented some of the top up- and downregulated genes (Fig. A1b). In total, 16 terms related to cardiac development contained genes that were downregulated (Fig. A2d). However, GO terms related to cardiac structural gene expression showed the opposite effect, with their associated genes upregulated (Fig. A2d). This indicates that mechanisms related to H3K9me3 might work primarily to determine cell fate rather than the structural needs of the cell.

Figure A.2

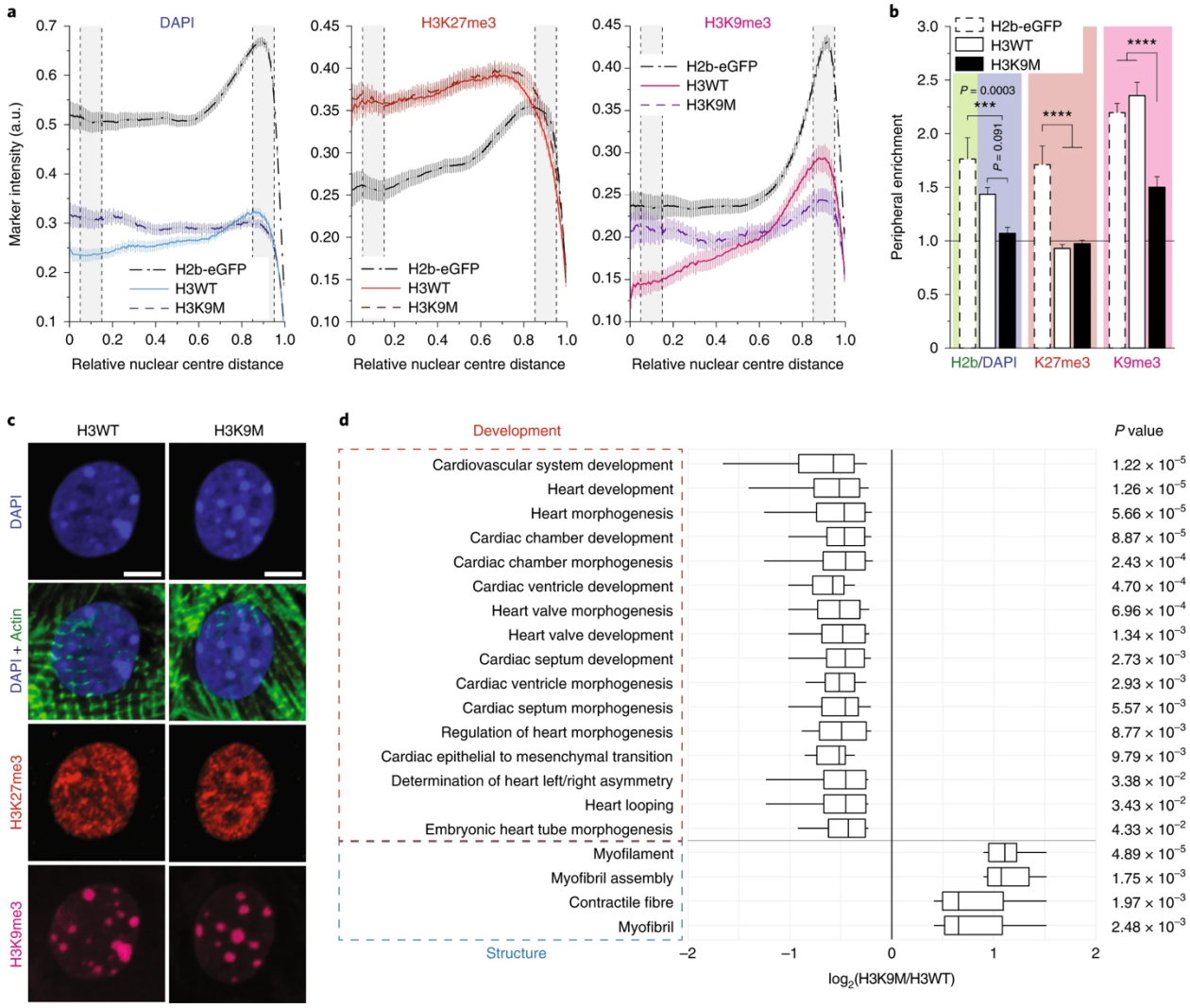

Appendix Figure 2. Suppressing H3K9 methylation via expression of H3K9M mutant histones abrogates chromatin reorganization and decreases expression of cardiac developmental genes

Cardiac cells were isolated from (E)18.5 mouse embryos expressing either mutated H3.3 (H3K9M), which suppressed H3K9me3, or wild-type H3.3 (H3WT) as control, and were cultured for 4 d on soft PDMS.

(a-c) Analysis of peripheral enrichment showed (a,b) that reorganization towards the nuclear envelope of overall (DAPI) and H3K9me3-marked chromatin was abrogated in CMs from H3K9M compared with those from H3WT (c). Day 4 data from H2b-eGFP mice is shown for comparison. Mean + s.e.m., $n = 63$ for H2b-eGFP, $n = 66$ for H3WT and H3K9M, 3 biological repeats, one-way ANOVA with Tukey's HSD.

(d) Total RNA was collected on day 4. RNA-seq analysis between H3K9M and H3WT revealed multiple GO terms related to cardiac development, all of which were downregulated. In contrast, GO terms related to cardiac structural genes were upregulated. Adjusted *P* values of GO terms are shown on the right. Boxplots show the 25th–75th percentiles, with whiskers spanning the full data range, $n = 4$ from 4 biological repeats. Scale bars, 5 μm. ***$P < 0.001$, ****$P < 0.0001$.

A.1.3 Conclusions

In this work, we showed that the location, specifically on the periphery of the nucleus, of chromatin with histone modifications such as H3K9me3 and H3K27me3 is associated with cardiac differentiation. My contribution to this work showed that suppression of H3K9me3 ablates the localization of chromatin marked with this modification at the periphery and reduces gene expression related to cardiac development, thereby suggesting a functional role for H3K9me3 in cardiac development. The connection between histone modifications and nuclear architecture could function to regulate gene expression by localizing repressed or activated genes to different sections of the nucleus to prevent or reinforce activity around those genes. This idea is interesting in the context of H3K36 methylation, which we have established also influences cell fate. It is possible that H3K36me3 may also localize to specific areas of the nucleus with certain genes to further reinforce their expression. Indeed, we note that by transmission electron microscopy, nuclei in H3K36M intestinal cells have an abnormal structure compared to those in WT H3 cells (data not shown). Further work remains to be done to explore the functional connection between other histone modifications, chromatin localization, and cell differentiation.

A.1.4 Methods

A.1.1.1 Mice

For H3K9M and H3WT studies, male mice carrying the transgene were bred to C57BL/6 (Jackson Laboratory) females. Embryonic hearts were collected on day 18.5 post conception.

Tissue digestion and culture conditions were maintained as stated for the H2b-eGFP cardiac cultures. On day 0, 1 and 2, cells were induced with 2 μg ml^{-1} doxycycline (Sigma).

A.1.1.2 RNA-seq

Total RNA was extracted from cardiac cultures after 4 d on either soft or stiff PDMS ($N = 4$) using the Aurum Total RNA mini kit (Bio-Rad Laboratories). Libraries were constructed by the Purdue Genomics Core Facilities according to standard protocols using TruSeq Stranded mRNA Library prep kit (Illumina). For the analysis of H3K9M and H3WT mice ($n = 3$), total RNA was sequenced at the Genomics Shared Resource Facility at the UC Anschutz Medical Campus, and reads were mapped using hisat2 v2.1.0 and custom parameters for the University of California, Santa Cruz mouse genome release mm10. Reads were summarized to genes annotated by UCSC using featureCounts v1.6.2. Count data were further analysed in R 3.6 using DESeq2 to call differentially expressed genes and clusterProfiler for the gene set enrichment analysis of gene ontology pathways. To compare the local impact of H3K9 trimethylation and changes in gene expression, we compared our data to publicly available ChIP-seq datasets from day 16.5 embryo heart from the model organism encyclopaedia of DNA elements (modEncode) using in-house scripts based on DeepTools, and the bamTools and bedTools suite. RNA-seq data can be obtained from the GEO database (GSE178674).

A.1.1.3 Immunofluorescence staining

Cells were fixed in 4% ice-cold paraformaldehyde (PFA) for 10 min, permeabilized with 1% Triton X-100 in PBS buffer for 15 min and blocked with 10% normal goat serum and 1% bovine serum albumin (BSA) in 0.1% PBT (0.1% Tween-20 in PBS) for 60 min. For digitonin experiments, cells were permeabilized in 0.003% digitonin (D141, Sigma) in PBS. Primary incubation was performed at 4 °C overnight in 0.1% PBT containing 1% BSA. Secondary incubation was performed in primary incubation buffer for 45 min (r.t.) at a dilution of 1:500. Actin was counterstained with Phalloidin conjugated to either Texas Red-X for embryonic tissues and marker co-localization in vitro studies (Life Technologies), Alexa Flour 488 for cardiac sections of hypertrophic mice (Life Technologies) or CF405 for all

other in vitro cultures (Biotium). Primary antibodies used were: H3K9me3 (ab8898, Abcam, 1:800), H3K27me3 (ab6002, Abcam, 1:200), RNA polymerase II CTD repeat YSPTSPS phospho S2 (ab24758, Abcam, 1:400), nesprin-1 (ab24742, Abcam, 1:500), DAPI (Invitrogen, 1:1,000) and Emerin (30853S, CST,1:250).

A.1.1.4 Western blot analysis

For H3K9M and H3WT experiments, cells grown in culture for 4 d were prepared for western blotting by nuclear isolation. Cells were incubated in nuclear isolation buffer containing 50 mM Tris-HCl (pH 8), 15 mM NaCl, 60 mM KCl, 5 mM MgCl2, 1 mM $CaCl_2$, 250 mM sucrose, 1 mM dithiothreitol, 0.6% IGEPAL and 1x protease inhibitor (all from Sigma-Aldrich) before pelleting and washing with nuclear isolation buffer one more time. Next, cells were lysed in RIPA buffer (containing 50 mM Tris-HCl (pH 8), 150 mM NaCl, 0.1% SDS, 0.5% sodium deoxycholate, 1% Triton X-100 and 1 mM EDTA), 1x protease inhibitor (all from Sigma-Aldrich) and 0.01 U μl^{-1} benzonase (Novagen). The lysates were then sonicated (Bioruptor Pico sonicator, Diagenode) and cleared by centrifugation to remove cell debris. The supernatant was boiled together with Laemmli sample buffer containing 100 mg ml^{-1} SDS, 250 mM Tris (pH 6.8), 1 mg ml^{-1} bromophenol blue and 50% glycerol (all from Sigma-Aldrich), and loaded into 4–20% mini-Protean TGX precast protein gels (Bio-Rad). Protein was transferred to PVDF membranes (Bio-Rad) and blocked for 1 h. Primary antibodies used were H3 (Abcam, 1791, 1:10,000) and H3K9me3 (Abcam, 8898, 1:1,000). Secondary antibody used was goat anti-rabbit-HRP-conjugated (Invitrogen, PI31460, 1:2,000). Proteins were detected using Immobilon western chemiluminescent HRP substrate (Millipore).

A.2 Chondrocytes

A.2.1 Introduction

Given the relationship between chromatin architecture, H3K9 and H3K27 methylation, and cardiomyocyte differentiation, we were also interested to determine whether this translated to other cell types. Specifically, we were interested in examining

chondrocytes, the cells that make up cartilage and are often cultured for transplantation. Previous work from the Neu lab suggests that changes in nuclear strain due to 2D culture influence chondrocyte cell fate[165]. The stiff environment of 2D culture pushes chondrocytes to proliferate and differentiate, and restoration to a 3D environment allows the chondrocytes to return to a quiescent, round morphology[166–169]. However, the question remains whether 2D stiff mechanical priming may lead to mechanical memory in the chondrocytes and influence their later fate. Our work in cardiomyocytes suggested that H3K9me3 plays a role in spatial chromatin organization during cardiomyocyte differentiation[164], and therefore we hypothesized that H3K9me3 might regulate mechanical memory in chondrocytes exposed to different physical environments, thereby affecting cell fate.

A.2.2 Results

The bulk of the results of these studies, carried out by the Neu lab, can be seen in Scott et. al., 2023[170]. Briefly, in this work we found that cellular plasticity decreased after exposure to stiff environments, even after movement to a new environment. In response to an initial stiff environment, we observed that H3K9me3 specifically relocated from the nuclear envelope to distribute throughout the nucleus over expansion time. After chondrocytes were transferred to 3D culture to dedifferentiate, the H3K9me3-marked chromatin architecture persisted in a dose-dependent manner according to time spent in a 2D environment, suggesting a structural nuclear memory for this histone modification. The persistence of a differentiated chondrocyte phenotype, marked by distributed H3K9me3, was also supported by upregulation of genes associated with differentiated chondrocytes in cells exposed to stiff environments for longer times.

Figure A.3

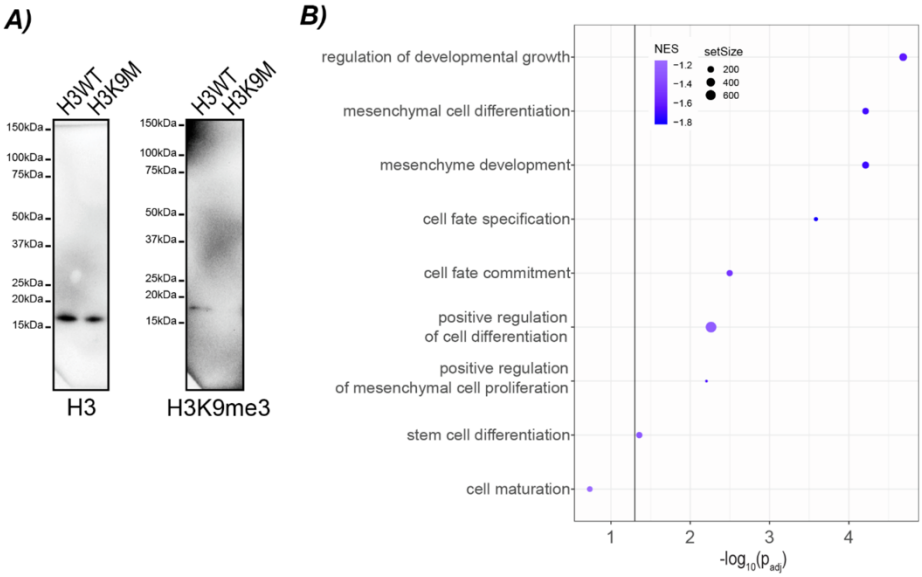

Appendix Figure 3. Suppression of H3K9 methylation led to de-enrichment of cell fate and a subset 50 of chondrogenic pathways.

A) Representative western blot to confirm the suppression of 51 H3K9me3 in comparison to total H3 protein (N=4 biological replicates).

B) Decrease in 52 H3K9me3 caused suppression of pathways related to cell fate commitment (N=3 biological replicates).

Given this association between H3K9me3 changes during chondrocyte dedifferentiation in 3D environments, I examined whether we could functionally connect this histone modification to chondrocyte phenotypes. I mated mice with doxycycline-inducible WT H3 or H3K9M with C57Bl/6 mice to obtain heterozygous pups. We harvested these pups at E18.5 and isolated chondrocytes from these embryonic mice. We used doxycycline to induce the mutant or control, and then I confirmed loss of H3K9me3 via Western blot (Fig. A3a). Interestingly, though we noted overall loss in fluorescent intensity of H3K9me3 in H3K9M chondrocytes compared to WT H3, there were minimal changes in overall H3K9me3-marked chromatin architecture compared to WT H3, measured by number of foci and nuclear area (Fig. A4a-c). We next asked if there were changes in gene expression after suppression of H3K9 methylation. There were 392 genes differentially expressed between WT H3 and H3K9M chondrocytes, however few of the known chondrogenic or dedifferentiation genes were significantly different between the two genotypes (Fig. A4d-e). Despite this, functional annotation revealed that overall gene

expression signatures characteristic of chondrocytes were de-enriched in H3K9M samples (Fig. A4g). After comparing these samples to previously published chondrocyte gene expression data by principal-component analysis, we noted that both WT H3 and H3K9M clustered separately from native chondrocytes, suggesting a similar adaptation of our cells to the 2D stiff culture (Fig. A4f). Therefore, we hypothesized that H3K9me3 might regulate chondrocyte cell fate through other pathways not directly related to dedifferentiation. Indeed, examining genes related to cell fate commitment in H3K9M samples compared to WT H3 confirmed their downregulation (Fig. A3b). After increasing levels of H3K9me3 by inhibiting demethylases, dedifferentiation-based chromatin remodeling was partially blocked, and chondrogenic genes increased in expression. Therefore, we speculate that the chromatin architecture of H3K9me3, not necessarily the levels of H3K9me3, are associated with maintaining the chondrocyte phenotype.

Figure A.4

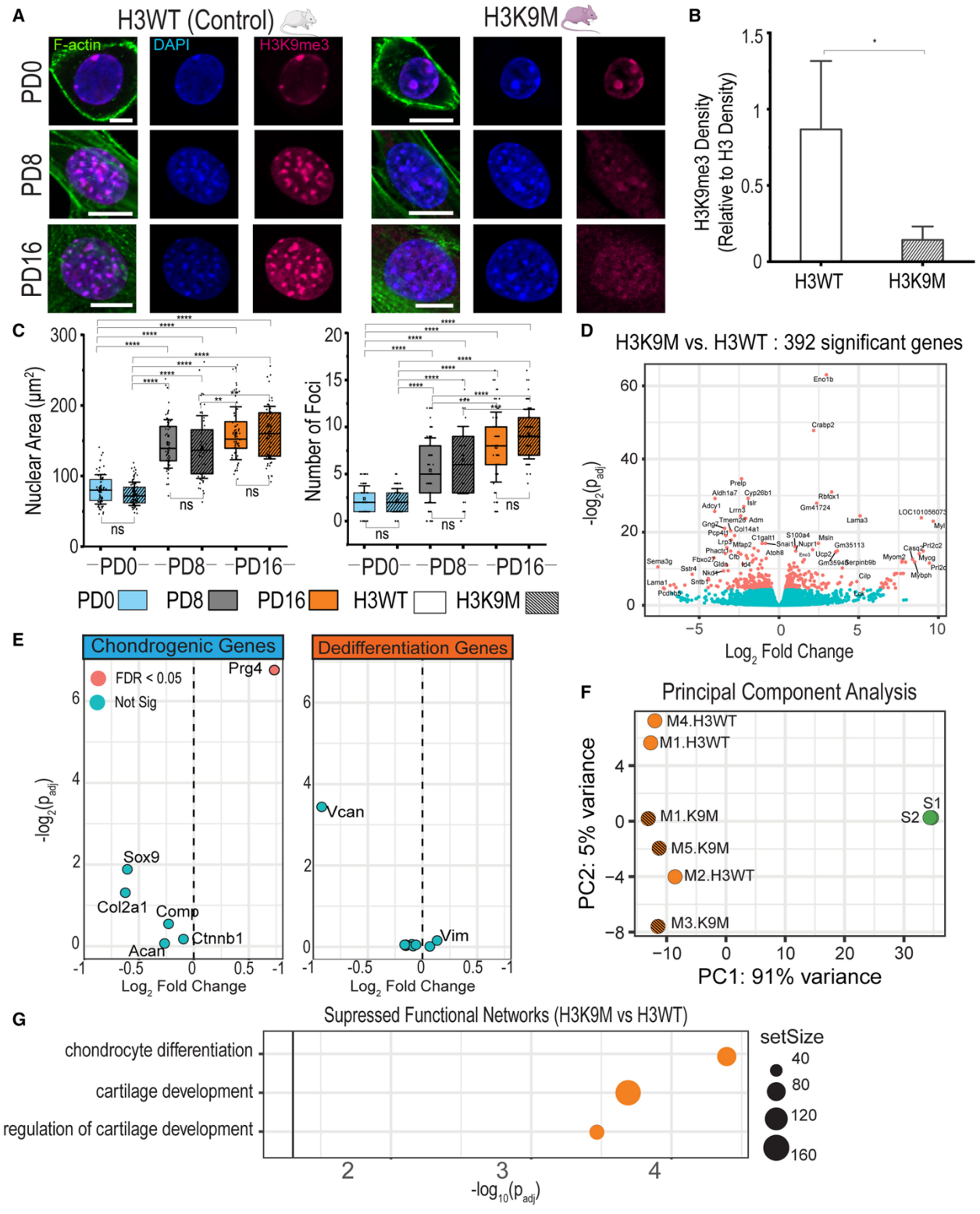
A
H3WT (Control)
H3K9M
F-actin
DAPI
H3K9me3
PD0
PD8
PD16
B
H3K9me3 Density (Relative to H3 Density)
H3WT
H3K9M
C
Nuclear Area (µm²)
Number of Foci
PD0
PD8
PD16
H3WT
H3K9M
ns
D
H3K9M vs. H3WT : 392 significant genes
-log2(padj)
Log2 Fold Change
E
Chondrogenic Genes
Dedifferentiation Genes
FDR < 0.05
Not Sig
Prg4
Sox9
Col2a1
Comp
Ctnnb1
Acan
Vcan
Vim
-log2(padj)
Log2 Fold Change
F
Principal Component Analysis
M4.H3WT
M1.H3WT
M1.K9M
M5.K9M
M2.H3WT
M3.K9M
S1
S2
PC2: 5% variance
PC1: 91% variance
G
Supressed Functional Networks (H3K9M vs H3WT)
chondrocyte differentiation
cartilage development
regulation of cartilage development
setSize
40
80
120
160
-log10(padj)

Appendix Figure 4. Suppression of H3K9me3 did not prevent nuclear architecture remodeling of H3K9 trimethylated chromatin and dedifferentiation of expanded chondrocytes.

(A) Chondrocytes were isolated from H3K9M mice or H3WT mice and expanded to PD16. Immunofluorescence imaging showed a decrease in H3K9me3 signal in the H3K9M cells because of the suppressed levels of H3K9me3, but the nuclear architecture changes (H3K9me3 foci) from PD0 to PD16 appeared similar to control cells.

(B) Quantified H3K9me3 density relative to total H3 density from Western blots decreased in H3K9M cells compared with H3WT cells to confirm suppression of H3K9me3 (+SD, N = 4 biological replicates). $^{*}p < 0.05$.

(C) Nuclear area and number of H3K9me3 foci did not change significantly between H3WT and H3K9M cells of the same passage (±SD, N = 4 biological replicates, n > 16 nuclei/genotype/replicate). $^{*}p < 0.05$, $^{**}p < 0.01$, $^{***}p < 0.001$, $^{****}p < 0.0001$, ns: $p > 0.05$.

(D) RNA-seq analysis revealed 392 significantly differentially expressed genes between PD16 H3K9M and H3WT cells.

(E) However, most chondrogenic and dedifferentiation genes were not significantly expressed when comparing PD16 H3K9M and H3WT cells.

(F) Compared with previously published data of native chondrocytes (samples S1 and S2), principal-component analysis revealed that 91% of the variance of the changes in gene expression in the system can be accounted for by the difference between the expanded (M1–M5 samples) and the native chondrocytes (S1, S2), indicating that both H3K9M and H3WT cells dedifferentiated and differ between them in a much smaller proportion.

(G) Although the lack of H3K9me3 did not prevent dedifferentiation, H3K9me3 did play a protective role in maintaining the chondrocyte phenotype since chondrogenic pathways were suppressed significantly for H3K9M cells.

A.2.3 Conclusions

With this work, we established that mechanical memory exists in chondrocytes exposed to 2D and then 3D environments, and this is partially influenced by H3K9me3-marked chromatin architecture changes. My contribution to this work showed that suppression of H3K9me3 did not prevent the chromatin architecture remodeling nor

dedifferentiation of chondrocytes when exposed to stiff 2D substrates, suggesting that not level of H3K9me3, but architecture of the chromatin, is what supports chondrocyte cell fate change in this context. In cardiomyocytes, we examined the process of differentiation and found that disruption of H3K9me3 via H3K9M impacted cell fate through changes to nuclear architecture and gene expression. It would be interesting to examine chondrocytes in a differentiation context, as it seems possible that H3K9me3 may play a different role there, perhaps more similar to cardiomyocyte differentiation. Many questions remain about how the chromatin environment impacts the mechanical memory of these and other cell types, and how this may improve strategies for tissue regeneration.

A.2.4 Methods

A.2.1.1 2D cell culture of H3K9M and H3WT murine chondrocytes

For H3.3 lysine-to-methionine mutant (H3K9M) and wild-type H3.3 (H3WT; control) studies, male mice carrying the transgene were bred to C57BL/6 (Jackson Laboratory, Bar Harbor, ME, USA, cat. no. 000664) female mice. The methods were performed in accordance with relevant guidelines and regulations and approved by the Institutional Animal Care and Use Committee. Mice were maintained in specific-pathogen-free, temperature-controlled housing with 12 h light cycles and received food and water ad libitum. Chondrocytes from embryonic (embryonic day 18.15) H3K9M and H3WT mice were harvested and cultured with chondrocyte media and 2 μg/mL doxycycline (Sigma, cat. no. D3072-1mL) for PD0, PD8, and PD16 on TCP (Corning, cat. no. 430165, or Ibidi, cat. no. 80841). To harvest embryonic chondrocytes, hind limb articular cartilage was isolated and washed 3× with PBS, transferred to 3 mg/mL collagenase-P solution in DMEM F12 (with 1× penicillin/streptomycin), digested for 12 hr at 37°C, filtered through a 70 μm mesh strainer, and plated at a density of 4×10^4 cells/cm^2.

A.2.1.2 Immunofluorescence staining and imaging

We fixed cells cultured on TCP in 4% paraformaldehyde (PFA; Electron Microscopy Sciences, Hatfield, PA, USA, cat. no. 15714-S) for 10 min and permeabilized

them in 1% Triton-X100 (Sigma, cat. no. 78787-100mL) in PBS for 10 min. Before incubating with the primary antibodies, we blocked by incubating the cells with 10% natural goat serum (Invitrogen, Waltham, MA, USA, cat. no. 10000C), 1% bovine serum albumin (BSA) in 0.1% PBT (0.1% Tween-20, Bio-Rad, Hercules, CA, USA, cat. no. 170-6531, in PBS) for 60 min at room temperature (RT). We performed the primary antibody incubation in 0.1% PBT containing 1% BSA at 4°C overnight (12 h) and the H3K9me3 primary antibody (Abcam, Cambridge, UK, ab8898, 1:600) with agitation. Following the primary incubation, we performed the secondary incubation in 0.1% PBT containing 1% BSA, with Alexa Fluor 633 goat anti-rabbit immunoglobulin G (Life Technologies, Carlsbad, CA, USA, cat. No. A21070) at a dilution of 1:500 for 45 min (RT) with agitation. To visualize both actin and DNA, we counterstained with 488 Phalloidin (Invitrogen, cat. no. A12379, 1:80, 20 min incubation in PBS) and DAPI (Invitrogen, cat. no. D1306, 1:1000, 10 min incubation in PBS), respectively.

To stain cells encapsulated in 3D HA-PEGDA hydrogels, we used a similar protocol. However, we fixed the cells in 4% PFA for 30 min, permeabilized them in 1% Triton-X100 in PBS for 15 min, and blocked them with 5% natural goat serum and 1% BSA in 0.1% PBT for 60 min. The primary antibody incubation was performed in 0.1% PBT containing 1% BSA at 4°C for 16 h with agitation. Secondary incubation was also performed in 0.1% PBT containing 1% BSA at a dilution of 1:200 for 2 h (RT) with agitation. Lastly, we counterstained both actin and DNA with 488 Phalloidin (1:80, 40 min incubation in PBS) and DAPI (1:500, 15 min incubation in PBS), respectively.

Using an inverted Nikon A1R confocal microscope with a 60× oil immersion objective, we imaged both encapsulated cells and cells grown on TCP from all time points, treatments, and genotypes. Specifically, we imaged the nucleus/DNA (DAPI; 405 nm), actin (phalloidin; 488 nm), and H3K9me3 (640 nm).

A.2.1.3 RNA sequencing (RNA-seq) gene expression

H3K9M and H3WT chondrocytes were cultured in the presence of doxycycline (2 μg/mL) for PD16 and lysed with Qiazol, and RNA was extracted using Direct-zol RNA MiniPrep (Zymo Research, cat. no. R2050). Poly A-selected RNA was sequenced at the Genomics Shared Resource Facility at UC Anschutz Medical Campus (Aurora, CO, USA). We mapped reads

using hisat2 v.2.1.0 and custom parameters to the UCSC mouse genome release mm10. We summarized reads to genes annotated by UCSC using featureCounts v.1.6.2. We further assessed count data in R 3.6 using DESeq2 to analyze differentially expressed genes and used clusterProfiler for the gene set enrichment analysis of Gene Ontology pathways. We compared our data with publicly available RNA-seq data of embryonic proliferating chondrocytes using in-house scripts based on DeepTools and the bamTools and bedTools suite. Our RNA-seq data are found on the NIH GEO database (GEO: GSE190339).

A.2.1.4 Western blot

Following PD16, H3K9M and H3WT chondrocytes were prepared for Western blot analysis by nuclear isolation following a previously reported protocol[164]. Briefly, cells were resuspended in cold nuclear isolation buffer (50 mM Tris-HCl pH 8, 15 mM NaCl, 60 mM KCl, 5 mM $MgCl_2$, 1 mM $CaCl_2$, 250 mM sucrose, 1 mM dithiothreitol, 0.6% IGEPAL (Sigma-Aldrich)) supplemented with complete protease inhibitors (Sigma-Aldrich) and incubated for 5 min on ice. Isolated nuclei were then centrifuged (960 × g for 5 min), washed in nuclear isolation buffer and lysed in RIPA buffer (50 mM Tris-HCL (pH 8), 150 mM NaCl, 0.1% SDS, 0.5% sodium deoxycholate, 1% Triton X-100 and 1 mM EDTA (all from Sigma-Aldrich) supplemented with complete protease inhibitors (Sigma-Aldrich) and 0.01 U µl–1 benzonase (Novagen). We sonicated the resulting lysates 10 times for 30 s with a 30 s pause between pulses using a Bioruptor Pico sonicator (Diagenode). The lysates were then cleared to remove cell debris through centrifuging and collecting the supernatant which was boiled together with Laemmli sample buffer (100 mg mL–1 SDS, 250 mM Tris pH 6.8, 1 mg mL–1 bromophenol blue and 50% glycerol (all from Sigma-Aldrich) and loaded into 4–20% mini-Protean TGX precast protein gels (BioRad). Protein was transferred to PVDF membranes (Bio-Rad) and blocked for 1 h in 5% powdered milk in Tris-buffered saline and Tween-20. The following primary antibodies were used: H3K9me3 (Abcam, 8898; 1:1000), H3 (Abcam, 1791; 1:10,000 dilution). Goat, anti-rabbit-HRP-conjugated (Invitrogen, PI31460; 1:2000 dilution) was used as the secondary antibody. Immobilon western chemiluminescent HRP substrates (Millipore) were used to detect proteins.

SUPPLEMENTAL INFORMATION

Figure S1

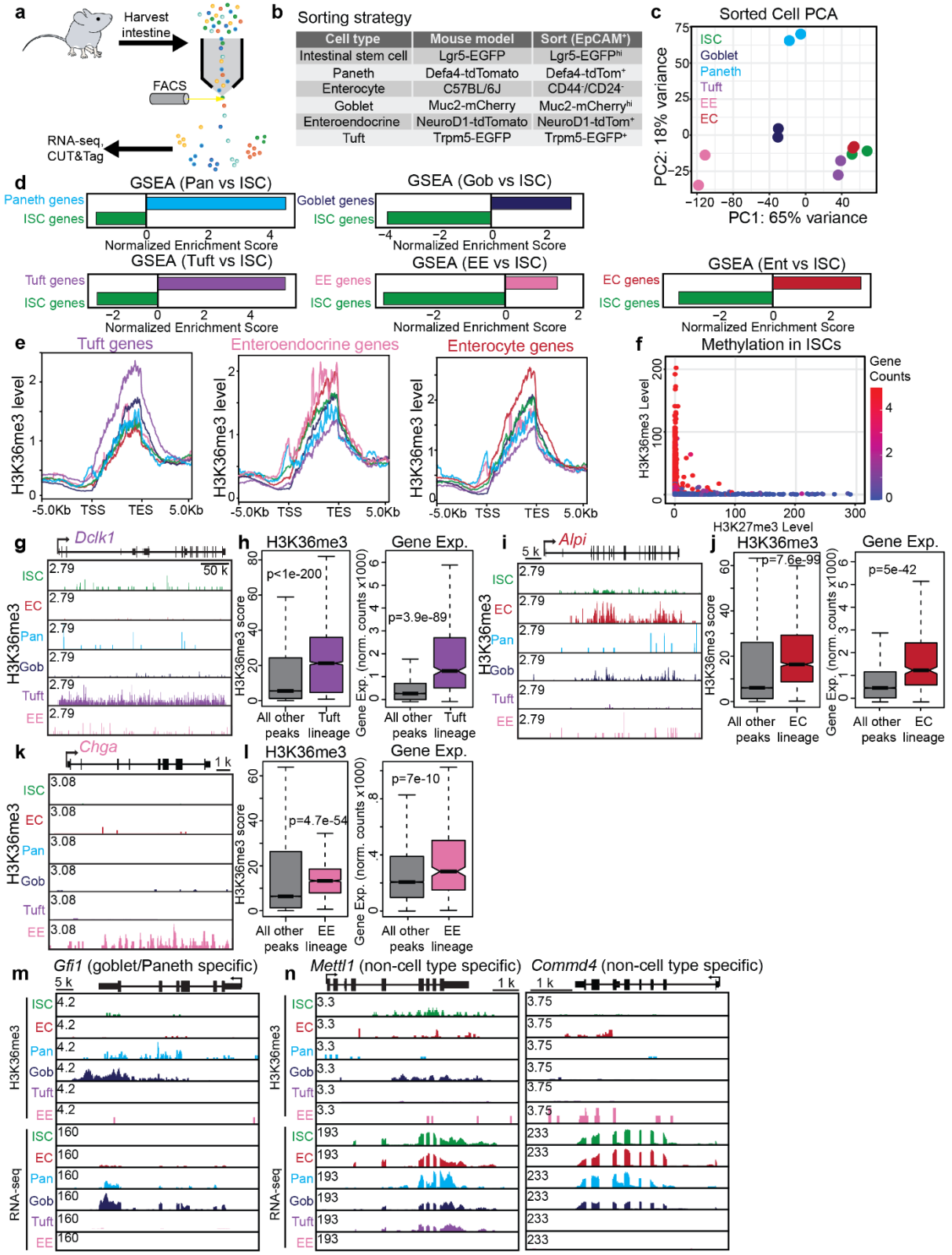

Supplemental Figure 1. Intestinal epithelial cells have distinct H3K36 methylation profiles.

(a) A schematic of the strategy used to sort and profile intestinal epithelial cell types.
(b) Mouse lines used to sort intestinal epithelial cell types.
(c) Multidimensional scaling analysis based on RNA-seq from sorted intestinal epithelial cells (n = 2 biological replicates each).
(d), Gene set enrichment analysis based on RNA-seq data for each sorted cell type compared to ISCs, using published gene sets[96].
(e) Meta-analysis of H3K36me3 at published cell-type associated genes[96] in each sorted cell type (representative trace for 2 biological replicates).
(f) Correlation analysis for H3K36me3 and H3K27me3 in 10,000 randomly selected bins across the genome. The color of each dot represents gene expression (counts) in that bin.
(g) Gene tracks for H3K36me3 at *Dclk1*, a tuft cell-associated gene (representative track for 2 biological replicates).
(h) Left, boxplots for H3K36me3 levels for a published[96] tuft cell-associated gene set and all other genes; right, boxplots for gene expression for a published[96] tuft cell-associated gene set and all other genes (n = 2 biological replicates; Wilcoxon test; box plot shows the median, box plot center lines represent the median, box edges represent the first and third quartiles, and whiskers indicate minimum and maximum values).
(i) Gene tracks for H3K36me3 at *Alpi*, an enterocyte-associated gene (representative track for 2 biological replicates).
(j) Left, boxplots for H3K36me3 levels for a published[96] enterocyte-associated gene set and all other genes; right, boxplots for gene expression for a published[96] enterocyte-associated gene set and all other genes (n = 2 biological replicates; Wilcoxon test; box plot shows the median, box plot center lines represent the median, box edges represent the first and third quartiles, and whiskers indicate minimum and maximum values).
(k) Gene tracks for H3K36me3 at *Chga*, an enteroendocrine cell-associated gene (representative track for 2 biological replicates).
(l) Left, boxplots for H3K36me3 levels for a published[96] enteroendocrine cell-associated gene set and all other genes; right, boxplots for gene expression for a published[96] enteroendocrine cell-associated gene set and all other genes (n = 2 biological replicates; Wilcoxon test; box plot shows the median, box plot center lines represent the median, box

edges represent the first and third quartiles, and whiskers indicate minimum and maximum values).

(m) Representative gene tracks for H3K36me3 and RNA-seq data for each sorted cell type over *Gfi1*, a Paneth- and goblet-specific gene (n = 2 biological replicates).

(n) Representative gene tracks of H3K36me3 and RNA-seq data for each sorted cell type over *Mettl1* and *Commd4*, non-cell type-specific genes that are expressed in Paneth and goblet cells (n = 2 biological replicates).

Figure S2.

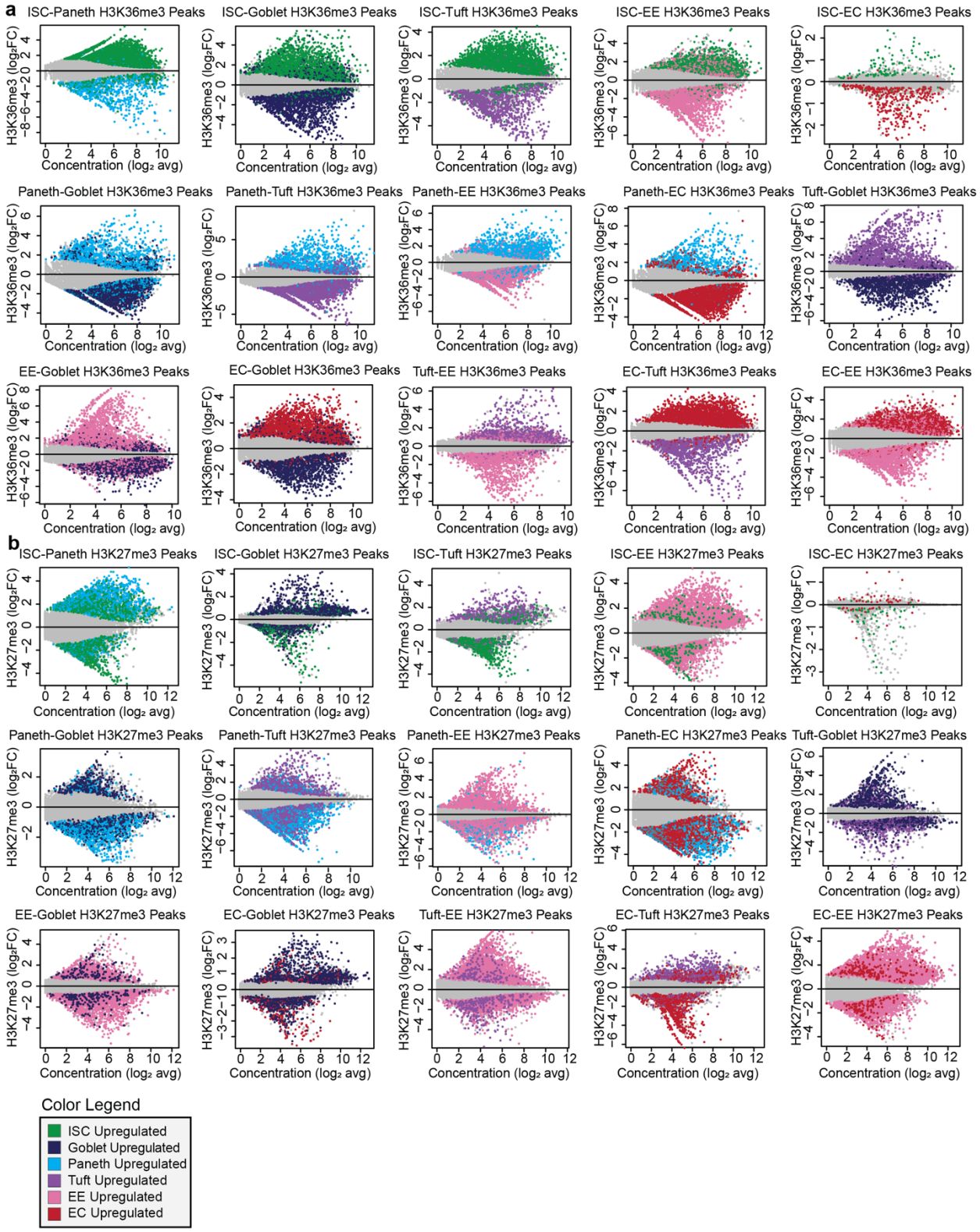
a
ISC-Paneth H3K36me3 Peaks
ISC-Goblet H3K36me3 Peaks
ISC-Tuft H3K36me3 Peaks
ISC-EE H3K36me3 Peaks
ISC-EC H3K36me3 Peaks
Paneth-Goblet H3K36me3 Peaks
Paneth-Tuft H3K36me3 Peaks
Paneth-EE H3K36me3 Peaks
Paneth-EC H3K36me3 Peaks
Tuft-Goblet H3K36me3 Peaks
EE-Goblet H3K36me3 Peaks
EC-Goblet H3K36me3 Peaks
Tuft-EE H3K36me3 Peaks
EC-Tuft H3K36me3 Peaks
EC-EE H3K36me3 Peaks
b
ISC-Paneth H3K27me3 Peaks
ISC-Goblet H3K27me3 Peaks
ISC-Tuft H3K27me3 Peaks
ISC-EE H3K27me3 Peaks
ISC-EC H3K27me3 Peaks
Paneth-Goblet H3K27me3 Peaks
Paneth-Tuft H3K27me3 Peaks
Paneth-EE H3K27me3 Peaks
Paneth-EC H3K27me3 Peaks
Tuft-Goblet H3K27me3 Peaks
EE-Goblet H3K27me3 Peaks
EC-Goblet H3K27me3 Peaks
Tuft-EE H3K27me3 Peaks
EC-Tuft H3K27me3 Peaks
EC-EE H3K27me3 Peaks
H3K36me3 (log₂FC)
H3K27me3 (log₂FC)
Concentration (log₂ avg)
Color Legend
ISC Upregulated
Goblet Upregulated
Paneth Upregulated
Tuft Upregulated
EE Upregulated
EC Upregulated

Supplemental Figure 2. H3K36me3 is largely distinct between intestinal epithelial cell types.

(a) Pairwise comparison of H3K36me3 between the indicated cell types. Colored dots indicate peaks over genes differentially expressed between each cell type. Gray dots represent 10,000 randomly selected peaks over non-significantly differentially expressed genes.

(b) Pairwise comparison of H3K27me3 between the indicated cell types. Colored dots indicate peaks over genes differentially expressed between each cell type. Gray dots represent 10,000 randomly selected peaks over non-significantly differentially expressed genes.

Figure S3.

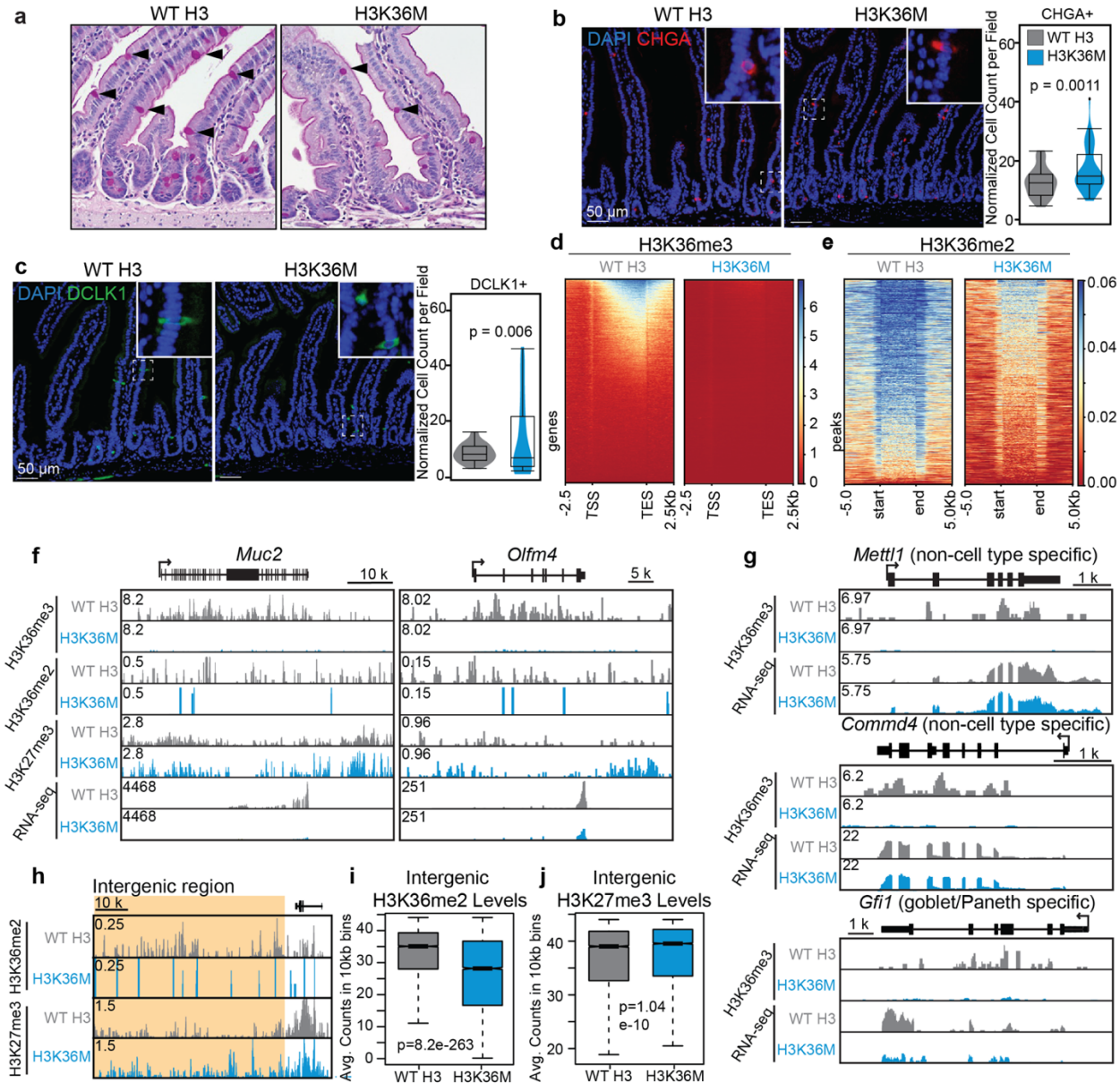

Supplemental Figure 3. Suppressing H3K36 methylation disrupts intestinal homeostasis.

(a) Periodic acid-Schiff stain on intestinal sections from WT H3 and H3K36M mice treated for 4 weeks with dox. Black arrows indicate secretory cells (n = 2 biological replicates each). **(b)** Representative images of immunofluorescence for CHGA, a marker of enteroendocrine cells, in WT H3 and H3K36M intestinal sections. The inset is a magnified image of a positive cell. Scale bar=50 μm. (left, n = 2 mice each genotype). Quantification of enteroendocrine cells (right, n=10 images per mouse; unpaired two-tailed student's t-test;

box plot center lines represent the median, box edges represent the first and third quartiles, and whiskers indicate minimum and maximum values).

(c) Representative images of immunofluorescence for DCLK1, a marker of tuft cells, in WT H3 and H3K36M intestinal sections. The inset is a magnified image of a positive cell. Scale bar=50 μm. (left, n = 2 mice each genotype). Quantification of enteroendocrine cells (right, n = 10 images per mouse; unpaired two-tailed student's t-test; box plot center lines represent the median, box edges represent the first and third quartiles, and whiskers indicate minimum and maximum values).

(d) H3K36me3 signal over all genes in representative WT H3 and H3K36M samples (n = 2 biological replicates each).

(e) H3K36me2 levels at all domains of H3K36me2 in representative WT H3 and H3K36M samples (n = 2 biological replicates each).

(f) Representative gene tracks for H3K36me3, H3K36me2, H3K27me3, and RNA-seq for WT H3 and H3K36M samples over *Muc2*, a marker of goblet cells, and *Olfm4*, a marker of ISCs (n = 2 biological replicates each).

(g) Representative gene tracks for H3K36me3 and RNA-seq over *Gfi1*, a goblet/ Paneth cell marker, and *Mettl1* and *Commd4*, non-cell type-specific genes (n = 2 biological replicates each).

(h) Representative gene tracks for H3K36me2 and H3K27me3 over genic (white) and intergenic (orange) regions in WT H3 and H3K36M samples (n = 2 biological replicates each).

(i) Quantification of H3K36me2 counts in 10,000 randomly selected 10 kb bins from intergenic regions across the mouse genome in WT H3 and H3K36M mice (Wilcoxon test; box plot center lines represent the median, box edges represent the first and third quartiles, and whiskers indicate minimum and maximum values).

(j) Quantification of H3K27me3 counts in 10,000 randomly selected 10 kb bins from intergenic regions across the mouse genome in WT H3 and H3K36M mice (Wilcoxon test; box plot center lines represent the median, box edges represent the first and third quartiles, and whiskers indicate minimum and maximum values).

Figure S4.

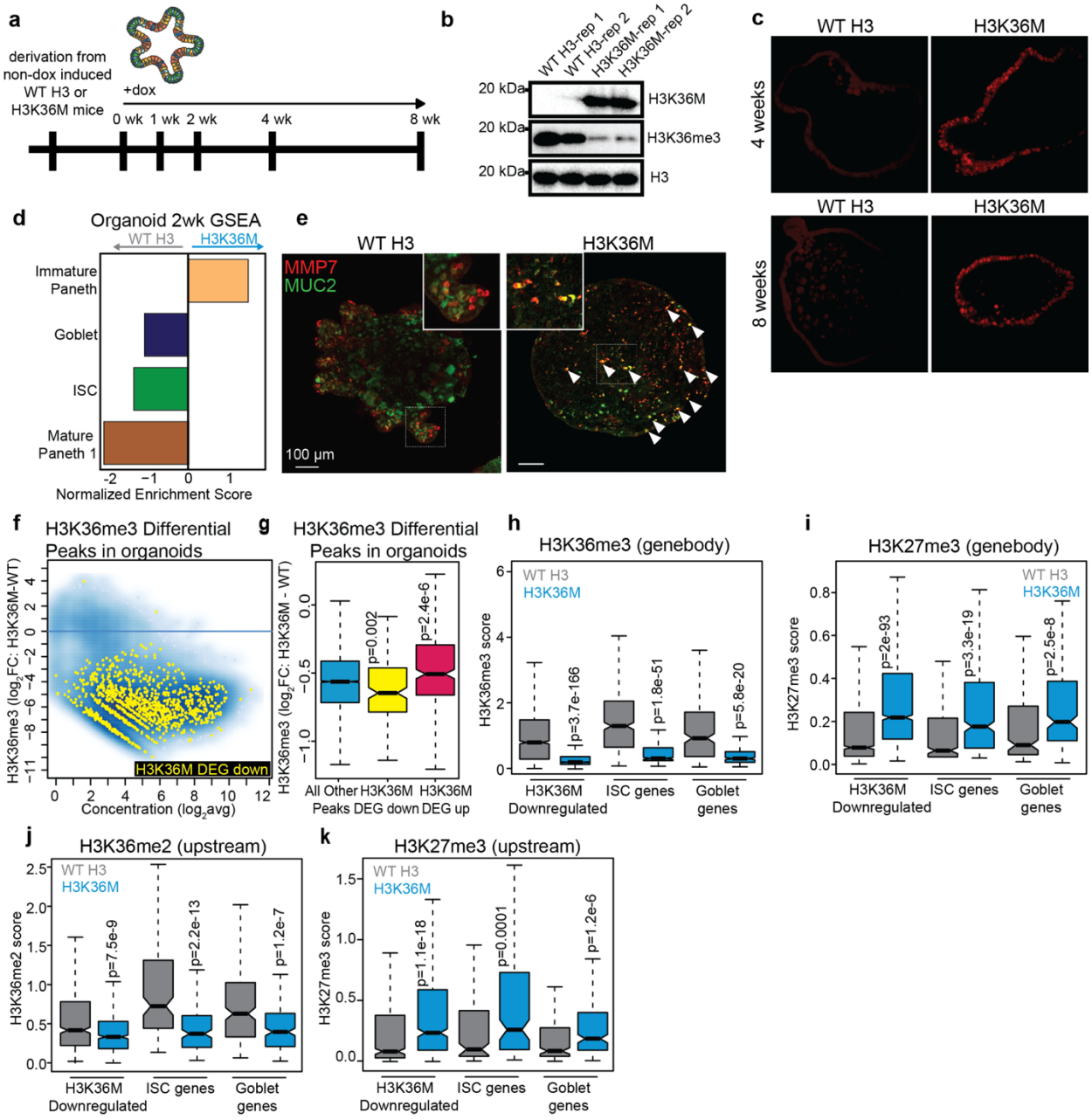

Supplemental Figure 4. Expressing H3K36M in intestinal organoids recapitulate phenotypes observed in mice.

(a) A schematic of intestinal organoid derivation from non-induced WT H3 or H3K36M mice, followed by dox induction in culture.

(b) Western blot analysis on intestinal organoids after one week of dox induction (n = 2 biological replicates).

(c) Representative images of whole-mount immunofluorescence staining for H3K36M in WT H3 and H3K36M organoids induced for four and eight weeks. (n = 2 biological replicates).

(d) Gene set enrichment analysis based on RNA-seq analysis comparing WT H3 and H3K36M organoids after two weeks of induction, using published gene[96] sets and gene sets from Paneth scRNA-seq.

(e) Representative images of whole-mount immunofluorescence staining for MMP7, a marker of Paneth cells, and MUC2, a marker of goblet cells, in WT H3 and H3K36M organoids induced for eight weeks. Scale bar = 100 μm. (n = 2 biological replicates).

(f) Differential H3K36me3 peaks between WT H3 and H3K36M organoids induced for four weeks. Yellow dots indicate peaks over significantly downregulated genes from RNA-seq (n=2 biological replicates; downregulated genes are defined as p-value < 0.05 and $\log_2$FC > 1).

(g) Quantification of H3K36me3 over all genes, H3K36M organoid downregulated genes, and H3K36M organoid upregulated genes (Wilcoxon test; box plot shows the median, box plot center lines represent the median, box edges represent the first and third quartiles, and whiskers indicate minimum and maximum values).

(h) Quantification of H3K36me3 binned into 10 kb regions over the gene body of all H3K36M downregulated genes, ISC-associated genes, and goblet cell-associated genes[96] (Wilcoxon test; box plot center lines represent the median, box edges represent the first and third quartiles, and whiskers indicate minimum and maximum values).

(i) Quantification of H3K27me3 binned into 10 kb regions over the gene body of all H3K36M downregulated genes, ISC-associated genes, and goblet cell-associated genes[96] (Wilcoxon test; box plot center lines represent the median, box edges represent the first and third quartiles, and whiskers indicate minimum and maximum values).

(j) Quantification of H3K36me2 binned into 1 kb regions upstream of the gene body of all H3K36M downregulated genes, ISC-associated genes, and goblet cell-associated genes[96] (Wilcoxon test; box plot center lines represent the median, box edges represent the first and third quartiles, and whiskers indicate minimum and maximum values).

(k) Quantification of H3K27me3 binned into 1 kb regions upstream of the gene body of all H3K36M downregulated genes, ISC-associated genes, and goblet cell-associated genes[96]

(Wilcoxon test; box plot center lines represent the median, box edges represent the first and third quartiles, and whiskers indicate minimum and maximum values).

Figure S5.

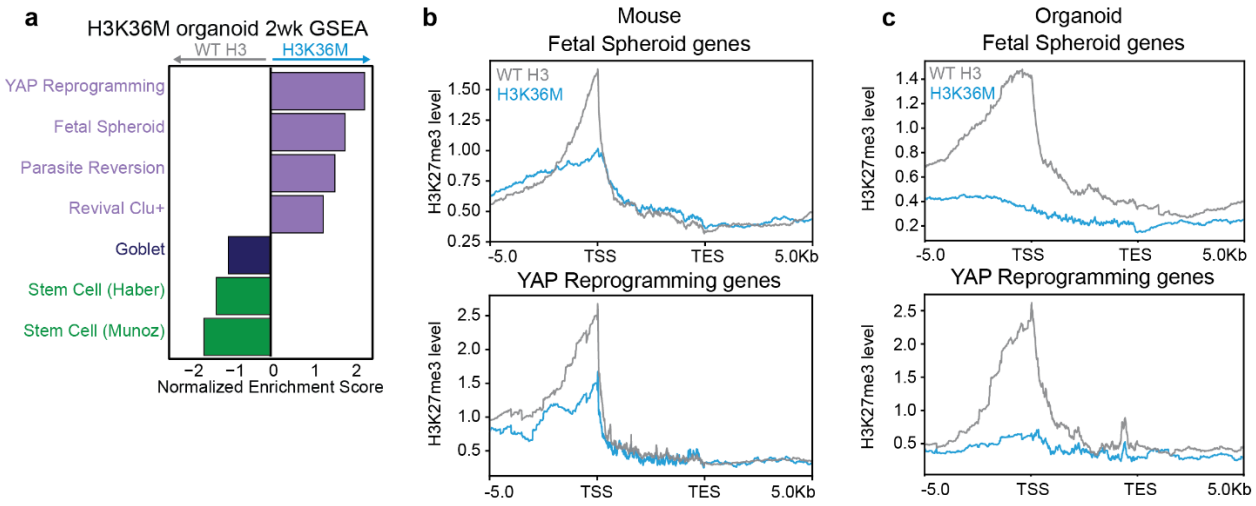

Supplemental Figure 5. Suppressing H3K36 methylation leads to decreased H3K27me3 at regenerative genes in mice and organoids.

(a) Gene set enrichment analysis based on RNA-seq comparing WT H3 and H3K36M organoids after two weeks of induction, using published regenerative and mature cell type-specific gene sets[82,96,107–109,111].

(b) Meta-analysis of H3K27me3 over regenerative gene sets in WT H3 and H3K36M mice (5kb window around the TSS and TES, representative trace for 2 biological replicates).

(c) Meta-analysis of H3K27me3 over regenerative gene sets in WT H3 and H3K36M organoids induced for four weeks (5kb window around the TSS and TES, representative trace for 2 biological replicates).

Figure S6.

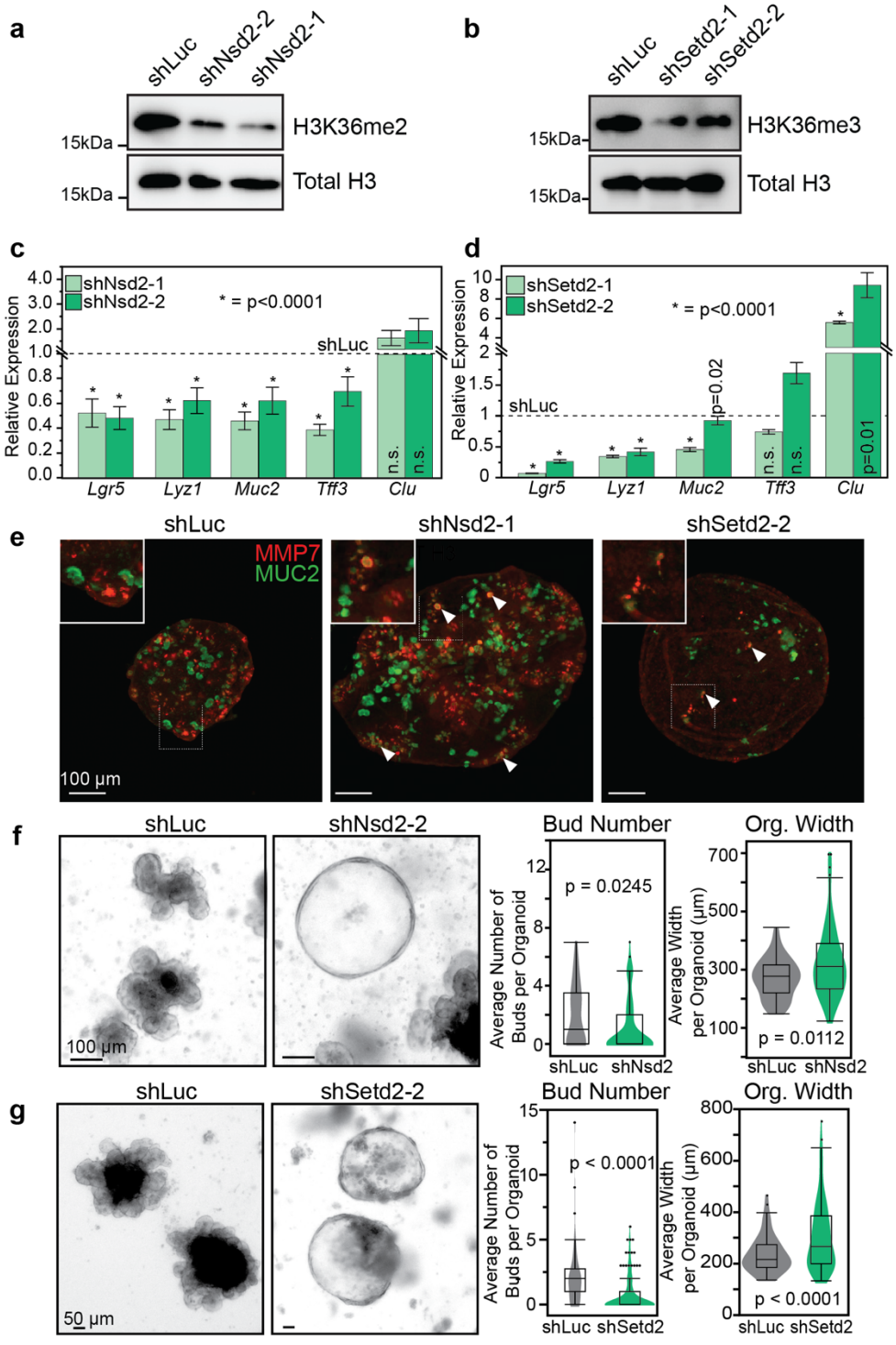
a
shLuc
shNsd2-2
shNsd2-1
15kDa
H3K36me2
15kDa
Total H3
b
shLuc
shSetd2-1
shSetd2-2
15kDa
H3K36me3
15kDa
Total H3
c
shNsd2-1
shNsd2-2
* = p<0.0001
shLuc
Relative Expression
Lgr5
Lyz1
Muc2
Tff3
Clu
n.s.
n.s.
d
shSetd2-1
shSetd2-2
* = p<0.0001
shLuc
p=0.02
p=0.01
n.s.
n.s.
Relative Expression
Lgr5
Lyz1
Muc2
Tff3
Clu
e
shLuc
shNsd2-1
shSetd2-2
MMP7
MUC2
100 µm
f
shLuc
shNsd2-2
100 µm
Bud Number
p = 0.0245
Average Number of Buds per Organoid
shLuc
shNsd2
Org. Width
p = 0.0112
Average Width per Organoid (µm)
shLuc
shNsd2
g
shLuc
shSetd2-2
50 µm
Bud Number
p < 0.0001
Average Number of Buds per Organoid
shLuc
shSetd2
Org. Width
p < 0.0001
Average Width per Organoid (µm)
shLuc
shSetd2

Supplemental Figure 6. Knockdown of H3K36 methyltransferases, *Nsd2* or *Setd2*, phenocopy H3K36M expression in organoids.

(a) Western blot analysis for organoids transduced with shRNAs targeting either *Nsd2* or a luciferase control.

(b) Western blot analysis for organoids transduced with shRNAs targeting either *Setd2* or a luciferase control.

(c) RT-qPCR on shNsd2 or control organoids for markers of stem cells, secretory cells, or regeneration (n = 2 independent replicates per shRNA; unpaired two-tailed student's t-test; errors bars represent standard deviation).

(d) RT-qPCR on shSetd2 or control organoids for markers of stem cells, secretory cells, or regeneration (n = 2 independent replicates per shRNA; unpaired two-tailed student's t-test; errors bars represent standard deviation).

(e) Representative images of immunofluorescence for MMP7, a marker of Paneth cells, and MUC2, a marker of goblet cells, in shNsd2, shSetd2, or control organoids. Scale bar=100 μm. (n = 2 replicates per target).

(f) Left, representative brightfield images of shNsd2 or control organoids. Scale bar 100 μm. Middle, quantification of organoid budding in shNsd2 and control organoids (middle, n = 10 images each; unpaired two-tailed student's t-test). Quantification of organoid width in shNsd2 and control organoids. (right, n=10 images each; unpaired two-tailed student's t-test).

(g) Left, representative brightfield images of shSetd2 or control organoids. Scale bar 100 μm. Middle, quantification of organoid budding in shSetd2 and control organoids (middle, n=10 images each; unpaired two-tailed student's t-test). Quantification of organoid width in shSetd2 and control organoids. (right, n=10 images each; unpaired two-tailed student's t-test).

Figure S7.

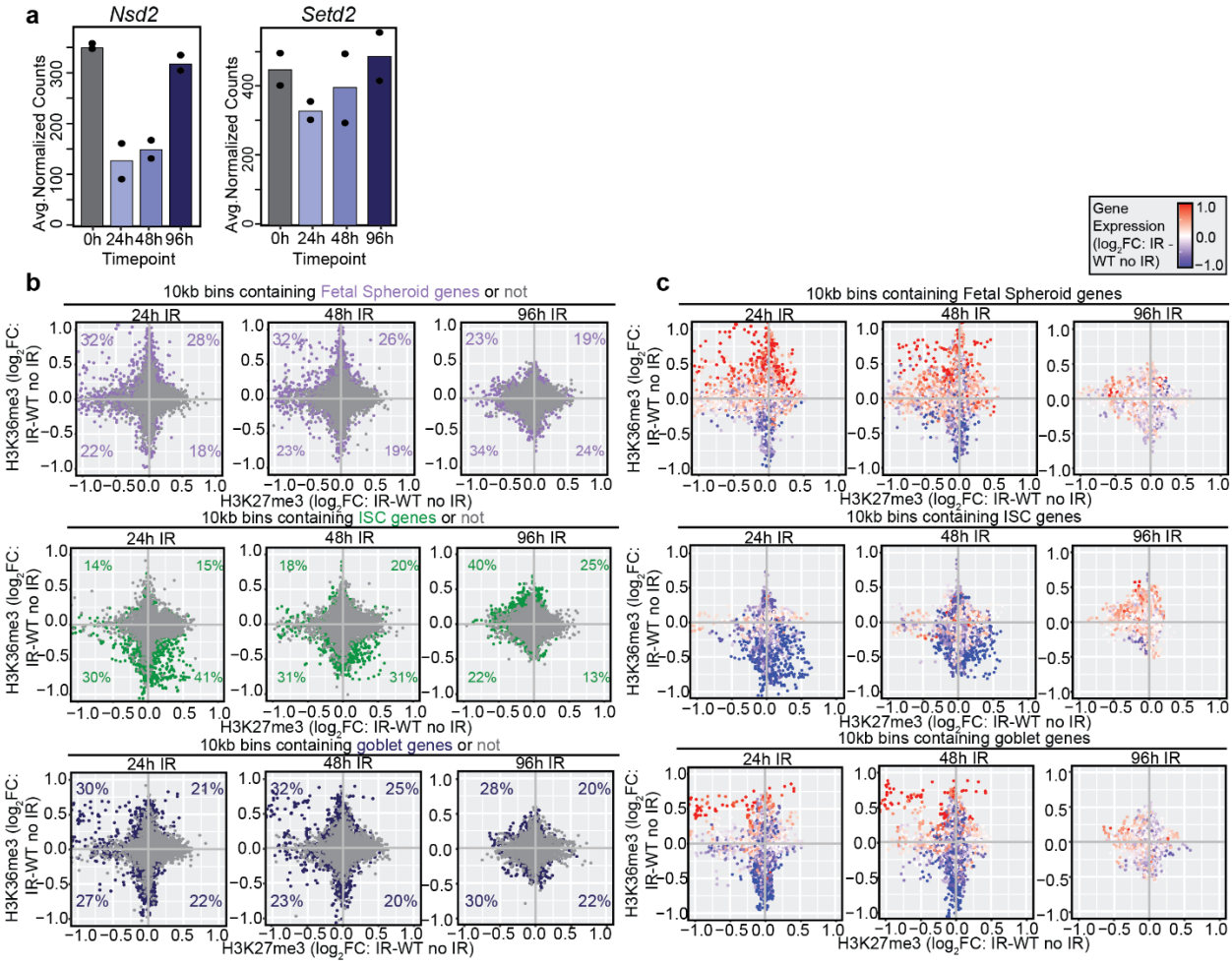

Supplemental Figure 7. H3K36 methylation is remodeled following injury-induced regeneration in organoids.

(a) Left, normalized gene counts of *Nsd2* from RNA-seq of irradiated organoids, each dot represents an independent replicate (n = 2 independent replicates). Right, normalized gene counts of *Setd2* from RNA-seq of irradiated organoids, each dot represents an independent replicate (n = 2 independent replicates).

(b) Differential methylation analysis between WT non-irradiated and 24-hour post-irradiation (left column), 48-hour post-irradiation (middle column), and 96-hour post-irradiation (right column) organoids in 10kb bins across the genome. In the top row, purple dots indicate bins containing published fetal spheroid-associated genes[109]. In the middle row, green dots represent ISC-associated genes. In the bottom row, blue dots represent goblet cell-associated genes. Up to 5000 datapoints are plotted at each timepoint.

Percentages in each quadrant represent the percentage of total colored dots in the graph that fall in that quadrant.

(c) Differential methylation analysis as in panel **b**, but with gene expression values overlaid (log_2FC gene expression in that bin).

Figure S8.

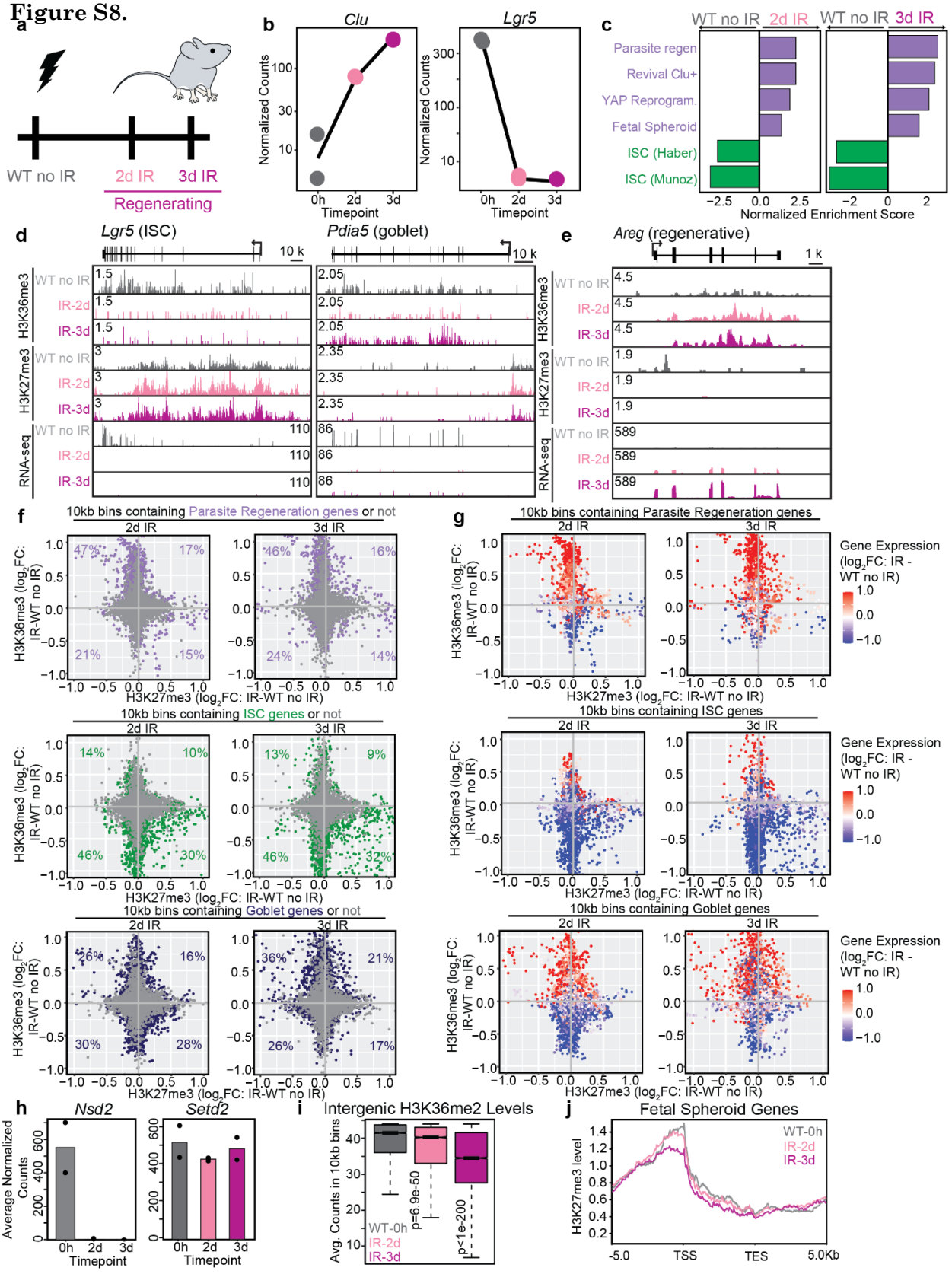
a
WT no IR
2d IR
3d IR
Regenerating
b
Clu
Lgr5
Normalized Counts
Timepoint
c
WT no IR 2d IR
WT no IR 3d IR
Parasite regen
Revival Clu+
YAP Reprogram.
Fetal Spheroid
ISC (Haber)
ISC (Munoz)
Normalized Enrichment Score
d
Lgr5 (ISC)
Pdia5 (goblet)
H3K36me3
H3K27me3
RNA-seq
WT no IR
IR-2d
IR-3d
e
Areg (regenerative)
f
10kb bins containing Parasite Regeneration genes or not
10kb bins containing ISC genes or not
10kb bins containing Goblet genes or not
H3K36me3 (log2FC: IR-WT no IR)
H3K27me3 (log2FC: IR-WT no IR)
g
10kb bins containing Parasite Regeneration genes
10kb bins containing ISC genes
10kb bins containing Goblet genes
Gene Expression (log2FC: IR - WT no IR)
h
Nsd2
Setd2
Average Normalized Counts
Timepoint
i
Intergenic H3K36me2 Levels
Avg. Counts in 10kb bins
p=6.9e-50
p<1e-200
j
Fetal Spheroid Genes
H3K27me3 level
TSS
TES
5.0Kb

Supplemental Figure 8. H3K36 methylation is remodeled following injury-induced regeneration in mice.

(a) A schematic of the experimental design for irradiation and harvest of intestinal epithelial cells from WT mice.

(b) Normalized gene expression counts based on RNA-seq at each timepoint in irradiated mice for *Clu*, a marker of regeneration, and *Lgr5*, a marker of ISCs (n = 2 biological replicates each).

(c) Gene set enrichment analysis based on RNA-seq data comparing WT non-irradiated and 2-day (left) and 3-day (right) post-irradiation mice using published gene sets[82,96,107–109,111].

(d) Representative gene tracks for H3K36me3, H3K27me3, and RNA-seq over *Lgr5*, a marker of ISCs, and *Pdia5,* a marker of goblet cells (n = 2 biological replicates each).

(e) Representative gene tracks for H3K36me3, H3K27me3, and RNA-seq over *Areg*, a marker of regeneration (n = 2 biological replicates each).

(f) Differential methylation analysis between WT non-irradiated and 2-day post-irradiation (left column) or 3-day post-irradiation (right column), mice in 10kb bins across the genome. In the top row, purple dots indicate bins containing published fetal spheroid-associated genes[109]. In the middle row, green dots represent ISC-associated genes. In the bottom row, blue dots represent goblet cell-associated genes. Up to 10,000 datapoints are plotted at each timepoint. Percentages in each quadrant represent the percentage of total colored dots in the graph that fall in that quadrant.

(g) Differential methylation analysis as in panel **f**, but with gene expression values overlaid (log_2FC gene expression in that bin).

(h) Normalized gene expression counts based on RNA-seq at each timepoint post-irradiation in mice for *Nsd2* and *Setd2* (n = 2 biological replicates each).

(i) Quantification of H3K36me2 binned into 10,000 randomly selected 10 kb intergenic regions in WT or 2-day and 3-day post-irradiation mice (Wilcoxon test; box plot center lines represent the median, box edges represent the first and third quartiles, and whiskers indicate minimum and maximum values).

(j) Meta-analysis of H3K27me3 in WT or 2-day and 3-day post-irradiation mice over a published regenerative gene set[109] (representative trace for 2 independent replicates).

Figure S9.

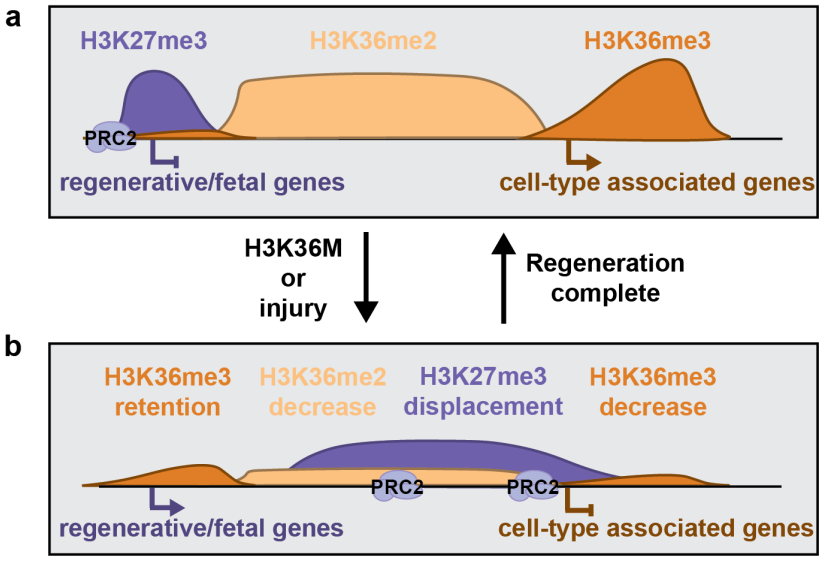

Supplemental Figure 9. H3K36 methylation regulates cell plasticity and regeneration in the small intestine.

(a) A schematic representation of chromatin under homeostatic conditions.

(b) Upon H3K36M induction or injury, H3K36me2 and H3K36me3 are depleted across the genome, but H3K36me3 is retained at regenerative genes. H3K27me3 spreads into intergenic regions and cell-type associated genes and is titrated away from regenerative genes. Changes to the chromatin landscape return to normal, homeostatic levels as regeneration completes.